Light-Matter Interaction in III-Nitride Waveguides: Propagating Polaritons and Optical Gain

THÈSE N^{O} 8946 (2018)

PRÉSENTÉE LE 29 OCTOBRE 2018
À LA FACULTÉ DES SCIENCES DE BASE
LABORATOIRE EN SEMICONDUCTEURS AVANCÉS POUR LA PHOTONIQUE ET L'ÉLECTRONIQUE
PROGRAMME DOCTORAL EN PHYSIQUE

ÉCOLE POLYTECHNIQUE FÉDÉRALE DE LAUSANNE

POUR L'OBTENTION DU GRADE DE DOCTEUR ÈS SCIENCES

PAR

Joachim Armand Simonne CIERS

acceptée sur proposition du jury:

Prof. P. Ricci, président du jury
Prof. N. Grandjean, Dr R. Butté, directeurs de thèse
Dr D. Krizhanovskii, rapporteur
Prof. P. Perlin, rapporteur
Prof. E. Matioli, rapporteur

ÉCOLE POLYTECHNIQUE
FÉDÉRALE DE LAUSANNE

Suisse
2018

We need numbers, not adjectives.
— Sir David J. C. MacKay

To those who strive to make this little spaceship a better place. . .

Acknowledgements

Even though this work carries only my name, it could not have been conceived without the contributions of many other people. Before talking about the results of this study, they deserve to be acknowledged.

First and foremost, I should thank my thesis directors, Nicolas and Raphaël, for giving me the chance to work in their lab, for their guidance, availability, valuable feedback and exemplary work attitude. I consider myself privileged when realizing that most PhD students don't have this kind of supervision.

Second, I also wish to acknowledge Prof. Paolo Ricci, for accepting to preside my thesis jury, and the experts, Prof. Elison Matioli, Dr. Dmitry Krizhanovskii and Prof. Piotr Perlin for the time and effort they have spent on my work, and the fruitful discussion we had.

Third, I want to thank Jean-François, for the growth of the samples, many good ideas and interesting discussions. I definitely also need to acknowledge Marlene, who took me under her wings during the first months of my PhD and learned me how to do spectroscopy, processing, data analysis, and many other little things.

I am grateful to the other past and present members of LASPE, for the good and collaborative atmosphere and countless great scientific and non-scientific exchanges: Gwénolé for TRPL and CL measurements and valuable expertise; Gordon for PLE measurements and many interesting discussions on spectroscopy; Ian for a test sample and many elucidating office conversations; Noelia for her help with Lumerical and fabrication; Camille for help with Nextnano and her wonderful PLubby software; Gedis for his help with moving the PL lab and with PL measurements; Marco for helping me with the VSL setup; Christian for help with the PR setup; Kanako for help with the lift-off; Hezhi for the processing; Nino for advice on processing; Wei for TRPL measurements; Pirouz for Nextnano advice; Nadja for help with the administration; Sebastian, Denis, Lorenzo, Mauro, Etienne, Jean-Michel and Lise. I should also mention the master students that contributed to the lab atmosphere over the years: Irene, Yao, Ching-wen, Alex, Coralie and Louis, with a special thanks to the students I supervised, Marina and Jonas, for many hours spent in the lab. Thanks also to the cleanroom staff: Nicolas, Damien, Yoan and François for their help with many little things, in the lab and in the cleanrooms. Thanks to the CMi staff and especially Zdenek and Joffrey for their great support and their meticulous maintenance of the e-beam tool.

I am also grateful to the external collaborators: Antoine Congar, for several long but nice FIB sessions; Paul Walker and Dmitry Krizhanovskii, for an interesting stay in Sheffield; and Catherine Bougerol, for great TEM images.

Ook wil ik mijn familie en Roselien bedanken, voor de steun doorheen alles.

Last, but definitely not least, I want to thank Anastasiia, for her help with figures, her support and understanding in difficult times, and her warmth.

This thesis work was financially supported by the Swiss National Science Foundation.

Lausanne, August 28, 2018 Joachim Ciers

Abstract

III-nitride waveguides featuring AlInN claddings and GaN/AlGaN quantum wells (QWs) offer promising perspectives for applications in many fields of short-wavelength photonics. Thanks to their nearly lattice-matched nature, these structures exhibit an excellent material quality, leading, e.g., to strong light-matter interaction in such QWs, and several promising phenomena.

In the low carrier density regime, the strong coupling between QW excitons and waveguide photons results in propagating hybrid light-matter particles, called (exciton-)polaritons, which combine photon-like propagation and exciton-like interactions. These interactions lead to a strong optical nonlinearity, which could be useful for integrated all-optical devices. Due to their strong exciton binding energy ($\sim$40 meV in the present structures), III-nitride devices have the potential to maintain these nonlinearities up to room temperature.

In the high carrier density regime, a GaN/AlGaN QW electron-hole plasma can provide gain to an optical field in the UV, which can be useful for realizing near-UV laser diodes and semiconductor optical amplifiers. The performance of current UV devices featuring AlGaN claddings is limited by poor material quality. The improved structural quality of waveguides with lattice-matched AlInN claddings could therefore circumvent these issues.

This study aims at an in-depth investigation of the optical properties of III-nitride waveguides with AlInN claddings and GaN/AlGaN QWs grown on freestanding GaN substrates. In a sample with an active region that was optimized for strong exciton-photon coupling, we observe propagating polaritons in the low-density regime. A sample with an active region that was optimized for homogeneous near-resonant excitation with a 355 nm laser shows elevated optical gain in the high-density regime. The nearly lattice-matched nature of the entire structure leads to a high structural and optical quality. We found inhomogeneous broadening values between 8 and 11 meV, and a standard deviation in the QW emission energy well below 1 meV over a $50 \times 50\ \mu\mathrm{m}^2$ area. We calculated the band structure and transition energies of the QWs using self-consistent Schrödinger-Poisson $k \cdot p$ calculations and found an excellent agreement with experiments.

The waveguide polaritons feature a normal mode splitting as large as 60 meV at low temperature, thanks to the large overlap between the optical mode and the active region, a polariton decay length up to 100 μm for photon-like polaritons and a lifetime of 1-2 ps. These decay lengths and lifetimes are limited by residual absorption occurring in the waveguide. The large normal mode splitting and elevated in-plane homogeneity are important assets for the realization of polaritonic integrated circuits.

We also demonstrate optically-pumped waveguides exhibiting narrow bandwidth (3.8 nm) optical gain around 370 nm. Due to the high refractive index contrast between the cladding layers and the active region, the confinement factor is as high as 48% and net modal gain values in excess of 80 cm^{-1} are measured. The results agree well with self-consistent calculations accounting for built-in electric field effects and high carrier density related phenomena. As such, these results open interesting perspectives for the realization of more efficient near-UV laser diodes and semiconductor optical amplifiers.

Keywords: III-nitrides, gallium nitride, aluminum indium nitride, lattice-matched growth, multiple quantum wells, excitons, electron-hole plasma, waveguides, light-matter coupling, exciton-polaritons, waveguide polaritons, strong coupling regime, optical gain

Résumé

Les guides d'onde à base de nitrures d'éléments III comportant des gaines optiques AlInN et des puits quantiques GaN/AlGaN sont prometteurs pour de nombreuses applications dans le domaine de la photonique à courtes longueurs d'onde (proche UV). Comme ces structures sont en quasi-accord de maille, elles présentent d'excellentes qualités structurales conduisant, entre autre, au régime de couplage fort lumière-matière qui permet d'explorer de nombreux phénomènes physiques inaccessibles par ailleurs.

Dans le régime de faible densité de porteurs injectés, le couplage fort entre les excitons de puits quantiques et les photons de guides d'onde conduit à la formation de polaritons excitoniques guidés, qui sont des particules hybrides lumière-matière. Ces quasi-particules combinent d'excellentes propriétés de propagation en raison de leur part photon tout en pouvant interagir entre elles via leur part excitonique. Ces interactions entraînent une forte non-linéarité optique qui permettrait la réalisation de nouveaux dispositifs optiques intégrés. En raison de la forte énergie de liaison excitonique (40 meV dans les structures étudiées dans ce travail), ces dispositifs ont le potentiel pour maintenir ces non-linéarités jusqu'à température ambiante voire au-delà.

Dans le régime de densité de porteurs injectés élevée, un plasma électron-trou va se former dans les puits quantiques GaN/AlGaN qui peut générer un gain optique élevé dans le proche UV. L'obtention d'un tel gain est essentiel pour la réalisation de diodes lasers et d'amplificateurs optiques à semiconducteurs opérant dans le gamme spectrale 330-380 nm. Les performances des dispositifs UV actuels comportant des gaines optiques à base d'AlGaN est limitée par leur qualité structurale, ce dont ne souffrent pas les guides d'onde basés sur des gaines optiques AlInN de par la quasi absence de contraintes/déformations de la maille atomique.

Le but de ce travail est de fournir une analyse détaillée des propriétés optiques des guides d'onde à base de nitrures d'éléments III avec des gaines optiques AlInN et des puits quantiques GaN/AlGaN crûs sur des substrats de GaN. Dans un échantillon avec région active optimisée pour le couplage fort exciton-photon, nous avons observé des polaritons guidés dans le régime de faible densité de porteurs. Un échantillon avec région active optimisée pour une excitation quasi-résonante homogène avec un laser à 355 nm présente un gain optique élevé dans le régime de forte densité de porteurs. Les structures étudiées étant en quasi-accord de maille, leur excellente qualité structurale se traduit par des valeurs de l'élargissement inhomogène des puits quantiques comprises entre 8 et 11 meV, et un variation de l'énergie d'émission des puits bien inférieure à 1 meV sur une zone de $50 \times 50\ \mu m^2$. La qualité de ces structures est par ailleurs validée par l'excellente adéquation entre les résultats issus de calculs de la structure de bandes et des énergies de transition des puits quantiques reposant sur la méthode dite de Schrödinger-Poisson $k \cdot p$ cohérente et les mesures expérimentales.

Les polaritons guidés observés présentent une séparation de Rabi de 60 meV à basse température. Cette valeur particulièrement élevée résulte du fort recouvrement entre le mode optique guidé et la région active. Nous observons une longueur d'atténuation des polaritons guidés de l'ordre de 100 μm pour des polaritons au caractère photonique élevé et une durée de vie de 1 à 2 ps. Ces longueurs d'atténuation et ces durées de vie sont pour le moment limitées par l'absorption résiduelle dans le guide d'onde. La grande séparation de Rabi et l'uniformité élevée dans le plan des couches sont des avantages essentiels pour la réalisation de circuits intégrés polaritoniques.

Nous démontrons également la réalisation de guides d'ondes pompés optiquement présentant un gain optique sur une plage spectrale étroite (3,8 nm) autour de 370 nm. En raison du contraste élevé de l'indice de réfraction optique entre la gaine optique et la région active, le facteur de confinement atteint 48% et des valeurs du gain modal net supérieures à 80 cm^{-1} sont mesurées. Les résultats concordent avec les calculs cohérents qui prennent en compte les effets d'écrantage du champ électrique interne des puits quantiques et les phénomènes de renormalisation liés à la densité de porteurs élevée. Ces résultats ouvrent des perspectives très prometteuses pour la réalisation de diodes lasers et des amplificateurs optiques à semiconducteurs opérant dans le proche UV plus efficaces que les dispositifs actuels.

Mots-clés : nitrures d'éléments III, nitrure de gallium, nitrure d'indium et d'aluminium, croissance en accord de maille, puits quantiques multiples, excitons, plasma électron-trou, guides d'onde, couplage lumière-matière, exciton-polaritons, régime de couplage fort, gain optique

Contents

List of Figures

List of Tables

List of Acronyms

0…3D	0…3 dimensional
2DEG	Two-dimensional electron gas
AFM	Atomic force microscopy
ASE	Amplified spontaneous emission
BGR	Bandgap renormalization
CAD	Computer-aided design
CB	Conduction band
CL	Cathodoluminescence
CCD	Charge-coupled device
COM	Coupled oscillator model
(PE)CVD	(Plasma-enhanced) Chemical vapor deposition
CW	Continuous wave
DAP	Donor-acceptor pair
DBR	Distributed Bragg reflector
DOS	Density of (electronic) states
e-beam	Electron beam
e-h	Electron-hole
(Δ)EN	(Difference in) Electronegativity
FWHM	Full width at half maximum
FDTD	Finite-difference time-domain
HEMT	High electron mobility transistor
hh	Heavy hole (subband)
IQE	Internal quantum efficiency
III-N	Group-III-nitride
IR	Infrared
ICP	Inductively coupled plasma
JDOS	Joint density of states
LD	Laser diode
LDOS	Local density of optical states
LED	Light-emitting diode
LO	Longitudinal optical (phonon)
lh	Light hole (subband)
LP(B)	Lower polariton (branch)
MOCVD	Metalorganic chemical vapor deposition
MOVPE	Metalorganic vapor phase epitaxy
Nd:YAG	Neodymium-doped yttrium aluminum garnet
NA	Numerical aperture
PID	Proportional–integral–derivative
PML	Perfectly matched layer
(μ-)PL	(Micro-)Photoluminescence
PLE	Photoluminescence excitation
PR	Photoreflectance
PMMA	Poly(methyl methacrylate)
QCSE	Quantum-confined Stark effect
(M)QW	(Multiple) Quantum well
RF	Radio-frequency
RIC	Refractive index contrast
RIE	Reactive ion etching
SCR	Strong coupling regime
S(T)EM	Scanning (tunneling) electron microscopy
so	Split-off (subband)
SOA	Semiconductor optical amplifier
SS	Stokes shift
(HR)TEM	(High-resolution) Transmission electron microscopy
TIR	Total internal reflection
TE	Transverse electric polarization
TM	Transverse magnetic polarization
TEGa	Triethylgallium
TMAl	Trimethylaluminium
TMGa	Trimethylgallium
TMIn	Trimethylindium
TMS	Transfer matrix simulations
TRPL	Time-resolved photoluminescence

UP(B)	Upper polariton (branch)
UV	Ultraviolet
VB	Valence band
VSL	Variable stripe length
WCR	Weak coupling regime
(HR-)XRD	(High-resolution) X-ray diffraction
XX	Biexciton

List of Symbols

α_V	Varshni α parameter
α_B	Electron-phonon coupling constant
α	Absorption coefficient
α_{2D}	Two-dimensional absorption coefficient
α_{wg}	Absorption coefficient in the waveguide
β	In-plane wavevector component
β_V	Varshni β parameter
γ_{hom}	FWHM homogeneous broadening
γ_{inh}	FWHM inhomogeneous broadening
γ_{ph}	Photonic broadening/decay rate
γ_{PR}	PR linewidth
γ_X	Excitonic broadening/decay rate
Γ/Γ_i	Confinement factor (of QW i)
δ	Exciton-photon detuning
Δ_{BGR}	Bandgap renormalization shift
Δ_{cf}	Crystal-field splitting
Δ_{so}	Spin-orbit splitting
ε	Permittivity
ε_0	Vacuum permittivity
ε_{rel}	Relative permittivity $\frac{\varepsilon}{\varepsilon_0}$
λ	Wavelength
λ_e	de Broglie wavelength of an electron
μ_0	Vacuum permeability
Ψ_e	Electron envelope function
Ψ_h	Hole envelope function
Φ	Electrostatic potential
ρ	Charge density
σ	Charge plane density
$\bar{\bar{\sigma}}$	Stress tensor
Θ_B	Average phonon temperature
θ_{PR}	Phase factor representing the asymmetry of the PR lineshape
τ_{nr}	Nonradiative lifetime
τ_r	Radiative lifetime
τ_{ph}	Photon lifetime
τ_X	Exciton lifetime
τ_{pol}	Polariton lifetime
ω	Photon angular frequency
a_B	Exciton Bohr radius
b	Bandgap bowing parameter
$\mathbf{B}$	Magnetic induction
c	Vacuum speed of light
C_{PR}	Photoreflectance normalization factor
d_{ijk}	Piezoelectric moduli
d_{QW}	Quantum well thickness
d_{wg}	Waveguide thickness
D_{cv}	Joint density of states (between VB and CB)
$\mathbf{D}$	Electric displacement
$\mathbf{E}$	Electric field
e	Elementary charge
$\mathbf{e}_E$	Light polarization vector
E_0	Single-photon electric field amplitude
E_B	Exciton binding energy
E_B^{XX}	Biexciton binding energy
E_g	Bandgap energy
E_k	Kinetic energy
E_P	Kane energy

E_{ph}	Photon energy
E_{QW}	Quantum well interband transition energy
E_{tr}	Transition energy
$E^{j}_{tr,0}$	Transition energy at low carrier density, with j representing the A or B transition
E_X	Exciton energy
F	Polarization field
f_c	Fermi-Dirac distribution of electrons
f_v	Fermi-Dirac distribution of holes
f_{cv}	Interband oscillator strength
f_X	Exciton oscillator strength (2D or 3D)
g	Optical gain
g_{mod}	Net modal gain
g_{mat}	Material gain
g_0	Exciton-photon coupling strength
h	Planck constant
$\hbar$	Reduced Planck constant
$\mathbf{H}$	Magnetic field
H_{int}	Light-matter interaction Hamiltonian
I	Optical intensity (various subscripts)
I_{sat}	Saturation optical intensity
$\mathbf{J}$	Electric current density
k_B	Boltzmann constant
$\mathbf{k}$	Wavevector
k_j	Magnitude of the wavevector in medium j
$k_{\perp c}$	Basal plane wavevector component
$k_{//c}$	Wavevector component along the c-axis
L_{eff}	Modal effective length
l_{min}	Rayleigh resolution limit
M^*	Exciton mass
m_0	Free electron mass
m_e^*	Effective electron mass
m_h^*	Effective hole mass
m_r	Reduced electron-hole mass
m_{PR}	PR lineshape parameter representing the dimensionality of the critical point
n	Exciton principal quantum number
n_{op}	Refractive index
n_i	Imaginary part of the refractive index
n_r	Real part of the refractive index
n_e	Extraordinary refractive index
n_o	Ordinary refractive index
N	Carrier density
N_X	Exciton density
N_{XX}	Biexciton density
N_{QW}^{eff}	Effective number of QWs
$\mathbf{P}_{pz}$	Piezoelectric polarization
$\mathbf{P}_{sp}$	Spontaneous polarization
$\mathbf{P}_{tot}$	Total polarization
P	Photonic Hopfield coefficient
p	Momentum
$\mathbf{r}$	Position vector
R_{cv}	Interband transition rate
R	Reflectance
r_{cv}	Interband optical matrix element
T	Temperature
V	Modal volume
V_{bg}	Background potential
X	Excitonic Hopfield coefficient

Introduction

III-nitride (III-N) semiconductors, and especially gallium nitride (GaN), have allowed several technological breakthroughs over the past two decades, thanks to interesting properties such as their large bandgap as well as their thermal and chemical robustness. This culminated in the 2014 Nobel Prize in Physics *for the invention of efficient blue light-emitting diodes which has enabled bright and energy-saving white light sources*, that was awarded to Isamu Akasaki, Hiroshi Amano and Shuji Nakamura [1]. A first important step was the realization of p-type doping in GaN epilayers reported by Amano *et al.* [2] through activation of Mg acceptors by low-energy electron beam irradiation and the alternative activation method developed by Nakamura *et al.*, based on thermal annealing [3]. This led to the development of high-brightness blue light-emitting diodes (LEDs) [4] and laser diodes (LDs) [5]. These blue LEDs form the basis of the efficient white LED that is ubiquitous in present-day lighting. Blue III-N LDs are for example used for high-density optical data storage, such as Blu-ray disc readers, which can store 2.28 GB/cm^2 per layer [6] using a laser spot with a diameter of 580 nm [7]. Additionally, III-nitrides are used in high electron mobility transistors (HEMTs) for high-temperature, high-power, and high-frequency electronics. These applications render III-nitrides currently the second semiconductor material family after silicon in terms of total market share, and the dominating material system in optoelectronics.

The III-N material family is particularly interesting for optical applications due to its strong light-matter interaction, which is a direct consequence of their direct wide bandgap. This leads to interesting phenomena, such as the strong light-matter coupling regime, where photons hybridize with excitons,[1] and optical gain, which is the core process in the operation of lasers and optical amplifiers. In this thesis work, we investigate these phenomena in planar waveguides, operating in the near UV spectral region, where the optical mode is confined via total internal reflection.

Optical waveguides operating in the strong light-matter coupling regime are a promising platform for applications in photonic integrated circuits. Such integrated circuits have a large potential in the field of information technology. The footprint of an optical device can be scaled down to the optical wavelength, while its clock rate could be scaled up to the order of optical frequency [8]. The latter ranges from 200 THz at 1550 nm to 750 THz at 400 nm. Optical devices require very little energy, as photons can travel nearly lossless, with loss rates on the order of 0.3 dB/cm in silicon photonic devices around 1550 nm [9].

---

[1] An exciton is an electronic excitation consisting of a conduction band electron and a valence band hole, which are bound by Coulomb interaction.

One of the inherent difficulties with all-optical devices is the lack of interaction between photons,[2] which makes it nearly impossible to directly modify a light beam with a second one. A nonlinear medium is therefore required to couple two optical signals.

In case of a nonlinear all-optical device made from traditional dielectric materials, typical values for the nonlinear refractive index are on the order of 10^{-16} cm^2/W [11]. This implies that large intensities on the order of 10^{15} W/cm^2 are required to operate such a device. Present plasmonic alternatives, where interaction is possible through the electronic part, are inherently lossy [12].

An interesting pathway to realize such a nonlinearity makes use of exciton-polaritons, hereafter called polaritons, in the waveguide geometry. Polaritons are quasiparticles that arise from the hybridization between a (confined) photon mode and a semiconductor exciton in the strong coupling regime (SCR) [13]. As a consequence of this hybridization, their properties are intermediate between those of photons and excitons. As such, they benefit from the best of both worlds. Polaritons can propagate at near light speed and interact through their exciton fraction. This makes them ideal candidates for low-power active all-optical devices such as switches, optical transistors and logic gates [14, 15]. A polariton-based device, combines a strong nonlinearity–on the order of 10^{-10} cm^2/W– with a very fast response time on the order of a few picoseconds [15, 16]. The realization of waveguide polaritons in III-N structures, which have previously shown polariton nonlinearities in microcavities up to room temperature due to their elevated exciton binding energy [17, 18], would be an important step towards practical devices.

Besides the success story of III-nitride emitters in the blue-green part of the spectrum, they also find applications in the UV. Efficient UV light sources are a key enabling technology for applications in many areas such as photolithography, polymer curing, high-density data storage, gas sensing, water disinfection (in the 230-300 nm spectral region), dermatological phototherapy, and UV fluorescence [19]. Recent advances in III-nitride LEDs and LDs have resulted in large improvements in these fields, with more compact, robust, and power-efficient devices compared to conventional technologies, often based on large and toxic mercury lamps or gas lasers. However, as a general trend, III-N-based UV light sources exhibit decreasing device performance with decreasing emission wavelength [20, 21], as illustrated in Fig. 1. This is a result of (i) valence band ordering effects that prevent surface emission in Al-rich *c*-plane oriented devices [22], (ii) reduced *p*-type conductivity, due to increasing activation energy of the Mg-acceptor with increasing bandgap, and (iii) reduced material quality for AlGaN alloys with increasing AlN mole fraction. For UV-C devices, which are emitting below 280 nm, great progress has been made regarding (iii), thanks to the progressive availability of bulk AlN substrates [23].

Although III-N LEDs have been demonstrated with emission wavelengths down to 210 nm [24], the shortest emission wavelength demonstrated to date for LDs is 336 nm [25]. Shorter wavelength operation requires either optical [23] or electron beam pumping [26]. Because of

---

[2] The linearity of Maxwell's equation results in the superposition principle of electromagnetic fields. Therefore, photon-photon scattering is classically forbidden. It is a weak quantum electrodynamical effect that has been observed for huge electric fields on the order of 10^{25} Vm^{-1}, which corresponds to an intensity on the order of 10^{43} W/cm^2 [10].

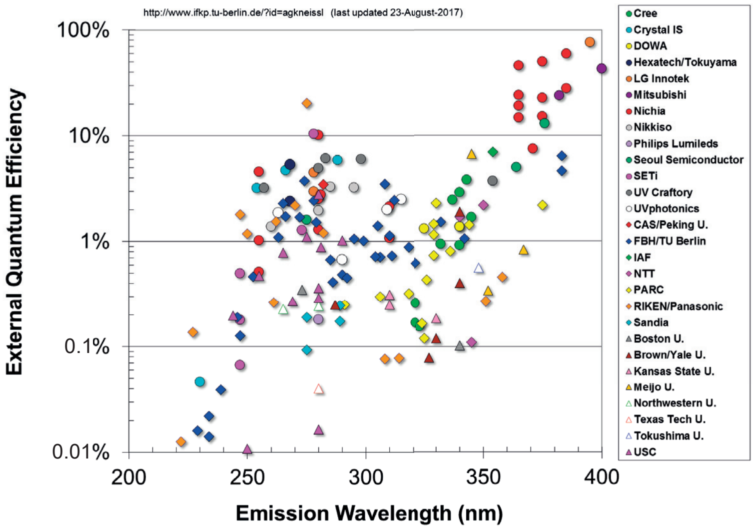

Figure 1 – External quantum efficiency of UV LEDs at room temperature from different research groups and commercial companies as a function of emission wavelength. The efficiency decreases by several orders of magnitude with decreasing wavelength. A peak in the external quantum efficiency can be observed around 280 nm, which results from improved AlGaN material quality through growth on AlN substrates. Reproduced from [20, 21].

the above-mentioned issues, the lasing threshold increases drastically for short-wavelength III-N LDs [27], hence limiting their present use to pulsed mode.

The objectives of this thesis work are to investigate the optical properties of III-nitride waveguides featuring GaN/AlGaN quantum wells (QWs) emitting in the UVA spectral region –i.e. between 320 and 400 nm– and AlInN cladding layers. More specifically, the goal is to investigate the potential of these structures for strong light-matter coupling and to generate optical gain. The AlInN claddings offer a high refractive index contrast with the AlGaN alloy over a wide range of Al contents [28, 29], which provides good optical confinement, while being grown nearly lattice-matched to GaN, resulting in very good overall material quality [30, 31, 32]. This excellent optical confinement leads to an enhanced light-matter interaction, both below and above the Mott transition.[3] At carrier densities below the Mott transition, the coupling between excitons and photons can lead to the strong coupling regime described before. Above the Mott transition, an electron-hole plasma can provide gain to an optical field. The enhanced light-matter interaction provides a potential pathway to decrease the transparency and lasing threshold in gain-based devices. Furthermore, *p*-type doping of AlInN has been demonstrated [33] and high-quality AlInN layers have been successfully used for optical mode confinement in visible III-N edge-emitting LDs [34, 35] and vertical-cavity surface-emitting lasers [36]. Additionally, blue laser diodes with both an *n*-type AlInN bottom cladding and *p*-type AlInN top cladding were developed [35]. The use of AlInN claddings could therefore lead to substantial improvements in LD device performance in the UVA spectral region.

---

[3] The Mott transition is the transition from an insulating exciton gas to a conducting electron-hole plasma that arises at high carrier densities or at elevated temperatures.

The remainder of this manuscript will be structured as follows: The relevant properties of III-N semiconductors are discussed in Chapter 1, while Chapter 2 explains the physics of light-matter coupling in waveguides. An in-depth investigation of the optical properties of the QWs in the present structures is reported in Chapter 3. Chapter 4 illustrates the properties of propagating polaritons that are supported by these waveguides. Chapter 5 describes on the optical gain that can be achieved in the present structures. Finally, a summary of the results and an outlook is given in Chapter 6.

1 III-Nitride Semiconductors

This chapter will give an overview of some selected topics in III-nitride semiconductors that are relevant to this PhD thesis work. We will focus on the conventional binary compounds InN, GaN and AlN and their ternary alloys (i.e. InGaN, AlGaN and AlInN). Other nitride semiconductors, such as BN or ScN that have recently attracted scientific attention, are outside the scope of this manuscript. In particular, the discussion will center around the properties of GaN, $Al_xGa_{1-x}N$ with low Al content ($x \approx 0.1$) and $Al_{1-x}In_xN$ with $x \approx 0.18$, which is lattice-matched to GaN. The structural properties of these materials are discussed in Section 1.1, while Section 1.2 illustrates their optical properties.

1.1 Structural Properties

1.1.1 Crystal Structure

The thermodynamically stable phase of III-nitride compounds (under standard conditions) has the hexagonal wurtzite structure. This is contrary to other III-V material systems, such as III-As or III-P, which crystallize with the cubic zinc-blende structure. Rock-salt [37, 38] and zinc-blende [39] III-N structures can be created under certain conditions, but all commercial III-N devices, as well as the samples used in this work have the wurtzite crystal structure. We will therefore focus exclusively on the properties of the wurtzite phase in the remainder of this manuscript.

In wurtzite crystal structures, it is common to describe crystal orientations by four coordinates $[hkil]$ that incorporate the hexagonal permutation symmetries, rather than the three Miller indices used in cubic lattices. The first three coordinates define respective axes that are oriented at an angle of 120° with respect to each other within the hexagonal basal plane of the unit cell. They are related by $h+k+i=0$, since there are only two degrees of freedom in the plane. The fourth coordinate, l, describes the axis perpendicular to the basal plane, which is called the c-axis.

The III-N wurtzite structure is shown in Fig. 1.1. It consists of a hexagonal close-packed lattice with a two-atom basis (one group-III atom and one N atom), which are separated by a distance

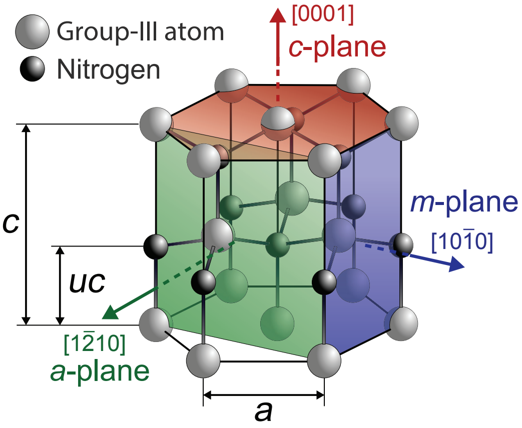

Figure 1.1 – Wurtzite crystal structure of group-III nitrides. The nitrogen (black) and group-III (grey) atoms each occupy a hexagonal close-packed sub-lattice with a relative displacement of uc along the [0001] direction. The principal planes and directions (a, c, m) are indicated.

uc along the c-axis. Here, c denotes the distance between two equivalent basal planes and $u = 3/8 = 0.375$ in an ideal wurtzite lattice. Nearest-neighbor atoms in the basal plane are separated by a. The a, c and u parameters for the binary compounds InN, GaN and AlN are given in Tab. 1.1. These structural parameters have been observed to precisely follow Vegard's law for the ternary alloys AlGaN and InGaN [40]. This means that their values can be obtained by linear interpolation between the two composing binary compounds. In the case of AlInN, a deviation from Vegard's law is reported [41, 42].

Alternatively, the hexagonal close-packed structure can be seen as an ABABAB... stack of alternating monolayers A and B, each containing a sub-layer of group-III atoms and a sub-layer of nitrogen atoms, where B is displaced by $[\frac{1}{2}\overline{\frac{1}{2}}0\frac{1}{2}]$ with respect to A. Since a unit cell contains one layer of A and one of B, the monolayer thickness for growth along the c-axis is equal to $c/2$.

The most common crystal orientation for the growth of III-N structures in industry and academia is the c-plane, thanks to the associated high crystalline quality, mature growth, processability, in-plane isotropic properties and the availability of c-plane freestanding GaN substrates with a relatively low threading dislocation density (on the order of 10^6 cm^{-2}). Of the two possible crystal orientations, $+c$ and $-c$ –also called Ga-polar and N-polar after the atoms in the terminating sub-layer, respectively–, the $+c$ direction is used in the majority of cases, since the N-polar surface suffers from an increased incorporation of oxygen impurities [43], which results in a reduced optical quality [44]. For these reasons, the samples used in this thesis work, just like all commercial III-N devices, are grown along the $+c$ direction.

Due to the differences in lattice parameters of the III-N compounds mentioned in Tab. 1.1, III-N heterostructures can, in some cases, suffer from a severe lattice-mismatch. For c-plane growth, the lattice-mismatch of the relevant a parameter, is defined as $\frac{a_{layer}-a_{substrate}}{a_{substrate}}$ and it amounts to -2.4% for AlN on GaN and +10.9% for InN on GaN. This leads to tensile (positive) or compressive (negative) strain in the epilayers, defined as $\frac{a_{substrate}-a_{layer}}{a_{layer}}$, respectively. Beyond a certain critical layer thickness, threading and misfit dislocations will be formed [45, 46]. In the case of large tensile strain, even cracks will be generated in the sample. Strain management and engineering

	InN	GaN	AlN
c (Å)	5.704	5.186	4.981
a (Å)	3.538	3.189	3.112
u	0.377	0.379	0.387
ΔEN	1.26	1.23	1.43

Table 1.1 – Lattice parameters of binary wurtzite III-N semiconductors at room temperature. The structural data (c, a and u) were obtained by X-ray diffraction in refs. [48, 49]. The difference in electronegativity (ΔEN) between group-III and N atoms defines the ionicity of the bond [50].

can be required to avoid degraded material quality [47]. In this respect, $Al_{0.82}In_{0.18}N$ is a very interesting alloy, since it is lattice-matched to GaN and has a higher bandgap (see Section 1.2.1) and lower refractive index (Section 1.2.6) compared to the latter [28, 29, 30]. The growth of AlInN layers is discussed in Section 1.1.3.

1.1.2 Polarization Fields

The wurtzite crystal structure, contrary to its zinc-blende counterpart, lacks inversion symmetry. Together with the ionic character of the covalent bonds due to the substantial difference in electronegativity between nitrogen and group-III elements (ΔEN, given in Tab. 1.1), this results in a separation of the barycenters of positive (group-III) and negative (N) charges along the c-axis within the unit cell. As a consequence, these materials have an intrinsic polarization vector, a property which is known as pyroelectricity. The polarization in case of an unstrained material is called spontaneous polarization $\mathbf{P}_{sp}$, while the additional polarization coming from lattice deformations in a strained layer is called piezoelectric polarization $\mathbf{P}_{pz}$. It is related to the stress tensor $\overline{\overline{\sigma}}$ via the piezoelectric moduli d_{ijk} [51]

$$P_{pz,i} = \sum_{jk} d_{ijk}\sigma_{jk}. \tag{1.1}$$

The spontaneous polarization values for relaxed binary and ternary III-N compounds are shown in Fig. 1.2, as determined by Ambacher *et al.* [40]. The total polarization $\mathbf{P}_{tot} = \mathbf{P}_{sp} + \mathbf{P}_{pz}$ for the case of layers pseudomorphically grown on relaxed GaN, which is the relevant case for this thesis work, is also shown in Fig. 1.2. Note the special case of $Al_{0.82}In_{0.18}N$, which is lattice-matched to GaN and therefore has $\mathbf{P}_{pz} = \mathbf{0}$ [30, 52].

As a result of the polarization mismatch between the different materials, c-plane III-N heterointerfaces will contain a charge plane σ (expressed in elementary charges e per unit of surface) given by

$$\sigma = \frac{\Delta\mathbf{P}\cdot\mathbf{n}}{e}, \tag{1.2}$$

where $\Delta\mathbf{P} = \mathbf{P}_2 - \mathbf{P}_1$ and $\mathbf{n}$ represents a unity vector normal to the interface and pointing from

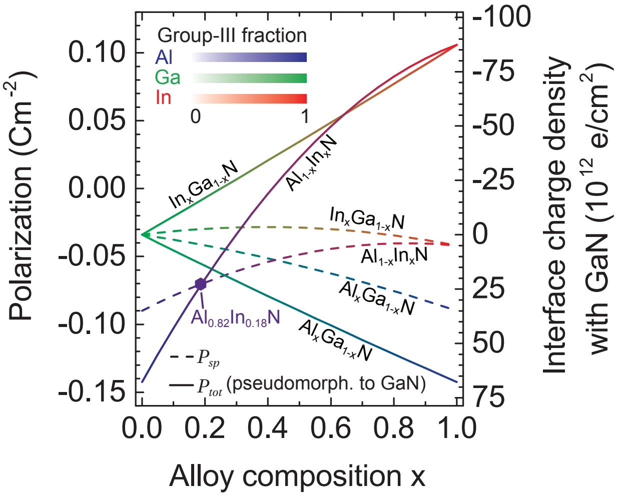

Figure 1.2 – Polarization in ternary III-N alloys as a function of alloy composition (x-axis and colorscale). The c-component of the spontaneous polarization $\mathbf{P}_{sp}$ of the unstrained alloy is given (dashed line) as well as the c-component of the total polarization $\mathbf{P}_{tot} = \mathbf{P}_{sp} + \mathbf{P}_{pz}$ for a layer grown pseudomorphically on a relaxed c-plane freestanding GaN substrate (solid line). The right axis shows the corresponding charge density at the interface with GaN. Data from [40].

material 2 to 1. The corresponding interface charge density at the interface with the GaN substrate for the pseudomorphic layers is equally shown on the right-hand side vertical axis of Fig. 1.2.

These positive and negative charge planes result in built-in electric fields in III-N heterostructures grown along the c-axis, which is therefore called the polar axis. The a- and m-axes are called non-polar axes and growth axes which are intermediate between the basal plane and the c-axis are called semi-polar axes. These electric fields are exploited to form a 2D electron gas in III-N HEMTs and have an important impact on the optical properties of III-N nanostructures such as QWs and quantum dots grown along a polar or semi-polar axis, through the quantum-confined Stark effect (QCSE, explained in Section 1.2.3).

1.1.3 Crystal Growth

Growth of III-N semiconductor compounds is in many aspects different from conventional III-V materials. First, there is a lack of inexpensive and lattice-matched substrates with hexagonal structure. Historically, the development of III-nitrides has been done on sapphire (0001) substrates, which are low-cost, but are severely lattice-mismatched to GaN (+16%, meaning that the GaN in-plane lattice parameter a is 16% larger than that of sapphire), leading to a high threading dislocation density of $10^8 - 10^9$ cm^{-2} [47]. Sapphire is still the substrate of choice for LED production due to its low price, availability in large diameters (up to 8 inches) and transparency across the visible spectrum. The situation of Si (111) is slightly worse with a low cost but no transparency in the visible and a -17% lattice mismatch. Additionally, the large mismatch in thermal expansion coefficient between GaN and Si (5.6×10^{-6}/K versus 2.6×10^{-6}/K, respectively) generates extensive tensile stress and, potentially, cracks during the cool-down cycle [53], which requires strain management [54]. The threading dislocation density is slightly higher than for sapphire substrates at $\sim 10^9$ cm^{-2} for thick layers of several μm [54] and even higher for thin films [55]. Threading dislocation densities of 5×10^8 cm^{-2} have been demonstrated using lateral overgrowth techniques in buffer layers of ~3 μm thickness [56]. 4H-SiC (0001) is expensive with a price above USD 1000 for a 2 inch wafer and has a lattice mismatch of -3.5%. Freestanding GaN substrates with a low dislocation density of 10^6 cm^{-2} [57] are expensive at USD 1500 per 2 inch wafer, but result in the best sample quality. These substrates are mainly used for optoelectronic devices that require low dislocation density, such as LDs and superluminescent light emitting diodes [58]. The samples used in this thesis work are grown on such freestanding GaN substrates.

Second, there is a substantial lattice mismatch between the binary III-N compounds, contrary to the case of III-As and III-P, where GaAs/AlAs and GaP/AlP have a negligible lattice mismatch. This makes it more challenging to grow binary III-N heterostructures and reduces the critical thickness for pseudomorphic growth[1]. The lattice mismatch for GaN on AlN, e.g., is +2.5%, wich results in a critical thickness of a few nm, depending on temperature [46]. One way to circumvent the issues related to lattice mismatch is to use AlInN, which is lattice-matched to GaN for an In concentration around 18% [59]. This alloy will be elaborately discussed below.

Third, due to the strong chemical binding between group-III and N atoms, an elevated growth temperature is required to get sufficient adatom diffusion. This is to ensure a 2D step-flow growth mode that maintains a smooth and flat surface, which is essential for high quality QWs (see Section 1.2.3) and waveguides (Chapter 2). The growth technique with the best results in this respect is metal-organic vapor phase epitaxy (MOVPE). Additionally, the quality of AlInN layers is now well-mastered in MOVPE [29, 31, 32], whereas they are less mature in molecular beam epitaxy [60, 61, 62]. Since we heavily rely on high-quality AlInN layers for this thesis work, MOVPE is the growth technique of choice for the samples used here.

Metal-Organic Vapor Phase Epitaxy

MOVPE, also called metal-organic chemical vapor deposition (MOCVD), is the most commonly used growth technique for III-N heterostructures in both academia and industry. With this technique, the substrate is heated to the desired temperature and the required precursors are introduced in the reactor, together with a carrier gas (H_2, N_2 or a mixture of both). The use of H_2 promotes long diffusion length [63], but strongly hinders In incorporation [64], whereas N_2 reduces the mobility and allows good In incorporation. Trimethylgallium (TMGa) or triethylgallium (TEGa), trimethylindium (TMIn), trimethylaluminum (TMAl) and ammonia (NH_3) are

---

[1] An epitaxial film is pseudomorphic to the underlying substrate if it adopts the in-plane lattice constant of the latter. This growth regime can be maintained as long as the elastic strain energy in the layer is smaller than the energy required to generate dislocations or a 2D to 3D growth transition. Below a certain critical thickness, this will be the case and the layer is pseudomorphic. Above the critical thickness, threading and misfit dislocations are generated, or islands are formed, and the layer is relaxed. The critical thickness is reduced with increasing lattice mismatch.

the usual precursors for Ga, In, Al and N, respectively. TEGa is known to produce fewer carbon contamination in the sample, while TMGa allows for a faster growth rate and is cheaper. During growth, the precursors decompose above a heated substrate, the group-III and N atoms are adsorbed on the surface and the byproducts are evacuated by the carrier gas flow. The growth rate and the composition of the growing material can be controlled by acting on the precursor flow and substrate temperature.

Temperature is a key parameter during MOVPE growth. It must be sufficiently high to allow for an efficient decomposition of the precursors (in particular NH_3 is difficult to decompose and requires high temperatures), for an easy desorption of reaction byproducts and for a sufficient diffusion length of the adsorbed species. A high diffusion length is required to ensure step-flow growth and a smooth surface. On the other hand, if the temperature is too high, precursors will decompose before their arrival above the surface, and species will desorb from the surface, thus reducing the growth rate. The optimum growth temperature, which balances out all these different processes, is highly dependent on the group-III element. The III-N bond strength is very strong for Al, intermediate for Ga and weaker for In. As a result, In already has a high diffusion length at relatively low temperatures and easily desorbs at moderate temperatures. The optimum MOVPE growth temperature for InN is therefore around 600°C. Al, on the other hand, has a very low diffusion length and low desorption rate, even at high temperatures. The AlN growth temperature should therefore be at least 1200°C. The case of GaN is intermediate with an optimum around 1000°C. This temperature difference is problematic for the growth of alloys, since good conditions for one species, can be compromising for the others. This is especially true for the AlInN alloy due to the large difference in optimal growth temperature between InN and AlN binary compounds [29].

Growth of thick AlInN cladding layers

High-quality AlInN layers were first demonstrated by Carlin and Ilegems in 2003 at EPFL [59]. They can be grown lattice-matched to GaN for an In composition of ~18%. This results in strain-free GaN/AlInN heterostructures with very interesting properties:

- The large spontaneous polarization mismatch (see Fig. 1.2) leads to the generation of a two-dimensional electron gas (2DEG) at the interface, which is useful for HEMTS [65, 66].
- $Al_{0.82}In_{0.18}N$ has a wider bandgap than that of GaN (~4.5 vs. 3.4 eV at room temperature, respectively [30], see also Section 1.2.1). These materials can therefore be used to form strain-free GaN/AlInN QWs. The strong built-in field in these structures results in a band-to band transition below the GaN bandgap through the QCSE, which is explained in Section 1.2.3 [67], while the large conduction band offset results in inter-subband transitions in the near infrared [52].
- The small refractive index of $Al_{0.82}In_{0.18}N$ compared to that of GaN (see section 1.2.6),

makes it useful for optical confinement in distributed Bragg reflectors (DBRs) [68, 31] or waveguide claddings [34].

In this thesis work, we will exploit this last property to make high-quality optical waveguides. Reviews on the properties and applications of AlInN layers can be found in refs. [28, 29, 30, 69]. In order to optimally benefit from the properties of AlInN stated above, it is crucial to avoid Ga incorporation in the alloy. Indeed, such AlInGaN layers would have properties which are closer to GaN, reducing the contrast in polarization, bandgap and refractive index. In MOVPE reactors with a showerhead design, Ga is always incorporated in AlInN layers, often in even larger concentrations than Al and In [70]. This is due to the the small reactor size and turbulent gas flow of these reactors. Ga-containing deposits on the reactor sidewalls and especially near the showerhead apertures can re-evaporate and incorporate in the deposited AlInN layers. In a horizontal-flow MOVPE reactor such as the AIXTRON 200/4 RF-S system used in this work, Ga incorporation is absent and we obtain pure AlInN layers [71, 42]. The laminar flow in this type of reactor assures that earlier deposits do not reach the substrate.

AlInN is an inherently challenging alloy to grow. Due to the large differences in Al-N and In-N bond length and bond strength, this alloy is sensitive to phase separation [72]. This could lead to degraded material quality with large inhomogeneity and local strain. Additionally, due to the large mismatch in optimal growth temperature between InN (600°C) and AlN (1200°C), it is difficult to combine low In desorption with a high Al adatom mobility. This results in a narrow growth window between 800 - 850°C for In concentrations between 6 and 21% [29]. The strong dependence of the In desorption rate on temperature, makes growth temperature the key parameter to control AlInN composition, rather than, e.g., precursor fluxes. Indeed, it was found that decreasing the growth temperature by a mere 5°C results in an increase in the In concentration of about 1% [73]. The lattice-matching condition is obtained for growth temperatures of ~820°C [69].

The carrier gas used for AlInN growth is generally pure N_2, as H_2 strongly decreases In incorporation [64]. This, together with the limited diffusion length of Al adatoms at these growth temperatures hinders step-flow growth and results in kinetic roughening of the AlInN surface. As a consequence, hillocks are formed during AlInN growth and, beyond a layer thickness of 100 nm, even V-pits [32]. This is shown in Fig. 1.3. The cross-section scanning tunneling electron microscopy (STEM) image in Fig. 1.3(a) shows a severe degradation of the material quality starting at a layer thickness of ~150 nm. The surface of a 50 nm thick layer shows mainly hillocks, as can be seen in the atomic force microscopy (AFM) image shown in Fig. 1.3(b), while the surface of a 100 nm thick layer features a high density of V-pits with surrounding rings (Fig. 1.3(c)). Note that these growth conditions away from thermodynamic equilibrium, which favor kinetic roughening, simultaneously avoid phase separation of the alloy, due to the limited Al mobility. Despite the challenging nature of the growth of this alloy, good quality films can be obtained, especially on freestanding GaN substrates [31].

Since we need at least a 400 nm thick AlInN bottom cladding to ensure a good optical isolation from the GaN substrate (see Section 3.1), and as a smooth interface between the bottom

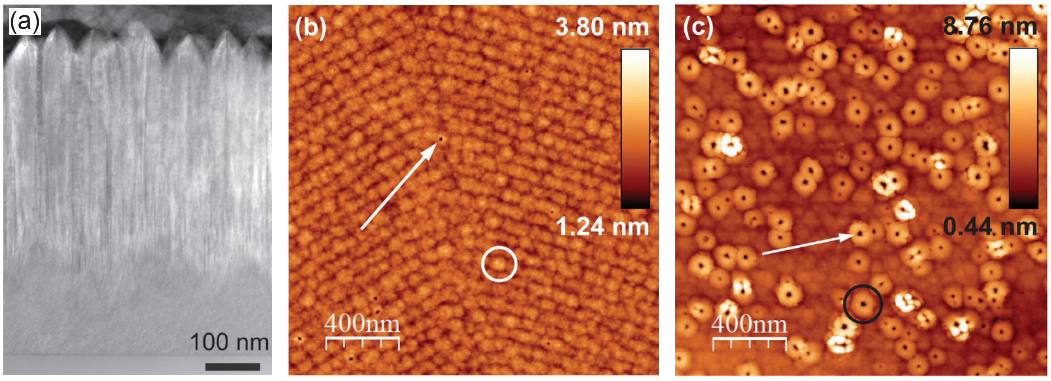

Figure 1.3 – Formation of hillocks and V-pits in thick $Al_{0.8}In_{0.2}N$ layers grown on freestanding GaN. (a) Cross-section Z-contrast STEM image of a 500 nm thick layer shows a severe degradation of material quality beyond an AlInN layer thickness of ~150 nm. (b,c) $2 \times 2\ \mu m^2$ AFM images of (b) 50 nm and (c) 100 nm thick AlInN layers. Two V-defects are pointed by white arrows in (b) and (c). One hillock is circled in white in (b). A ring structure is circled in black in (c). Adapted from ref. [32].

cladding and the active region is required, we need to make use of GaN interlayers to reduce the detrimental impact of kinetic roughening. Hence, after every 50 nm of AlInN, a 5 nm thick GaN interlayer is grown, of which the first 2 nm are grown at the same temperature as the AlInN layer (~820°C) to avoid In evaporation and the remainder is grown at high temperature (~1000°C) and under H_2 to planarize the surface. Note that for a DBR structure in the blue-green spectral region, AlInN layers with a thickness of around 50 nm are by default alternated with GaN layers.

Growth of high-quality GaN/AlGaN QWs

Alloy disorder is a key parameter governing the optical quality of GaN/AlGaN QWs. It is paramount to promote a homogeneous AlGaN composition and abrupt GaN/AlGaN interfaces. This can be done by limiting the Al adatom mobility through a low growth temperature around 870°C and by using N_2 as carrier gas [74]. Similarly to the case of AlInN, this induces some kinetic roughening of the surface, which can lead to slight QW thickness fluctuations. Despite this additional source of inhomogeneous broadening, GaN/AlGaN QWs grown at low temperature and with N_2 as carrier gas have shown superior quality, indicating that well width fluctuations contribute little to the overall inhomogeneous linewidth in this system and that alloy disorder is the main source of inhomogeneous broadening [74].

1.2 Optical Properties

In this section, we will discuss some selected optical properties of III-N semiconductors. Readers with limited knowledge in this topic can find more elaborate discussions in refs. [75, 76, 77].

1.2.1 Band Structure

The key to understanding the interaction of a semiconductor material with light, is to consider its electronic band structure. The latter determines which electronic states exist in the material, and which optical transitions can occur through interactions with a photon.

The origin of the band structure of a crystalline, nearly covalent material can be understood from a simplified picture of the interaction of atomic orbitals. If two atoms are brought close together, their valence orbitals will overlap, interact and hybridize, causing a splitting into a bonding and anti-bonding molecular orbital. The magnitude of the splitting increases with the bond strength and ΔEN.

In an analogous way, the interaction of the valence orbitals of a large number of atoms in a semiconductor crystal lattice creates an equally large number of bonding and anti-bonding states. In the simplified picture of the single electron Hamiltonian, where all interactions with the nuclei and the other electrons are assimilated in a single background potential V_{bg} the electronic states $\phi_q(\mathbf{r})$ with eigenenergies E_q can be found through the time-independent Schrödinger equation:

$$\hat{H}_{1e}\phi_q(\mathbf{r}) = \left[\frac{\hat{p}^2}{2m_0} + V_{bg}(\mathbf{r})\right]\phi_q(\mathbf{r}) = E_q\phi_q(\mathbf{r}), \tag{1.3}$$

where m_0 denotes the free electron mass and the index q refers to the various eigenstates. These states form quasi-continuous energy bands in a crystalline solid. The highest occupied (bonding) band is called the valence band (VB), and the lowest unoccupied (anti-bonding) band is called the conduction band (CB). The energy separation between both is called the bandgap. This bandgap is a key parameter in the optical properties of a semiconductor. The most fundamental optical process in a semiconductor is the transition of an electron from the valence to the conduction band (or vice versa) by absorption (emission) of a photon with the corresponding energy. Just like in the case of the two-atom molecule, there is a general trend that the bandgap will be larger for materials with a large bond strength. For this reason, the bandgap in the relatively weakly bound InN is small (0.7 eV at low temperature, corresponding to a photon in the near infrared (IR)), the bandgap in GaN is intermediate (3.5 eV, in the near UV) and the bandgap of AlN is very large (6.2 eV, in the deep UV) [78]. With these values, the III-N material system spans a wide range of photon energies from the near IR to the deep UV. Intermediate bandgaps can be reached by alloying the binary compounds, as shown in Fig. 1.4. Note that these alloys cannot all be grown with high quality. Especially those with a large lattice mismatch from the available substrates such as GaN and AlN, are challenging to grow. The bandgap energy $E_g^{A_xB_{1-x}}$ of an alloy of materials A and B cannot be correctly determined

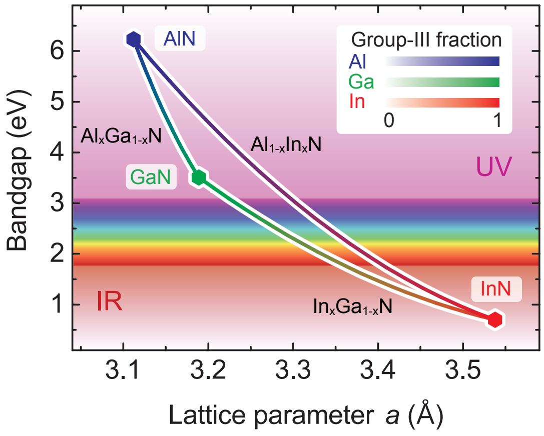

Figure 1.4 – Low-temperature bandgap and basal plane lattice parameter a of unstrained group-III nitrides as a function of alloy composition (color scale). The bandgap energy of this material system can be tuned from the infrared (IR) over the visible to the deep UV by adjusting the alloy composition.

by applying Vegard's law on the respective bandgaps E_g^A and E_g^B. A corrective term is required:

$$E_g^{A_xB_{1-x}} = E_g^A x + E_g^B(1-x) + bx(1-x). \tag{1.4}$$

The parameter b is called the bowing parameter and has a value of -0.70 eV for AlGaN [78], -1.7 eV for InGaN [79], and a debated value of -5.4 eV for AlInN [69].

When the lattice temperature of a semiconductor is increased, the material expands and the atomic orbital overlap decreases. As a result, the bandgap energy decreases as well. This can be described by Varshni's semi-empirical law [80]:

$$E_g(T) = E_g(0) - \frac{\alpha_V T^2}{\beta_V + T}, \tag{1.5}$$

where $E_g(0)$ is the bandgap of the material at 0 K and α_V, β_V are the Varshni parameters. However, a more accurate model (especially for low temperatures), based on the Bose-Einstein occupation of phonon states, is given by [81]

$$E_g(T) = E_g(0) - \frac{2\alpha_B}{\exp(\Theta_B/T) - 1}, \tag{1.6}$$

where α_B is an electron-phonon coupling constant and Θ_B is an average phonon temperature. For bulk (Al)GaN layers, the values of these parameters are $\alpha_B = 75$ meV and $\Theta_B = 370$ K [82].

In a way similar to temperature variations, the bandgap also changes due to strain. Indeed, as the distance between atoms is decreased (increased) under compressive (tensile) strain, the bandgap increases (decreases) according to the overlap and interaction between atomic orbitals [83]. Since we are dealing with nearly strain-free structures in this work, we will not go into further details here.

Since the CB and VB states are eigenstates of a crystal with translational symmetry, which is supposed infinite for mathematical simplification, they are plane-wave-like states (called Bloch states) with a well-defined wavevector $\mathbf{k}$. Due to the periodicity of the lattice, only a limited number of wavevectors are effectively unique, the ones in the so-called first Brillouin zone.[2] A state with a wavevector outside this zone is essentially the same as that of a state belonging to the first Brillouin zone. We can therefore limit the $\mathbf{k}$-space we consider to the first Brillouin zone. Since a state with a different $\mathbf{k}$-value will experience a different periodicity and depth of the lattice potential, it will have a different energy. Therefore, the energy bands will be distributed across the Brillouin zone. Due to the enormous amount of particles and interactions in a solid, such a band dispersion cannot be calculated exactly. A solution for GaN, based on the GW approximation, was calculated by Carvalho *et al.* [84] and is given in Fig. 1.5(a). The VB maximum and CB minimum occur at the center of the first Brillouin zone, i.e. for $\mathbf{k} = \mathbf{0}$, also called the Γ-point. This means that a single photon –which has a negligible wavevector of $\frac{En_r}{\hbar c} \approx 50\ \mu\text{m}^{-1}$ at these energies E, with n_r the real part of the refractive index, $\hbar$ the reduced Planck constant and c the vacuum speed of light– can comply with both energy and momentum conservation laws of an electronic transition between the VB maximum and CB minimum. This type of transition is called a direct interband optical transition. In the situation where the CB minimum and VB maximum do not occur at the same wavevector (which is the case, e.g., for Si and Ge), an indirect band transition involving a phonon is required in addition to the photon emission/absorption to fulfill momentum conservation. Such an indirect transition is a three-body process (electron, phonon and photon) and therefore much less likely to occur than the two-body direct transition. As a result, direct bandgap semiconductors such as III-Ns, ZnO or GaAs have a much stronger light-matter interaction than indirect bandgap semiconductors such as Si.

In an intrinsic or undoped semiconductor –i.e. without any impurities–, the position of the Fermi level lies close to mid-gap, meaning that the VB is almost entirely populated with electrons, and the CB is almost empty. It is therefore convenient to introduce the hole as an unoccupied state in the VB. We will henceforth use the words *electron* and *hole*, to discuss occupied electron states in the CB and unoccupied electron states in the VB, respectively. Due to the relatively small value of the thermal energy $k_B T$ (~25 meV at room temperature), only the states in the immediate vicinity of the VB and CB extrema will be populated with holes and electrons, respectively, at room temperature or below. We can therefore neglect most of the lower and upper lying bands and focus only on those close to the bandgap region. Therefore, as a further simplification, we can apply the effective mass approximation, where we can write

---

[2] A more detailed discussion on Bloch states and the reciprocal or $\mathbf{k}$-space can be found in ref. [75].

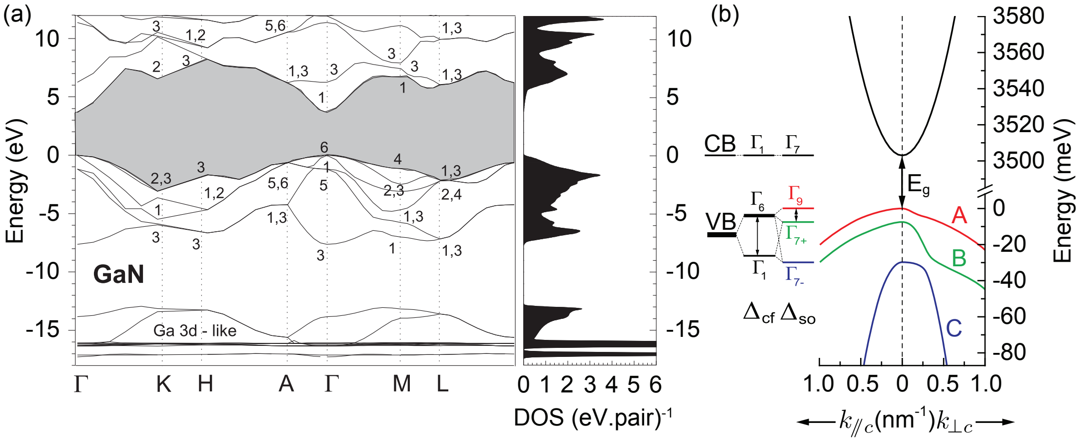

Figure 1.5 – GaN band structure. (a) Complete band structure over the entire first Brillouin zone as calculated using the GW approximation. The corresponding density of states (DOS) is also shown. The forbidden gap is marked in grey. Adapted from ref. [84]. (b) Detail of the CB and VB dispersion around the Γ-point, as calculated with the $k \cdot p$ formalism [85], for a wavevector parallel ($k_{//c}$) and perpendicular ($k_{\perp c}$) to the c-axis, including the crystal-field and spin-orbit splitting in the VB.

the conduction (E_c) and valence band energy (E_v) as

$$E_c(\mathbf{k}_e) = E_g + \frac{\hbar^2 k_e^2}{2m_e^*}, \tag{1.7a}$$

$$E_v(\mathbf{k}_h) = -\frac{\hbar^2 k_{h//c}^2}{2m_{h//c}^*} - \frac{\hbar^2 k_{h\perp c}^2}{2m_{h\perp c}^*}, \tag{1.7b}$$

taking zero energy at the VB maximum. Here, we introduced the effective masses m_e^*, $m_{h//c}^*$ and $m_{h\perp c}^*$ of the electron and hole, parallel and perpendicular to the c-axis, respectively. Due to the lattice anisotropy, the VB has a different curvature –and consequently, a different effective mass– for these two directions. Since the VB has a concave dispersion near the Γ-point, a VB electron will have a negative effective mass. A hole will therefore behave as a particle with positive mass. We can consider the electron and hole as particles with an effective mass, that is different from the free-electron mass, as a consequence of the interaction with the crystal potential.

Like in most other semiconductors, the CB in III-Ns has s-orbital-like symmetry, while the VB has p-like symmetry. Therefore, the CB is almost perfectly isotropic and non-degenerate, while the VB is expected to be threefold degenerate in a cubic lattice with p_a, p_m and p_c-like bands, aligned along the a-, m- and c-axis, respectively. Due to the uniaxial anisotropy of the wurtzite lattice however, the p_c-band is shifted toward lower energies with respect to the other two. The crystal field splitting is given by $\Delta_{cf} = 22$ meV in GaN [86]. Due to spin-orbit interaction, the degeneracy of the other two bands is equally lifted, with $\Delta_{SO} = 15$ meV [86]. This is illustrated in Fig. 1.5(b). The final subvalence bands exhibit Γ_9, Γ_{7+} and Γ_{7-} symmetry and are called the heavy-hole (hh) or A, light-hole (lh) or B and split-off (so) or C bands. The transitions occurring between the respective VBs and the CB are also called A, B and C. The band dispersion around the Γ-point, as calculated with the $k \cdot p$ formalism [85], is equally shown in Fig. 1.5(b). The CB is almost perfectly isotropic and parabolic as explained above, while this is not the case for the subVBs. The uniaxial lattice anisotropy leads to anisotropic effective masses and the observed non-parabolicities are a consequence of p-orbital repulsion. Therefore, the effective mass approximation is more flawed for the VB.

1.2.2 Excitons and Biexcitons

If an electron and a hole coexist in relative proximity in a semiconductor, their opposite charge will cause a Coulomb attraction, in a way similar to that of a proton/positron and electron in free space. Consequently, the electron and the hole will bind and form an exciton, which is analogous to the hydrogen or positronium atom. In a bulk semiconductor, the exciton will have an energy that is lower than the bandgap E_g for an exciton momentum $\mathbf{K}=\mathbf{0}$ with eigenenergies of the form [77]

$$E_X = E_g + \frac{\hbar^2 K^2}{2M^*} - \frac{Ry^*}{n^2}, \tag{1.8}$$

with $M^* = m_e^* + m_h^*$ the exciton mass, $\mathbf{K} = \mathbf{k}_e + \mathbf{k}_h$ the exciton wavevector, Ry^* the effective Rydberg energy and $n \in \mathbb{N}^*$ the principal quantum number. Ry^* is also called the exciton binding energy E_B and is equal to [77]

$$Ry^* = E_B = Ry \frac{\mu}{m_0} \frac{1}{\varepsilon_{rel}^2}, \tag{1.9}$$

with $Ry = 13.6$ eV the hydrogen Rydberg energy, $\varepsilon_{rel} = \frac{\varepsilon}{\varepsilon_0}$ the relative permittivity or dielectric function of the semiconductor and

$$\mu = \frac{m_e^* m_h^*}{m_e^* + m_h^*}, \tag{1.10}$$

the reduced exciton mass. In analogy to the hydrogen atom, we can define an exciton Bohr

Table 1.2 – Exciton parameters in bulk III-Ns, GaAs and ZnO. Data are taken from [95, 78] unless stated otherwise. a_B was calculated from Eq. 1.11.

	GaN	AlN	InN	GaAs	ZnO
$E_g(T=0\,\mathrm{K})(\mathrm{eV})$	3.50	6.2	0.7	1.519	3.437 [77]
m_e^*/m_0	0.2	0.3	0.07	0.065	0.28 [77]
$m_{hh//}^*/m_0$	1.8 [90]	3.1 [90]	0.35	0.47 [77]	0.59 [77]
$m_{hh\perp}^*/m_0$	1.6	6.3	0.35		0.45 [77]
E_B (meV)	25 [91]	56 [92]	4 [93]	4.9 [76]	59 [94]
a_B (nm)	3.5	1.8	12	11.2 [76]	1.8 [94]

radius [77]

$$a_B = a_B^H \varepsilon_{rel} \frac{m_0}{\mu} = a_B^H \frac{Ry}{Ry^*} \frac{1}{\varepsilon_{rel}}, \tag{1.11}$$

with a_B^H the hydrogen Bohr radius. The exciton Bohr radius determines the size of the exciton and the volume over which it averages the lattice potential. In inorganic semiconductors, ε_{rel} is typically large and the Coulomb-interaction will be screened by valence electrons. Consequently, the Bohr radius will span several unit cells. This type of delocalized exciton is called Wannier-Mott exciton [87]. In materials with a low dielectric function, such as organic materials and alkali halides, the excitons are localized and are called Frenkel excitons [88, 89]. In the remainder of this text, we will exclusively focus on Wannier-Mott excitons and call them excitons for short.

Since the exciton ground state is E_B below the energy of a free electron-hole (e-h) pair, excitons will be the dominant species as long as the thermal energy $k_B T < E_B$. The values of binding energies and Bohr radii of excitons in bulk III-nitrides are given in Tab. 1.2, together with the values for GaAs and ZnO. With a binding energy of 25 meV, excitons exist up to room temperature in GaN. As can be seen from Eq. 1.11, semiconductors which have a large exciton binding energy, have a small exciton Bohr radius. Since the Bohr radius determines the volume over which the exciton probes the lattice potential, a small a_B, will cause an increased sensitivity to disorder. Indeed, crystal disorder on a scale much smaller than a_B will not have an impact on the average potential felt by the exciton, while disorder over equal or larger length scales will create an energy landscape in the material.

As a general trend, the effective masses increase, the exciton Bohr radius decreases and the exciton binding energy increases with increasing bandgap [77], as summarized in Tab. 1.2.

It is also possible for two electrons and two holes to bind together in a semiconductor. This quasi-molecule is called a biexciton (XX). Since a biexciton consists of 2 excitons bound together

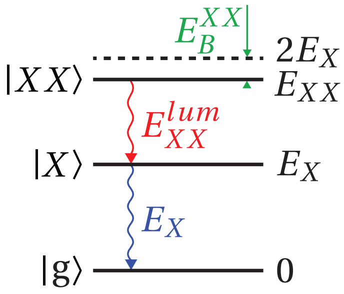

Figure 1.6 – Schematic representation of the biexciton-exciton cascade. The biexciton state $|XX\rangle$, exciton state $|X\rangle$ and ground state $|g\rangle$ are shown with their respective energies, together with the optical decay from $|XX\rangle$ to $|X\rangle$, and from $|X\rangle$ to $|g\rangle$.

by the biexciton binding energy E_B^{XX}, its eigenenergy can be written as

$$E_{XX} = 2E_X - E_B^{XX}. \tag{1.12}$$

In luminescence experiments, however, a biexciton will not emit a photon corresponding to its eigenenergy, but it will leave behind an exciton of energy E_X and emit a photon of energy

$$E_{XX}^{lum} = E_X - E_B^{XX}. \tag{1.13}$$

This process is called the biexciton-exciton cascade and is represented in Fig. 1.6.

1.2.3 III-Nitride Quantum Wells

A QW is a structure where electrons and/or holes are confined in a thin 2D layer. This is realized by sandwiching a narrow band-gap material in between two layers of a wider band-gap barrier material. A QW where the electron and hole are both confined in the same layer is called a type I QW, while in a type II QW, they are confined in adjacent layers. We will only discuss type I configuration here. There are three main advantages to the use of QWs over bulk semiconductors in optoelectronic devices such as LEDs and LDs and for applications in light-matter coupling.

First, the radiative recombination rate is increased for both excitons and unbound e-h pairs [76, 96]. This results in a higher radiative efficiency as the contribution of non-radiative recombination is reduced. In a perfect and infinite bulk semiconductor, an exciton can recombine and emit a photon, but this photon will soon be reabsorbed as an exciton. These so-called Rabi-oscillations give rise to the formation of exciton-polaritons, which will be further explained in Section 2.3. A bulk semiconductor can therefore only luminesce due to imperfections, either due to the presence of a surface –when the photon crosses the surface and is outside the material, it can not be reabsorbed anymore–, or due to disorder in the material. A photon that is emitted from the low-energy tail of the broadened band edge of a disordered material is less likely to be reabsorbed, as its energy is below the absorption edge of a large part of the sample. A QW breaks the symmetry in much the same way as a surface does. 2D excitons are coupled to 3D photons, which opens a channel for radiative decay. In the case of unbound e-h pairs, QWs offer an additional advantage with respect to the enhanced radiative decay by symmetry breaking. Since the electron and hole are required to be spatially close together in order to recombine, randomly wandering charge carriers recombine relatively slowly in the bulk. When introducing a QW however, electrons and holes are confined in the same layer, and hence have higher probability to meet, which leads to an increased radiative recombination rate.

Second, the transition energy can be tuned by varying the QW width d_{QW} [76]. This gives an additional pathway for bandgap engineering besides alloying. Since we are creating a particle-in-a-box, we add a nonzero confinement energy (the ground state energy of the particle-in-a-box model) to both the electron and hole states which increases with decreasing well width. For very large widths (larger than the exciton Bohr radius or the electron/hole de Broglie wavelength), the confinement energy vanishes and the states are at their respective bulk energies. In such a case, since there is no quantum confinement effect, we call this structure a double heterostructure, rather than a QW. The envelope wavefunction of a confined electron state Ψ_e and of a confined hole state Ψ_h in the QW forms a standing-wave pattern in the created potential well. This puts a restriction on the allowed wavevector components perpendicular to the QW-plane $k_{\perp QW}$, which will be quantized. We get a series of discrete states with confinement energy $E^q_{conf}(d_{QW})$, with $q \in \mathbb{N}^*$ the confinement quantum number. For a QW with infinite barrier height, this can be written as [76]

$$E^q_{conf}(d_{QW}) = \frac{\hbar^2 k^2_{\perp QW}}{2m^*_{\perp QW}}, \text{ with } k_{\perp QW} = \frac{q\pi}{d_{QW}}, \tag{1.14}$$

where $m^*_{\perp QW}$ is the effective mass of the confined particle, for motion perpendicular to the QW plane. For a limited barrier height, the evanescent tails of the envelope wavefunction in the barrier –and therefore the effective QW width– depend on the effective carrier mass. The number of confined states that can exist in the QW are determined by the height of the potential barrier. The energy of a QW e-h pair, in absence of any excitonic features, can be written as

$$E_{QW} = E_g + E^q_{h,conf}(d_{QW}) + E^q_{e,conf}(d_{QW}) + \frac{\hbar^2 k^2_{h//QW}}{2m^*_{h//QW}} + \frac{\hbar^2 k^2_{e//QW}}{2m^*_{e//QW}}, \tag{1.15}$$

where $k^2_{h//QW}$, $k^2_{e//QW}$, $m^*_{h//QW}$ and $m^*_{e//QW}$ represent the squared wavevector magnitude and effective mass of the electron and hole in the QW plane, respectively. Here, we supposed a QW with an isotropic effective carrier mass in the QW plane, which is true for c-plane III-N QWs or zinc-blende QWs. For anisotropic QWs, such as m-plane III-N QWs, terms must be added accordingly [97]. In this work, we will focus on isotropic c-plane III-N QWs. We will mainly focus on the ground state with $q = 1$.

Third, the exciton binding energy can be larger than in the bulk case, sustaining excitonic effects at higher temperatures, as explained below.

In the III-N material system, several material combinations are possible to construct a QW: InGaN/(In)GaN QWs emitting in the near UV to green spectral region are used in LEDs and LDs, (Al)GaN/AlGaN QWs for UV optoelectronic devices, and GaN/$Al_{0.82}In_{0.18}N$ QW that are lattice-matched. In III-N QWs, the valence band offset is smaller than the CB offset between different materials, according to a 70:30 ratio [98]. This is because of the common anion (N) in all materials and the fact that the VB is related to the anion p-orbitals. This heuristic principle is called the common anion rule [99].

2D Excitons

The energy of a 2D exciton in an ideal QW with infinite barriers and vanishing width, can be written as [77]

$$E_X = E_g + E^q_{h,conf}(d_{QW}) + E^q_{e,conf}(d_{QW}) + \frac{\hbar^2 K^2_{//QW}}{2M^*} - \frac{Ry^*}{(n-1/2)^2}, \tag{1.16}$$

where n represents the exciton principle quantum number. Looking at the last term of Eq. 1.16, we see that the exciton binding is increased with respect to the 3D case. For the $1s$ exciton state ($n = 1$), E_B is enhanced by a factor of 4 in the perfect 2D case [100, 101]. In a real QW however, due to the finite barrier height and the resulting evanescent tail of the wavefuction in the barrier, the confinement is limited and the enhancement is thus also limited to a factor ~2 at best [102]. In GaN/$Al_{0.2}Ga_{0.2}N$ QWs, a binding energy of 48 meV has been demonstrated [103].

Quantum-Confined Stark Effect

In III-N heterostructures grown along a polar or semi-polar axis, the polarization discontinuity creates charge planes at the interfaces. In a QW, two charge planes of opposite sign, σ^+ and σ^-, are formed at the two well/barrier interfaces. These charge planes induce an electric field F in the QW which changes the rectangular potential well (shown in Fig. 1.7(a)) to a triangular potential well (Fig. 1.7(b)). This has two main consequences: E_{QW} is reduced as the electron and hole energy levels are brought closer together, and the electron (Ψ_e) and hole envelope wavefunctions (Ψ_h) are separated to opposite sides of the well. This is commonly called the QCSE [104].

In case of a field-free QW, E_{QW} is equal to the bandgap plus the electron and hole confinement energies, according to Eq. 1.15. When the QW width is increased, the confinement energy is decreased and E_{QW} approaches the bulk bandgap, as shown in Fig. 1.7(c). When a built-in field F is present, however, we have to add a term to Eq. 1.15 to include the reduction of E_{QW} due to F [99]:

$$E_{QW}^{QCSE} = E_g + E_{h,conf}^{q}(d_{QW}) + E_{e,conf}^{q}(d_{QW}) + \frac{\hbar^2 k_{h//QW}^2}{2m_{h//QW}^*} + \frac{\hbar^2 k_{e//QW}^2}{2m_{e//QW}^*} - eFd_{QW}. \tag{1.17}$$

When we increase the thickness of such a well, the last term of Eq. 1.17 continues to reduce the QW energy, even below the bulk bandgap value [104]. This is equally depicted in Fig 1.7(c). Beyond a certain width, the electron and hole envelope wavefunctions are far away from the opposite side and the local well shape is invariant under d_{QW}. In this situation, E_{conf} is constant and E_{QW} changes with a slope of $-eF$ with respect to d_{QW}.

Due to the triangular well shape, the electron and hole are pushed to opposite sides of the QW. This results in a significant reduction of the wavefunction overlap for wider wells. As a consequence, the exciton binding energy and the light-matter interaction (see Section 1.2.4) are reduced, as shown in Fig. 1.7(d). This reduced exciton binding energy leads to a smaller redshift of the exciton under the QCSE, compared to an unbound e-h pair.

Note that the effects of QCSE can be reduced by using narrow wells. QCSE has a small impact below a well width of typically 2 nm [104]. In this regime, the confinement energy is larger than eFd_{QW} and E_{QW} exceeds the bulk bandgap energy.

In multiple (M)QW structures, where many periods of barrier and well material are repeated, the built-in field in the QWs is reduced compared to the single QW case, due to the geometric effect [105]. Free carriers in the structure will screen any potential drop over long distances (typically > 10 nm). This implies that a periodic MQW structure, which extends over more than several 10s of nm, will have a zero net potential difference over one period. In this approximation, which agrees well with experiments [106], the barriers accommodate part of the electric-field strength, which leads to a reduction in the built-in electric field compared to a single QW, and hence resulting in moderated QCSE effects in the QWs.

1.2.4 Light-Matter Interaction

The interaction between the electronic states of a medium and the vacuum light-field with angular frequency ω can be treated by time-dependent perturbation theory. Here, we will focus on transitions between the VB and CB. In the electric dipole approximation, the interaction Hamiltonian is given by [76]

$$H_{int} = -e\mathbf{r}\cdot\mathbf{E}. \tag{1.18}$$

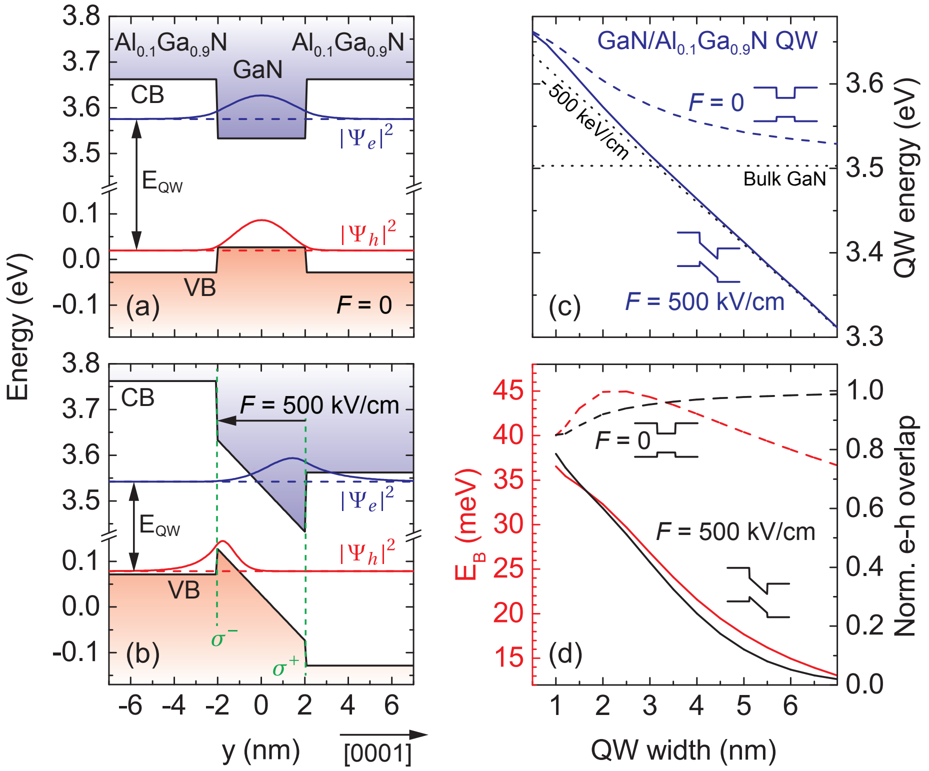

Figure 1.7 – QCSE in a *c*-plane GaN/$Al_{0.1}Ga_{0.9}N$ QW. (a) Band structure of a single hypothetical field-free 4 nm thick QW. The electron (blue) and hole (red) wavefunctions of the first excited state are symmetric with respect to the growth direction. (b) More realistic band structure of the same structure with a built-in electric field of 500 kV/cm. The barriers are supposed infinite in the + and -*c* direction and therefore field-free. The electron and hole wavefunctions are spatially separated due to the triangular potential well and their overlap is reduced. Also the energy separation between the electron and hole (E_{QW}) is reduced with respect to the field-free case shown in (a). (c) QW energy as a function of well width for the case of a field-free GaN/$Al_{0.1}Ga_{0.9}N$ QW (dashed line) and the same QW with $F = 500$ kV/cm (solid line). As the QW width increases, the confinement energy is reduced and the QW energy converges toward the bulk GaN bandgap for $F = 0$. In a triangular well however, E_{QW} keeps decreasing below the bulk bandgap energy. (d) Exciton binding energy E_B (red) and electron-hole overlap (black) for the same cases of $F = 0$ (dashed line) and $F = 500$ kV/cm (solid line). In a field-free QW, these quantities remain high as the well width is increased. Under the influence of the built-in electric field however, both quantities are rapidly reduced with increasing well width.

The interband transition probability, or transition rate is determined by Fermi's golden rule [75, 76]. The absorption rate between a VB state $|v\rangle$ with energy E_v and wavevector $\mathbf{k}_h$ and a

CB state $|c\rangle$ with energy E_c and wavevector $\mathbf{k}_e$ is given by

$$R_{cv}(\hbar\omega) = \frac{2\pi}{\hbar} \sum_{\mathbf{k}_h,\mathbf{k}_e} |\langle c|H_{int}|v\rangle|^2 \delta(E_c(\mathbf{k}_e) - E_v(\mathbf{k}_h) - \hbar\omega), \tag{1.19}$$

where the Dirac delta assures we take the sum over only those VB and CB states that are separated by the photon energy $\hbar\omega$.

The matrix element of the Hamiltonian can be written as

$$|\langle c|H_{int}|v\rangle| = -eE_0 |\langle c|\mathbf{r}\cdot\mathbf{e}_E|v\rangle| = -eE_0 |\mathbf{r}_{cv}|, \tag{1.20}$$

with $\mathbf{r}_{cv} = \langle c|\mathbf{r}\cdot\mathbf{e}_E|v\rangle$ the interband optical matrix element, $\mathbf{e}_E$ the light polarization vector, i.e. a unit vector parallel to $\mathbf{E}$, E_0 is the electric field associated with one photon in mode volume V, and can be written as [75]

$$E_0^2 = \frac{2\omega\hbar}{\varepsilon V}. \tag{1.21}$$

Note that the electric field can be enhanced, together with the light-matter interaction, by confining photons in a smaller volume V. The concept of radiative decay of an electronic excitation depending on the photonic environment, was first proposed by Purcell in 1946 [107]. This idea will be further elaborated in Chapter 2.

The optical matrix element can be determined from the Kane energy E_P, which is roughly constant in III-V semiconductors (17-22 eV [75]) and amounts to 17 eV for GaN [90].

$$|\mathbf{r}_{cv}| = \frac{\hbar}{E_g}\sqrt{\frac{E_P}{2m_0}}. \tag{1.22}$$

From Eq. 1.22, we can see that small-bandgap semiconductors have an increased optical matrix element. In the case of a QW, the transition rate is increased as the e-h wavefunction overlap is increased and both carriers share the same k_y if $q_e = q_h$. The optical matrix element then becomes [108]

$$|\mathbf{r}_{cv}| = |\langle c|\mathbf{r}\cdot\mathbf{e}_E|v\rangle|_{xz}\int_{-\infty}^{+\infty}\Psi^*_{e,q_e}(y)\Psi_{h,q_h}(y)dy (= 0 \text{ if } q_e \neq q_h), \tag{1.23}$$

where the subscript xz implies that the integral should be taken over the x and z directions only, contrary to Eq. 1.20. We see that the optical matrix element crucially depends on the overlap of the electron and hole envelope wavefunction in a QW. In the case of a QW with built-in electric field, such as in III-nitrides, this overlap –and therefore also the light-matter interaction strength– heavily depend on the QW width. In the Kane approximation, $|\mathbf{r}_{cv}|$ is constant to first order in k around the VB and CB extrema [109]. This means that we can bring the matrix element out of the summation of Eq. 1.19 and we can replace the summation by the joint density of states (JDOS, i.e. the density of states that are connected by an optical transition) D_{cv}, expressed per unit of energy and per unit of volume of material [76]

$$D_{cv}(\hbar\omega) = \sum_{\mathbf{k}_h,\mathbf{k}_e}\delta(E_c(\mathbf{k}_e) - E_v(\mathbf{k}_h) - \hbar\omega) = \frac{2}{(2\pi)^d}\int\frac{dS_{\mathbf{k}}}{|\nabla_{\mathbf{k}}(E_c - E_v)|}. \tag{1.24}$$

The prefactor 2 is coming from the spin degeneracy. $S_{\mathbf{k}}$ is the constant energy surface defined by $E_c - E_v = \text{const.}$ and d is the dimensionality of the system. Solving the integral for 2 and 3 dimensions with the band dispersion from Eqs. 1.7a and 1.7b gives [75]

$$D^{3D}_{cv}(\hbar\omega) = \frac{1}{2\pi^2}\left(\frac{2m_r}{\hbar^2}\right)^{\frac{3}{2}}\sqrt{\hbar\omega - E_g} \text{ for } \hbar\omega \geq E_g, \tag{1.25a}$$

$$D^{2D}_{cv}(\hbar\omega) = \frac{m_r}{\pi\hbar^2} \text{ for } \hbar\omega \geq E_g + E_{h,conf} + E_{e,conf}, \tag{1.25b}$$

while $D_{cv} = 0$ below the bandgap. We find that the JDOS mainly depends on the reduced masses of the VB and CB. Wide-bandgap semiconductors (with elevated electron and hole masses) have a larger JDOS. In a 3D semiconductor, we notice a square root continuous increase of the JDOS with energy. In a QW on the other hand, it increases in a staircase way. If multiple confined states ($q = 2,3,\ldots$) exist in the QW, we get a piecewise constant staircase shape for D^{2D}_{cv}.

Finally, we get

$$R_{cv}(\hbar\omega) = \frac{2\pi e^2}{\hbar}E_0^2|\mathbf{r}_{cv}|^2 D_{cv}(\hbar\omega). \tag{1.26}$$

In this form, we can clearly see the separate contributions from the optical mode (E_0), the wavefunction symmetry ($\mathbf{r}_{cv}$) and the band dispersion (D_{cv}).

We can define the interband oscillator strength, a dimensionless physical quantity, which describes the strength of the quantum coupling between the two states, as [75]

$$f_{cv} = \frac{2m_0\omega_{cv}|\mathbf{r}_{cv}|^2}{\hbar}. \tag{1.27}$$

In the case of excitons, the oscillator strength is concentrated in a volume of the order of the Bohr radius. Therefore, we express the excitonic oscillator strength as [108]

$$f_X^{3D} = f_{cv}\frac{1}{\pi(a_B)^3} \text{ for 3D excitons,} \tag{1.28a}$$

$$f_X^{2D} = f_{cv}\frac{8}{\pi(a_B)^2} \text{ for 2D excitons,} \tag{1.28b}$$

per unit of volume and per unit of area, respectively. Wide bandgap semiconductors typically have a large oscillator strength, due to their small exciton Bohr radius, and hence a strong light-matter coupling. As a result, the exciton oscillator strength is almost an order of magnitude larger in GaN/AlGaN QWs, ($f_X^{2D} = 2.1\times10^{13}$ cm^{-2}) [110], compared to InGaAs/GaAs QWs ($f_X^{2D} = 4.8\times10^{12}$ cm^{-2}) [111]. This, together with the elevated exciton binding energy in III-nitrides, makes this material system an interesting platform for strong light-matter coupling applications.

Optical Selection Rules

Since the hh-band is exclusively composed of p_a- and p_m-orbitals, it does not interact with light that is polarized $//c$. Therefore, the A-transition is optically forbidden for light polarization $//c$. B- and C-transitions on the other hand, are allowed in both polarization directions. The interband oscillator strength values for unstrained GaN are given in Tab. 1.3. The relative oscillator strengths obey the Thomas-Reiche-Kuhn sum rule $\sum_{i=A,B,C} f_{cv_i}^{E\perp c} = \sum_{i=A,B,C} f_{cv_i}^{E//c} = 1$. This rule states that if the oscillator strengths are distributed over several levels, the sum of the transition rates must equal the classically derived quantity. Since the A subband does not interact with light polarized along the c-axis, the effective bandgap is larger for this polarization.

For strained GaN, the oscillator strengths can drastically change [83, 97]. The oscillator strength of the A transition is insensitive to isotropic strain in the c-plane, since it consists of only p_m and p_a orbitals.

	$f_{osc}^{E\perp c}$	$f_{osc}^{E//c}$
A	0.5	0
B	0.44	0.12
C	0.06	0.88

Table 1.3 – Relative oscillator strength of the A, B and C interband transitions in unstrained bulk GaN at the Γ-point, as calculated using the $k\cdot p$-method [85].

Since the spin of the A subband is $\pm\frac{3}{2}$ and the spin of the CB, and that of the B and C bands is $\pm\frac{1}{2}$, the total spin of an exciton or e-h pair is 0, ±1 or ±2. A photon carries a spin ±1 and can only couple to excitons and e-h pairs with the same spin.

In addition to the polarization and spin selection rules, there are the **k** selection rules. In a bulk semiconductor, the exciton wavevector or $\mathbf{k}_e+\mathbf{k}_h$ must exactly match the wavevector of a photon with the correct energy. Otherwise, the recombination cannot take place without assistance of a phonon. In a QW, the selection rules are relaxed, as only the in-plane wavevector is conserved in the recombination process (there is no translation symmetry in the direction $\perp$ QW.) In this case, the exciton wavevector or $\mathbf{k}_e+\mathbf{k}_h$ must be within the light cone, i.e. it must be smaller than the photon wavevector. This is further explained in Section 2.3.4.

Excitons (and e-h pairs) whose radiative recombination is allowed under these selection rules are called bright excitons (e-h pairs), while those whose transition is optically forbidden are called dark excitons (e-h pairs).

1.2.5 Inhomogeneity, Broadening and Localization

Disorder is a central aspect to explain the behavior of electrons, holes and excitons in semiconductors. Variations in the local environment alter the energy of the VB, CB and potentially the bandgap. In bulk semiconductors, this can be due to point defects, such as impurities or dopants, or a variation of the strain state around dislocations [112]. In alloys, there is additionally disorder from variations in composition, such as phase separation or cluster formation, while QW states may experience disorder originating from well width fluctuations, interface roughness and the alloy disorder described above.

These various sources of disorder lead to inhomogeneous broadening of the band-edge and excitonic transitions. As a result, a variation in the transition energy is induced and the excitons, electrons or holes experience a potential landscape. Since excitons, electrons and holes probe the environment over a volume determined by their Bohr radius and de Broglie wavelength, respectively, they will experience the average potential of this region. Excitons with a large Bohr radius will therefore be less prone to inhomogeneous broadening. Consequently, wide bandgap semiconductors, such as GaN, with a small a_B, exhibit a more pronounced inhomogeneous broadening than comparable semiconductors with a smaller bandgap and similar crystalline quality.

In such a potential landscape and at low temperatures, species preferably occupy the lowest-energy states. Consequently, the peak emission energy (determined by the occupied states) will be lower than the peak absorption energy (determined by all available states). This process is called localization and the energy difference between the absorption and emission peak is called the Stokes shift (SS).

Besides inhomogeneous broadening γ_{inh} of the transition energy (which is accounted for using a Gaussian distribution), there is also homogeneous broadening γ_{hom}, which follows a Lorentzian lineshape. This can be due to two reasons, lifetime broadening, which is a result of Heisenberg uncertainty, $\Delta E = \frac{\hbar}{\Delta t}$, and phonon broadening. In semiconductors, the exciton lifetime is so long (from several 100 of ps to several ns), that lifetime broadening is negligible. We will therefore only consider phonon broadening here, which can be written as [113, 114]

$$\gamma_{hom}(T) = aT + \frac{b}{exp\left(\frac{E_{LO}}{k_B T}\right) - 1}, \tag{1.29}$$

where E_{LO} represents the longitudinal optical (LO) phonon energy, and a and b represent the coupling to the acoustic and LO-phonons, respectively.

Of the binary/ternary III-nitride QW structures, GaN/AlGaN QWs have the smallest γ_{inh} value. This is mainly because they are free of In and because the GaN well –which hosts the largest part of the carrier wavefunction– is a binary material and therefore free of any alloy disorder. Since InN has a much lower bandgap and much larger lattice parameters compared to GaN and AlN, as shown in Fig. 1.4, heterostructures with In are heavily strained (even at low In concentrations) and an In atom in the lattice changes the local potential substantially. Consequently, InGaN/-GaN or GaN/AlInN QWs typically are more prone to disorder and exhibit larger inhomogeneous linewidths. As a result of this increased γ_{inh}, it is much more challenging to achieve the strong light-matter coupling regime (explained in Section 2.3) using InGaN/GaN QWs [110].

1.2.6 Refractive Index

Bulk III-Nitrides

The refractive index $n_{op} = n_r + i n_i$ in semiconductors is mainly determined by the band edge transition. In the single electron picture, the real part n_r shows a sharp increase and a cusp-like feature at the bandgap energy. This is shown in Fig. 1.8(a) for the most relevant materials in this work: bulk GaN, $Al_{0.1}Ga_{0.9}N$, and $Al_{0.82}In_{0.18}N$ epilayers, and for a 1.5 nm thick GaN/$Al_{0.1}Ga_{0.9}N$ QW. A consequence of this feature, is that n_r decreases with increasing E_g of the material, for any given energy below E_g, as illustrated in Fig. 1.9 for the AlInN alloy [115, 116]. This leads to the interesting property that carrier or exciton confinement (which requires low E_g) will happen in the same materials as the optical mode confinement (which requires high n_r, see Chapter 2) in a waveguide or cavity. This leads to increased light-matter coupling in semiconductor cavities and waveguides, such as the structures used in this work. The optical confinement in a photonic structure is determined by the refractive index contrast RIC = $\frac{n_1^2 - n_2^2}{2n_1^2}$ between the materials with high (n_1) and low (n_2) refractive index [117]. In this work, we use $Al_{0.82}In_{0.18}N$ as low-index material. The RIC with GaN and $Al_{0.1}Ga_{0.9}N$ is also shown in Fig. 1.8(a) and reaches its maximum value of 15.5% near the bandgap energy of the high-index material. In the visible blue-green spectral region, the contrast amounts to about 4.5 - 6.5%.

The imaginary part of the refractive index n_i is closely related to the absorption coefficient α through the equation [75]

$$\alpha = \frac{4\pi n_i}{\lambda_0} = \frac{\omega \chi_i}{c n_r}, \tag{1.30}$$

where χ_i is the imaginary part of the linear optical susceptibility, defined by $\varepsilon_{rel} = 1 + \chi = 1 + \chi_r + i\chi_i$. The absorption coefficient above the bandgap can be calculated as [75]

$$\alpha(\omega) = \frac{\pi e^2 |\mathbf{r}_{cv}|^2 \omega n_r}{\varepsilon c} D_{cv}(\hbar\omega)[f_h(\hbar\omega) - f_e(\hbar\omega)], \tag{1.31}$$

where and $f_{e(h)}$ is the Fermi-Dirac distribution function of electrons (holes).

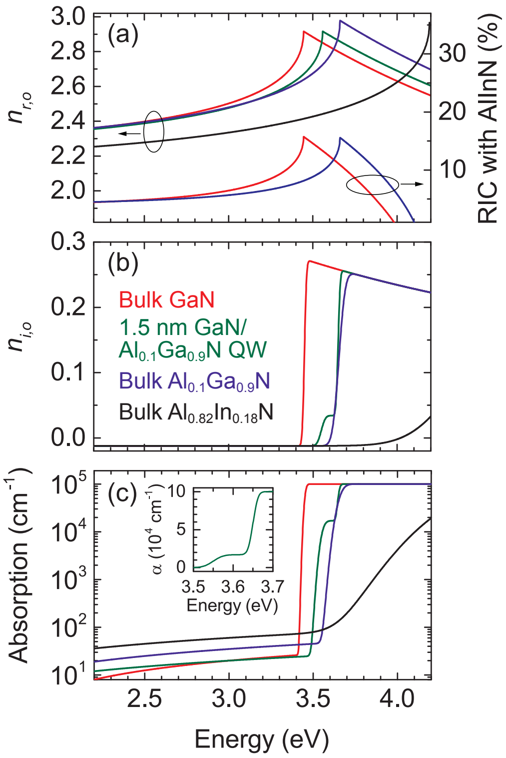

Figure 1.8 – Room temperature refractive index and optical absorption of bulk GaN (red), $Al_{0.1}Ga_{0.9}N$ (blue), and $Al_{0.82}In_{0.18}N$ (black) epilayers, and of a 1.5 nm thick GaN/$Al_{0.1}Ga_{0.9}N$ QW (green). (a) Real part of the ordinary refractive index and corresponding RIC of bulk GaN (red) and $Al_{0.1}Ga_{0.9}N$ (blue) with $Al_{0.82}In_{0.18}N$ epilayers. (b) Imaginary part of the ordinary refractive index. (c) Optical absorption coefficient. The residual absorption below the band edge is a result of defect and impurity states in the bandgap. It therefore highly depends on the defect and impurity concentration in the sample. The inset shows a detail of the QW absorption around E_{QW} and the barrier band edge. The dispersions are issued from experimental data taken from [82] for (Al)GaN and [29] for AlInN epilayers. The imaginary refractive index was determined from the reported absorption through Eq. 1.30.

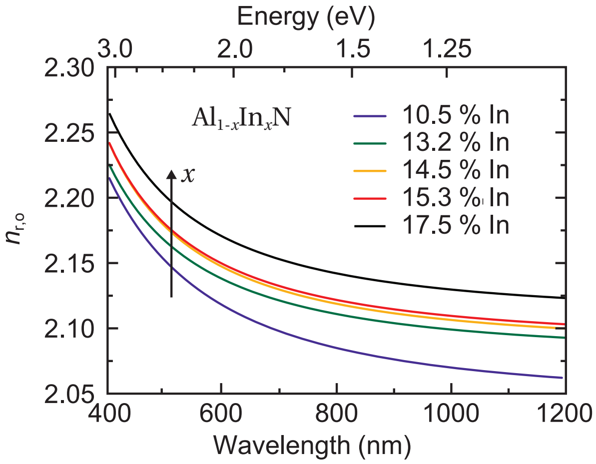

Figure 1.9 – Ordinary refractive index of bulk AlInN layers for different compositions. The refractive index increases for increasing In concentration. Adapted from [115].

Both n_i and α exhibit a step at E_g. In an ideal semiconductor, these quantities are zero below the bandgap, since no transitions between occupied and unoccupied states are available at these energies. In reality, however, defects introduce states in the gap, which results in nonzero sub-bandgap absorption and imaginary refractive index [118]. Free carriers also cause absorption, but this is typically occurring in the infrared spectral region [118]. Both quantities are depicted in Figs. 1.8(b) and 1.8(c), respectively. It is imperative for high-quality photonic devices to keep residual absorption as low as possible, as this is a major source of loss and decoherence. The absorption step at E_g is broadened by γ_{inh}, i.e. it is a Heaviside function convoluted with a Gaussian with full width at half maximum (FWHM) γ_{inh}. It is typically very sharp in high-quality GaN (< 1 meV) [91] and broader for ternary III-N alloys [82].

Due to the anisotropic structure of III-Ns, they will exhibit birefringence, i.e. propagating light experiences a different refractive index if it is polarized along or perpendicular to the optical axis c. Since the A subband only interacts with light polarized $\perp c$, the $E//c$ polarization can interact exclusively with the B and C subbands and therefore it experiences a larger effective bandgap. In this respect, the c-axis is called the extraordinary axis, while the a- and m-axes are called ordinary axes. Since we will focus on the transverse electric (TE) modes of c-plane waveguides in this work, which are polarized along the ordinary axes, we only represent the ordinary refractive index n_o in Fig. 1.8.

Quantum Well Structures

The refractive index of a QW can be approximated by shifting the index of the bulk material by the confinement energy $E^1_{e,conf} + E^1_{h,conf}$. The absorption in a QW resulting from a transition between a single valence subband and the conduction band is given by [75]

$$\alpha_{2D}(\lambda_0) = \frac{\pi e^2 E_P m_r}{3\lambda_0 n_r \varepsilon_0 E_g^2 d_{QW} m_0}, \tag{1.32}$$

where λ_0 is the vacuum wavelength and n_r is the real part of the refractive index of the QW material. In most practical cases, two or three transitions, i.e. A, B and optionally C, must be taken into account to find the total QW absorption [75]. For energies above the barrier bandgap, the bulk behavior is recovered, as shown in Fig. 1.8(c).

Effect of an Exciton Transition

The optical response of a homogeneously broadened (with FWHM γ_{hom}) bulk or quantum well exciton at energy E_X can be well described by the Drude-Lorentz damped harmonic oscillator model [77]:

$$\varepsilon_{rel}^{hom}(\hbar\omega) = \varepsilon_{bg} + \frac{f_X^{3D} e^2 \hbar^2}{\epsilon_0 M_X} \frac{1}{E_X^2 - (\hbar\omega)^2 + i\gamma_{hom}\hbar\omega}, \tag{1.33a}$$

$$\varepsilon_{rel}^{hom}(\hbar\omega) = \varepsilon_{bg} + \frac{f_X^{2D} e^2 \hbar^2}{d_{QW}\epsilon_0 M_X} \frac{1}{E_X^2 - (\hbar\omega)^2 + i\gamma_{hom}\hbar\omega}, \tag{1.33b}$$

for bulk and QW excitons, respectively, where ε_{bg} is the background permittivity of the semiconductor. In case of inhomogeneous broadening of the excitonic transition, which is typically the case for III-N QWs, the excitonic Lorentzian response has to be convoluted with a Gaussian function of standard deviation σ and FWHM $\gamma_{inh} = 2\sqrt{2\ln 2}\sigma$

$$\varepsilon_{rel}(\hbar\omega) = \frac{1}{\sigma\sqrt{2\pi}} \int_0^{+\infty} \exp\left(-\frac{(E' - \hbar\omega)^2}{2\sigma^2}\right) \varepsilon_{rel}^{hom}(E')\, dE'. \tag{1.34}$$

The oscillator strength determines the integrated intensity of the Lorentzian feature, as shown in Fig. 1.10(a). Inhomogeneous broadening of the excitonic transition dilutes the optical response over a larger spectral region. This results in a reduction in the feature amplitude, as shown in Fig. 1.10(b). Note that the effect of bulk excitons has been omitted in Fig. 1.8, since the feature is quite small at room temperature due to homogeneous broadening.

1.2.7 Effect of Carrier Density in Quantum Wells

Up to now, we have adopted a low carrier density picture. However, at elevated carrier densities N, several effects modify the QW properties. They will therefore be discussed in this section.

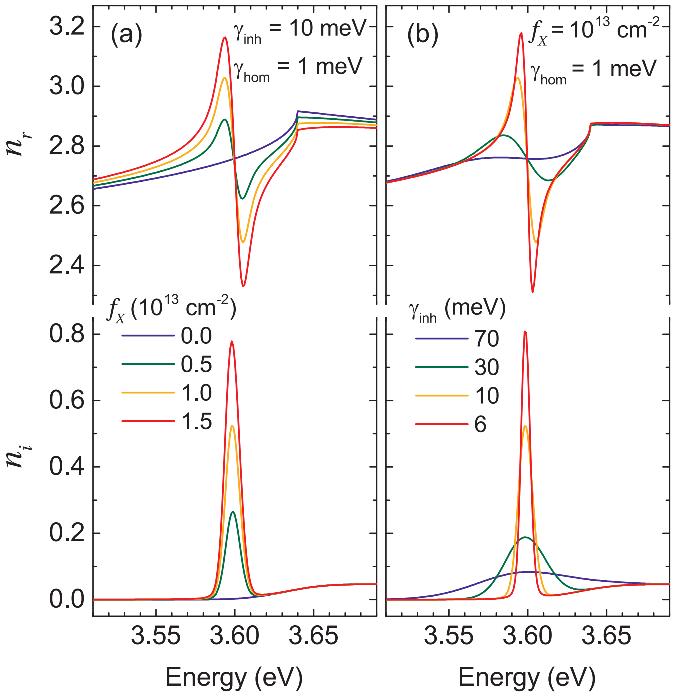

Figure 1.10 – Optical response of the ground state excitonic transition at low temperature (T = 12 K) in a 1.5 nm thick GaN/$Al_{0.1}Ga_{0.9}N$ QW. Real (top) and imaginary (bottom) part of the refractive index. (a) Effect of the oscillator strength f_X, which determines the amplitude of the Lorentzian response. (b) Effect of the inhomogeneous broadening γ_{inh}, which dilutes the excitonic response over a larger spectral range.

Screening of the Built-in Field

When the free carrier density in a QW approaches the polarization charge density σ^+ and σ^-, the built-in electric field is screened and the QCSE is reduced. As a consequence, E_g and E_X will blueshift until the flat-band regime is reached for which $F \approx 0$.

In order to calculate this blueshift, the Schrödinger equation (Eq. 1.3) should be solved simultaneously with Poisson's equation [97]:

$$\frac{\partial^2 \Phi(y)}{\partial y^2} = -\frac{\rho(y)}{\varepsilon}, \tag{1.35}$$

where Φ represents the electrostatic potential, ρ represents the charge density, and y is the position coordinate along the growth direction. Indeed, the band potential will determine the electron and hole envelope wavefunctions through the Schrödinger equation, while the charge distribution (given by the envelope wavefunctions) will screen F and modify the band potential through Poisson's equation. A consistent solution of both equations can be reached by iteratively solving one with the output of the other until convergence is reached: $F \xrightarrow{\text{Schrödinger}} \Psi_{e,h} \xrightarrow{\text{Poisson}} F \xrightarrow{\text{Schrödinger}} \Psi_{e,h} \xrightarrow{\text{Poisson}}$ ... In this work, we used a self-consistent Schrödinger-Poisson solver developed by J. Levrat and G. Rossbach at EPFL-LASPE [97, 119] that could accurately reproduce the behavior of high quality single GaN/AlGaN QWs upon increasing carrier density.

Bandgap Renormalization

With increasing carrier density, inter-particle interactions between excitons increase as well. Owing to the fermionic nature of the exciton constituents, both direct and exchange terms of the Coulomb-interaction have to be considered. This causes a monotonous redshift of the band edge E_g, the so-called bandgap renormalization (BGR), which follows a cubic root density dependence [120]

$$\Delta E_{BGR}(N) = 3.1 a_B^{2/3} E_B N^{1/3}. \tag{1.36}$$

Here, E_B is determined from $k \cdot p$ calculations [85] and a_B follows from Eq. 1.11.

From Bosonic Excitons to a Fermionic Electron-Hole Plasma

Since excitons are composed of two fermionic constituents, they have an integer total spin. This suggests that they should behave as bosons. Contrary to fermions, bosons do not obey the Pauli blocking principle. Within the framework of second quantization, the creation and annihilation operators of a boson of wave-vector $\mathbf{k}$, $b_{\mathbf{k}}^{\dagger}$ and $b_{\mathbf{k}}$, respectively, fulfill the commutation rule:

$$[b_{\mathbf{k}}, b_{\mathbf{k}'}^{\dagger}] = \delta_{\mathbf{k},\mathbf{k}'}, \tag{1.37}$$

where δ represents the Kronecker delta. It can be shown that Eq. 1.37 is never completely satisfied for excitons, but a good agreement is achieved in the low density regime [121]. When the density approaches the hard-sphere density, i.e. $N = \frac{1}{\pi a_B^2}$, the ideal bosonic behavior of Eq. 1.37 is gradually lost. This is a consequence of the increasing exchange interaction and phase space filling (Pauli blocking principle) of the fermionic constituents [121, 122].

Mott-transition

In the high-density regime, the (repulsive) inter-particle interactions between the fermionic constituents of the excitons, will cause a blueshift of the exciton energy, a reduction of E_B and eventually a dissociation of the excitons. This transition from an insulating exciton gas to a conducting e-h plasma is called the Mott transition, after the first prediction made by Sir Nevill Mott [123].

The Mott-transition in GaN/AlGaN QWs has been extensively studied by G. Rossbach *et al.* [124]. They showed that the Mott-transition is a secondary phase transition that occurs around $N \sim 10^{12}$ cm^{-2} with the fulfillment of two criteria. In the first criterion, E_g (which redshifts with N due to BGR) equals E_X (which blueshifts due repulsive inter-particle interactions). If these quantities are equal, the exciton binding energy (the difference between both) vanishes and the exciton gas dissociates. The second criterion is the Bernard-Duraffourg condition [125, 124]: the separation of electron and hole quasi-Fermi levels exceeds the bandgap and the stimulated emission rate exceeds the absorption rate. We therefore get optical gain (see Section 2.4). Since this is a purely fermionic effect, electrons and holes become the dominant species.

Oscillator Strength and Absorption Saturation

The exciton oscillator strength f_X will decrease with increasing carrier density due to phase space filling and to the Coulomb exchange interaction. When more excitonic states are occupied, less are available to absorb a photon, hence the light-matter interaction and the oscillator strength are reduced. The exchange interaction causes the exciton binding energy to decrease, as explained above, which results in an increased Bohr radius and a decreased interaction between electrons and holes. This also results in a decrease in the oscillator strength and the optical absorption.

In Ref. [126], Schmitt-Rink *et al.* assumed a linear relation between exciton density N_X and the oscillator strength variation

$$\Delta f_X = -\frac{N_X}{N_{sat}} f_X. \tag{1.38}$$

This is only valid for small saturation in the low-density regime. They found that the saturation exciton density N_{sat} is equal to

$$N_{sat} \approx \frac{0.117}{\pi a_B^2}, \tag{1.39}$$

where the contributions from phase space filling and exchange interaction are roughly equal [126]. It is important to notice that Eq. 1.39 is derived in the case where the saturating particle is the exciton and hence it neglects the contribution of free electrons and holes.

2 Light-Matter Interaction in Semiconductor Waveguides

This chapter, discusses the optical properties of III-N waveguides. We will start with a general discussion on the origin and the properties of guided modes in Section 2.1. Section 2.2 elucidates the properties of grating couplers. The chapter continues with an introduction on the light-matter interaction between waveguide modes and electronic excitations in semiconductors. Section 2.3 discusses the coupling with excitons, which leads to the formation of propagating exciton-polaritons. While Section 2.4 focuses on the coupling to an electron-hole plasma, which results in optical gain.

2.1 Guided Modes in Optical Waveguides

2.1.1 Total Internal Reflection at an Interface

In order to understand the origin and the dispersion of waveguide modes, we first discuss total internal reflection (TIR) occurring at an interface.

Let us consider a planar electromagnetic wave that is incident at an interface between two media with refractive index n_1 and n_2, respectively, with $n_1 > n_2$. In general, part of the incident light will be reflected and part of it will be transmitted. Here, we are interested in the case of internal reflection, i.e. the situation where light is incident from the high index side, as is sketched in Fig. 2.1. In phasor notation, the incident, transmitted and reflected fields will all contain a factor of the form $e^{-ik_z z}$, where z is the direction of propagation parallel to the interface, cf. Fig. 2.1. Since the Maxwell boundary conditions must be fulfilled for all values of z (i.e. at every point of the interface), the three waves must have the same in-plane wavevector component k_z. This is the case if the reflected wave has the same angle with the normal as the incident wave and the transmitted wave fulfills

$$k_1 \sin\theta_1 = k_2 \sin\theta_2 \tag{2.1a}$$

$$\Leftrightarrow n_1 \sin\theta_1 = n_2 \sin\theta_2. \tag{2.1b}$$

with $k_1 = \frac{2\pi n_1}{\lambda_0} = \frac{\omega n_1}{c}$ and $k_2 = \frac{2\pi n_2}{\lambda_0} = \frac{\omega n_2}{c}$ the wavenumbers in media 1 and 2, respectively. This is known as Snell's law. In the case of internal reflection, $\theta_2 > \theta_1$ since $n_1 > n_2$. This means that for a certain θ_1 value, called the critical angle θ_c, the magnitude of the wavevector component

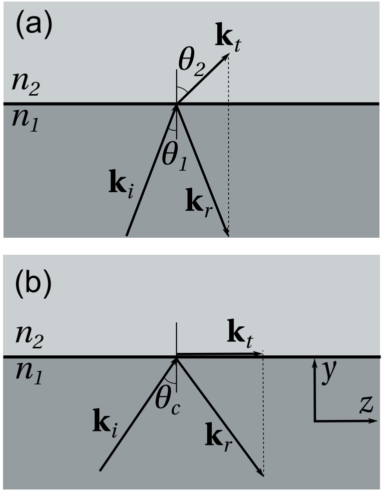

Figure 2.1 – Wavevectors of the incident, reflected and transmitted light ($\mathbf{k_i}$, $\mathbf{k_r}$ and $\mathbf{k_t}$, respectively) at an interface between two media. We take $n_1 > n_2$, which implies that the wavevectors in medium 1 are larger and therefore $\theta_2 > \theta_1$. (a) Case where $\theta_1 < \theta_c$. (b) Case where $\theta_1 = \theta_c$ and $\theta_2 = \frac{\pi}{2}$.

parallel to the interface of the incident and reflected waves will be equal to k_2. In this case, $\theta_2 = \frac{\pi}{2}$. This means that

$$\sin\theta_c = \frac{n_2}{n_1}.$$

If θ_1 increases even further, $\sin\theta_2$ must be larger than unity in order to fulfill Eq. 2.1b. This can only be the case if θ_2 becomes complex. The extended definitions of sine and cosine for complex arguments ($\theta_2 = \theta_{2,r} + i\theta_{2,i}$) are:

$$\sin(\theta_{2,r} + i\theta_{2,i}) = \sin\theta_{2,r}\cosh\theta_{2,i} + i\cos\theta_{2,r}\sinh\theta_{2,i}, \tag{2.2a}$$

$$\cos(\theta_{2,r} + i\theta_{2,i}) = \cos\theta_{2,r}\cosh\theta_{2,i} - i\sin\theta_{2,r}\sinh\theta_{2,i}. \tag{2.2b}$$

In order for $\sin\theta_2$ to be real and > 1, we see that $\theta_{2,r} = \frac{\pi}{2}$ and $\theta_{2,i} \neq 0$. This implies that $\cos\theta_2 = -i\sinh\theta_{2,i}$.

The reflection coefficients at an interface are given by the Fresnel equations [127]:

$$r_{TE} = |r_{TE}|e^{i\varphi_{TE}} = \frac{n_1\cos\theta_1 - n_2\cos\theta_2}{n_1\cos\theta_1 + n_2\cos\theta_2} = \frac{n_1\cos\theta_1 - n_2\sqrt{n_1^2/n_2^2(\sin^2\theta_c - \sin^2\theta_1)}}{n_1\cos\theta_1 + n_2\sqrt{n_1^2/n_2^2(\sin^2\theta_c - \sin^2\theta_1)}}, \tag{2.3a}$$

$$r_{TM} = |r_{TM}|e^{i\varphi_{TM}} = \frac{n_2\cos\theta_1 - n_1\cos\theta_2}{n_2\cos\theta_1 + n_1\cos\theta_2} = \frac{n_2\cos\theta_1 - n_1\sqrt{n_1^2/n_2^2(\sin^2\theta_c - \sin^2\theta_1)}}{n_2\cos\theta_1 + n_1\sqrt{n_1^2/n_2^2(\sin^2\theta_c - \sin^2\theta_1)}}. \tag{2.3b}$$

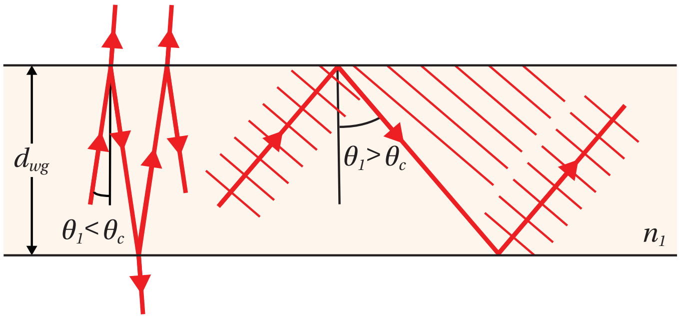

Figure 2.2 – Confinement and constructive interference condition in a waveguide. When the propagation angle θ_1 of a plane wave is below θ_c (left), the latter is only partially reflected at the interfaces and optical confinement is weak. If $\theta_1 > \theta_c$ (right), we have total internal reflection and the confinement is perfect for an ideal waveguide. Modes can only self-consistently exist in the waveguide if a plane wave constructively interferes with itself after two subsequent reflections. This means that the wavefronts of the two waves (represented by the thin lines in the right sketch) must coincide.

Here, TE means that the electric field is perpendicular to the yz plane, i.e. oriented along x, and transverse magnetic (TM) means that the magnetic field is oriented along x. Note that in case of a TM polarized wave, $r_{TM} = 0$ for $\theta_1 = \theta_B = \arctan\frac{n_2}{n_1}$. We call this angle the Brewster angle. If $\theta_1 > \theta_c$, the argument of the square root becomes negative and $\cos\theta_2$ becomes imaginary[1]

$$\theta_2 = -i\sqrt{n_1^2/n_2^2(\sin^2\theta_1 - \sin^2\theta_c)}. \tag{2.4}$$

Consequently, the expressions in the numerator and denominator of Eqs. 2.3 are complex conjugates and r is a complex number with unity square modulus and nonzero argument. This means that light will be fully reflected at the interface, with a phase shift given by

$$\tan\frac{\varphi_{TE}}{2} = \sqrt{\frac{\cos^2\theta_c}{\cos^2\theta_1} - 1} = \frac{\beta^2 - k_2^2}{k_1^2 - \beta^2}, \tag{2.5a}$$

$$\tan\frac{\varphi_{TM}}{2} = \frac{n_1^2}{n_2^2}\sqrt{\frac{\cos^2\theta_c}{\cos^2\theta_1} - 1} = \frac{n_1^2}{n_2^2}\frac{\beta^2 - k_2^2}{k_1^2 - \beta^2}, \tag{2.5b}$$

where $\beta = k_z$ represents the wavevector component in the plane of the interface. For this reason, we call the situation where the incident angle $\theta_1 > \theta_c$ TIR.

---

[1] The dependence of the transmitted electric and magnetic fields in the y direction is given by $e^{-ik_{2,y}y} = e^{-ik_2\cos\theta_2 y}$. Since the magnitude of these fields cannot reach ∞ for $y \to +\infty$, $\cos\theta_2$ must be in the lower complex half plane and we get exponentially decaying fields in the $+y$-direction.

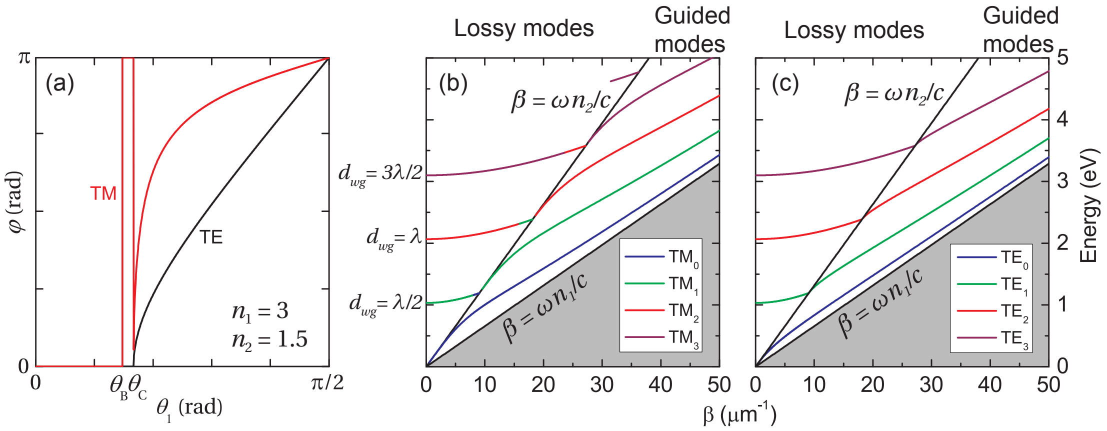

Figure 2.3 – (a) Phase shift φ of a TE and TM polarized plane wave after reflection at an interface between two media with refractive index n_1 and n_2, respectively. For low angles, $r = |r|e^{i\varphi}$ is real and positive, while for $\theta_1 > \theta_c$, r is complex with an increasing argument. In the TM case, r is real and negative between θ_B and θ_c. (b) and (c) Mode dispersion of a 2D slab in the lossy ($\beta \leq \omega n_2/c$) and guided regime ($\beta > \omega n_2/c$) for (b) TM and (c) TE polarizations. Due to the increased phase shift between the Brewster and critical angle for the TM case, the energy of mode m is shifted to the energy of mode $m+1$.

2.1.2 Waveguide Modes

If we put a 2D slab of a high-index (n_1) material with thickness d_{wg} between two low-index (n_2) cladding layers (this structure is commonly called a 2D optical waveguide), a plane wave propagating with an angle $\theta_1 > \theta_c$, will undergo TIR at both interfaces of the waveguide and will be perfectly confined. In the case where $\theta_1 < \theta_c$, there is only partial reflection and the confinement is lossy. These two regimes are sketched in Fig. 2.2. Another way of differentiating the two regimes, is via the in-plane wavevector component k_z. In the context of waveguides, this wavevector component is usually called the propagation constant $\beta = \frac{\omega n_1}{c}\sin\theta_1$ of the guided mode. Total internal reflection arises when $\beta > k_2 = \frac{\omega n_2}{c}$, as explained above, whereas partial reflection arises when $\beta \leq k_2$. In the former case, we say that β is outside the cladding light cone described by $k_2 = \frac{\omega n_2}{c}$ and we call this the waveguide regime. In the latter case, β is inside the cladding light cone and this is called the Fabry-Perot regime. A microcavity is a Fabry-Perot cavity, where the limited interface reflectivity is enhanced by adding a multilayer DBR on both sides. A DBR consists of a stack of alternating high- and low-index quarter-wavelength layers. The waves reflected off the different interfaces constructively interfere and the reflectivity is enhanced.

In order for a lightwave to self-consistently exist in the waveguide, it must constructively interfere with itself after two consecutive reflections, as illustrated in Fig. 2.2. This will be the case if

$$n_1\frac{\omega}{c}2d_{wg}\cos\theta_m - 2\varphi = 2\pi m, \tag{2.6}$$

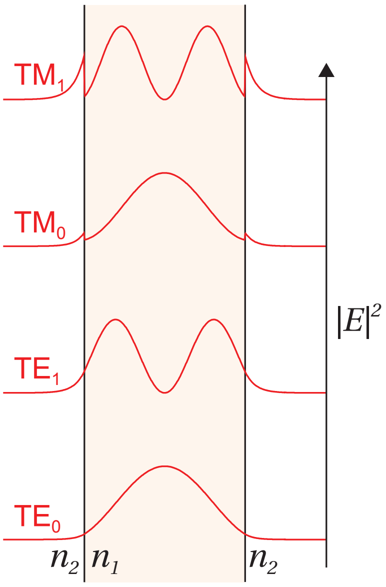

Figure 2.4 – Electric-field intensity profile of the four most fundamental waveguide modes. The mode order m represents the number of nodes in the profile. The TM modes have a discontinuity in the electric field at the interface, since their E-field has a component perpendicular to the interface and for this orientation, $D = \varepsilon E$ is continuous across the interface. The TE modes have their E-field tangential to the interface, and therefore there is no discontinuity.

with $m \in \mathbb{N}$. This limits the possible values of β for every wavelength. Consequently, we get discrete eigenmodes that can exist in the waveguide. m is called the order of the mode. The dispersion of these modes is shown in Fig. 2.3. The dispersion in the Fabry-Perot regime is approximately parabolic, while it is approximately linear in the waveguide regime. Due to the $\varphi = \pi$ phase shift between θ_B and θ_C in the TM case, the energy of the modes discontinuously shifts to higher energy for constant m.

We see that for any given energy and waveguide thickness d_{wg}, only a limited number of guided modes can exist. When we reduce d_{wg} or increase the wavelength, the number of modes is reduced and higher-order modes are cut off. If the waveguide is not symmetric, i.e. the top and bottom claddings have a different refractive index, the term 2φ in Eq. 2.6 has to be replaced by the sum of the two appropriate phase shifts as calculated by Eq. 2.5. Additionally, guided modes will only exist if β lies outside both cladding's light cones in this case.

If Eq. 2.6 is fulfilled, the upward and downward propagating plane waves that are sketched in Fig. 2.2, form a consistent standing wave pattern. This standing wave propagates in the structure with wave number $\beta = \frac{\omega n_{eff}}{c}$, where we have defined the effective refractive index $n_{eff} = n_1 \sin\theta_1$. The standing wave in the waveguide is completed by an evanescent wave in the cladding, as shown in Fig. 2.4 for the TE$_m$ and TM$_m$ modes with $m = 0,1$. The intensity profile of the optical mode will be an important feature to consider when discussing light-matter interaction, as the coupling will be proportional to the local field strength. This means, e.g., that an exciton in a QW located at a node of the modal field will not couple to the optical mode. The mode order m also represents the number of nodes in the standing wave.

An important parameter that is deduced from the mode profile, is the modal volume V, or in 1D, the modal effective length L_{eff}. In this work, we use the following definition of the effective length of the waveguide mode [128]:

$$L_{eff} = V_{1D} = \frac{\int \varepsilon |E|^2 dy}{\max(\varepsilon |E|^2)}. \tag{2.7}$$

The denominator assures the correct normalization of the peak modal field to unity. L_{eff} defines the region to which a photon is confined. A small effective length leads to a large electric field strength according to Eq. 1.21 and consequently, a large light-matter interaction.

Note that for microcavities, the effective modal length is usually defined as [129]

$$L_{eff}^{MC} = 2\frac{\int \varepsilon |E|^2 dy}{\max(\varepsilon |E|^2)}. \tag{2.8}$$

The rationale behind this definition is that it represents the cavity length required to have an equal one-dimensional mode volume if there were no evanescent fields in the distributed Bragg reflectors. Since a microcavity has a sinusoidal mode profile (as detailed below) with an average value of the modal field intensity over the standing wave equal to $\frac{1}{2}$, we get that

$$L_{eff}^{MC} = 2L_{eff}, \tag{2.9}$$

which corresponds exactly to Eq. 2.8.

2.2 Theory of Grating Couplers

Since waveguide modes are outside the air light cone, they cannot couple to free-space radiant modes. If we want to study their modal dispersion, we either have to collect the light from the end of the waveguide (end-fire coupling), or we have to use a grating coupler. In this work, we use the latter option, because it allows a direct mapping of the guided mode wavevector, following Eq. 2.11, derived below. Additionally, light collection in the sample plane, as required for end-fire coupling, is challenging with our cold-finger cryostat. The setup is described in Section 4.2.

In order to understand the working principle of a grating coupler, we first consider scattering of a light wave by a periodic structure. Consider a planar light wave with wavevector $\mathbf{k}_i$ that is incident on a periodic ensemble of line scatterers with period Λ, as depicted in Fig. 2.5. Diffraction of the incoming light will only happen if the contributions from different line scatterers

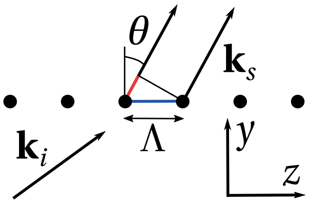

Figure 2.5 – Diffraction from a periodic ensemble of line scatterers. Constructive interference occurs for those directions where the blue and red pathways have a phase difference which is an integer multiple of 2π.

interfere constructively. This will be the case for those directions (defined by the angle θ made with the normal to the grating plane) where the red and blue pathways have a phase difference equal to an integer multiple of 2π. Along the blue pathway, the incident wave experiences a phase shift of $k_{i,z}\Lambda$, before reaching the second scatterer. Meanwhile, the scattered wave $\mathbf{k}_s$ has experienced a phase shift of $k_s\Lambda\sin\theta$. Therefore, we get constructive interference if

$$k_{i,z}\Lambda - k_s\Lambda\sin\theta = 2\pi q \tag{2.10a}$$

$$\Leftrightarrow k_{i,z} - \frac{2\pi q}{\Lambda} = k_s\sin\theta, \tag{2.10b}$$

with $q \in \mathbb{Z}$ the diffraction order. In this work, we use first-order gratings to maximize the outcoupled light intensity and to avoid back-reflection into the waveguide. If we apply Eq. 2.10b to the case of a grating coupler on a waveguide (which is in its basic form nothing more than a set of periodic line scatterers), where the incident wave is a guided mode with $k_{i,z} = \beta$, and $k_s\sin\theta$ is the z-component of the outcoupled wave in air, $k_{z,air}$, we get the following relation between the guided mode wavevector and the emission angle from the grating coupler,

$$k_{z,air} = \frac{\omega}{c}\sin\theta = \beta - \frac{2\pi q}{\Lambda}. \tag{2.11}$$

This simple relation allows us to determine the guided mode in-plane wavevector component β from the emission angle and the mode dispersion. We can choose the grating period such that the in-plane wavevector region of interest is emitted close to the normal to the sample surface and within the numerical aperture of the collection optics.

2.3 Waveguide Exciton-Polaritons

2.3.1 Exciton-Photon Coupling

An electronic excitation, such as an exciton, that is coupled to the vacuum field will decay according to Fermi's golden rule (Eq. 1.26), as explained in Section 1.2.4. We remind that Eq. 1.26 contains a factor E_0^2, the electrical field intensity at the location of the excitation, corresponding to a single photon in the optical mode to which the excitation is coupled. The transition rate can therefore be enhanced or reduced by varying E_0, e.g. by moving the excitation to an antinode or a node of the optical field, or by decreasing or increasing the optical mode volume V (cf. Eq. 1.21). Here we will consider excitons as electronic excitations (Section 2.4 will discuss the case of unbound electron-hole pairs) and we will focus on the case of enhanced interaction.

If the loss rate is higher than the reabsorption rate of an emitted photon, the photon will escape from the waveguide before reabsorption by the emitter occurs. This regime is called the weak coupling regime (WCR). If we can enhance the light-matter interaction in such a way that the reabsorption rate becomes higher than the loss rate, an emitted photon will be reabsorbed before it can escape from the waveguide. In this SCR, the present energy packet will oscillate back and forth between a photonic and an excitonic state. We call such a hybrid quasi-particle an exciton-polariton, or polariton for short. These polaritons have very interesting properties that are intermediate between those of photons and excitons, such as light-like propagation and inter-particle interactions coming from their excitonic part.

The coupling between excitonic and optical modes can be understood by making the analogy with two coupled mechanical oscillators, as sketched in Fig. 2.6. We consider two pendula (where one represents the photonic mode and the second the excitonic mode) of equal length, mass m_p and angular resonance frequency ω, which are coupled by a spring of stiffness k and coupling constant $g = \sqrt{\frac{k}{m_p}}$. If the damping rates γ_1, γ_2 of pendula 1 and 2, respectively, are much higher than g, a displacement given to one of the pendula will die out before it can be transmitted to the other one and the system is in the WCR. If on the other hand, γ_1,$\gamma_2 \ll g$, the system is in the SCR and mechanical energy will be exchanged between the two pendula, as illustrated in Fig. 2.6. The movement of the pendula follows a beating pattern, which can be described by the sum of two frequencies: ω_{ac} and ω_{opt}. ω_{ac} corresponds to the eigenfrequency of the acoustic eigenmode of the coupled system, where both pendula move in phase, and $\omega_{opt} > \omega_{ac}$ corresponds to the eigenfrequency of the optical eigenmode, where both pendula move with opposite phases. The generation of new hybrid eigenmodes, with a splitting in their eigenenergies, is a defining characteristic of the SCR.

2.3.2 Coupled Quantum Oscillator Model

In analogy to the coupled mechanical oscillators, the light-matter interaction can be described by two coupled quantum oscillators with exciton-photon coupling strength g_0. For a confined optical mode with effective length L_{eff} and refractive index n_{eff} coupled to QW excitons, it

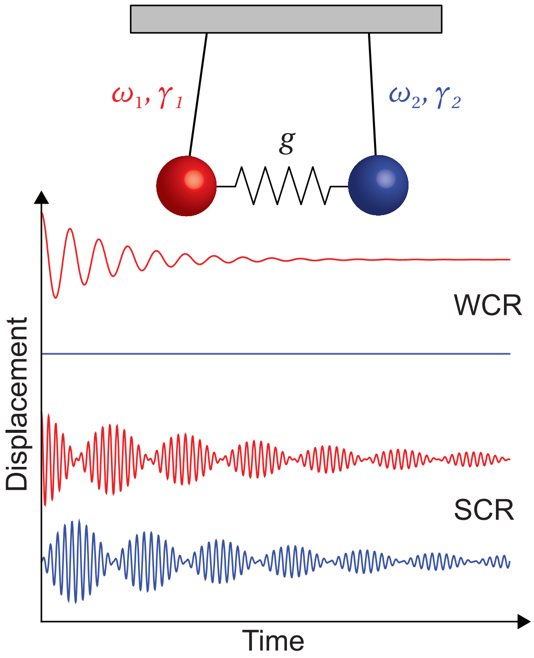

Figure 2.6 – Coupled mechanical oscillators in the strong (SCR) and weak coupling regime (WCR). (top) Sketch of two harmonic oscillators with uncoupled eigenfrequencies ω_1 and ω_2 and damping rates γ_1 and γ_2, respectively, joined by a spring of coupling constant g. (bottom) Oscillatory movement as a function of time. In the SCR ($g \gg \gamma_1, \gamma_2$), energy is transferred back and forth between the oscillators many times before the energy is dissipated. In the WCR ($g \ll \gamma_1, \gamma_2$), energy is dissipated before it can be transferred

can be expressed (in units of energy) as [128, 129]

$$g_0 = \frac{\hbar}{2} \sqrt{\frac{e^2 N_{QW}^{eff} f_X}{m_0 \varepsilon_0 n_{eff}^2 L_{eff}}}, \tag{2.12}$$

where N_{QW}^{eff} is the effective number of QWs that are coupled to the optical mode, i.e. the nominal number of QWs weighted by the intensity of the modal field:

$$N_{eff}^{QW} = \frac{\sum_{y_i} \varepsilon(y_i) |E(y_i)|^2}{\max(\varepsilon |E|^2)}, \tag{2.13}$$

with i the QW number and y_i the respective QW positions.

From Eq. 2.12, we can see which parameters influence the exciton-photon coupling. A large oscillator strength, which is typically present in wide-bandgap semiconductors such as GaN and ZnO, favors a large g_0 value. Additionally, structures with a large N_{QW}^{eff}, combined with a small L_{eff}, in other words a good overlap between the QWs and the optical mode, have an intense light-matter interaction. For the latter criterion, waveguides have a significant advantage over microcavities, since in the latter the optical mode extends far into the DBRs surrounding the cavity, leading to a large L_{eff} value with a relatively small N_{QW}^{eff}, whereas it quickly decays in the waveguide claddings. This point is more extensively discussed and illustrated in Section 2.3.4.

In the framework of second quantization, an exciton and a photon of in-plane wavevector β are characterized by their respective creation ($\hat{d}^{\dagger}_{\beta}$ and $\hat{c}^{\dagger}_{\beta}$) and annihilation operators ($\hat{d}_{\beta}$ and $\hat{c}_{\beta}$). In the coupled quantum oscillator model, the coupled photonic (with energy $E_{ph}(\beta)$ and decay rate γ_{ph}) and excitonic ($E_X(\beta)$, γ_X) states are described by the Hamiltonian

$$\hat{H} = (E_X(\beta) + i\gamma_X)\hat{d}^{\dagger}_{\beta}\hat{d}_{\beta} + (E_{ph}(\beta) + i\gamma_{ph})\hat{c}^{\dagger}_{\beta}\hat{c}_{\beta} + g_0\left[\hat{d}^{\dagger}_{\beta}\hat{c}_{\beta} + \hat{c}^{\dagger}_{\beta}\hat{d}_{\beta}\right], \tag{2.14}$$

or in matrix form

$$\widehat{H} = \begin{bmatrix} E_X + i\gamma_X & g_0 \\ g_0 & E_{ph} + i\gamma_{ph} \end{bmatrix}. \tag{2.15}$$

The eigenstates of the system are the upper (UP) and lower polaritons (LP) and can be found by diagonalizing this Hamiltonian using the unitary transformation

$$\hat{p}_{LP,\beta} = X(\beta)\hat{d}_{\beta} + P(\beta)\hat{c}_{\beta}, \tag{2.16a}$$
$$\hat{p}_{UP,\beta} = -P(\beta)\hat{d}_{\beta} + X(\beta)\hat{c}_{\beta}. \tag{2.16b}$$

X and P are called the Hopfield coefficients [96], which satisfy $|X|^2 + |P|^2 = 1$. The diagonalized Hamiltonian reads

$$\hat{H} = E_{LP}(\beta)\hat{p}^{\dagger}_{LP,\beta}\hat{p}_{LP,\beta} + E_{UP}(\beta)\hat{p}^{\dagger}_{UP,\beta}\hat{p}_{UP,\beta}. \tag{2.17}$$

The operators $\hat{p}^{\dagger}_{LP,\beta}$, $\hat{p}_{LP,\beta}$ and $\hat{p}^{\dagger}_{UP,\beta}$, $\hat{p}_{UP,\beta}$ are creation and annihilation operators of the LP and UP, respectively. The eigenenergies of these hybrid states are

$$E_{UP}(\beta) = \frac{1}{2}\left[E_X + E_{ph} + i(\gamma_X + \gamma_{ph}) + \sqrt{4g_0^2 - (\gamma_X - \gamma_{ph})^2 + (E_X - E_{ph})^2}\right], \tag{2.18a}$$
$$E_{LP}(\beta) = \frac{1}{2}\left[E_X + E_{ph} + i(\gamma_X + \gamma_{ph}) - \sqrt{4g_0^2 - (\gamma_X - \gamma_{ph})^2 + (E_X - E_{ph})^2}\right]. \tag{2.18b}$$

The upper (UPB) and lower polariton branch (LPB) exhibit an anticrossing, as shown in Fig.

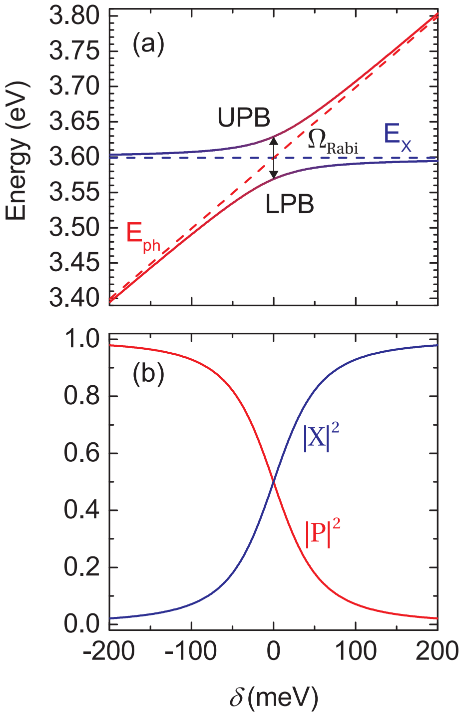

Figure 2.7 – Two quantum oscillators with a coupling strength of $g_0 = 30$ meV. (a) The polariton branches anticross near zero detuning. The upper and lower polariton branches gradually change from exciton-like and photon-like, respectively, at strongly negative detuning to the inverse situation at strongly positive detuning. (b) The photon and exciton fraction of the LPB are determined by the square modulus of the Hopfield coefficients, $|P|^2$ and $|X|^2$, respectively.

2.7(a), which is a characteristic feature of the SCR. The normal mode splitting or Rabi splitting Ω_{Rabi} is defined as the minimal distance between the two branches, which occurs at zero detuning ($\delta = E_{ph} - E_X = 0$). By subtracting E_{LP} from E_{UP}, we obtain

$$\Omega_{Rabi} = \sqrt{4g_0^2 - (\gamma_X - \gamma_{ph})^2}. \tag{2.19}$$

The Hopfield coefficients are given by

$$X(\beta) = \frac{1}{\sqrt{1 + \left(\frac{E_{LP}(\beta) - E_X}{g_0}\right)^2}}, \tag{2.20a}$$

$$P(\beta) = \frac{1}{\sqrt{1 + \left(\frac{g_0}{E_{LP}(\beta) - E_X}\right)^2}}. \tag{2.20b}$$

$|X|^2$ and $|P|^2$ represent the excitonic and photonic fraction of the lower polaritons, respectively, and are shown in Fig. 2.7(b). This implies that one can vary the light and matter content of polaritons by changing the detuning between the exciton and photon mode. As such, many polariton properties, such as lifetime, propagation and polariton-polariton interactions can be tuned as well.

This coupled oscillator model (COM) represents a simplified picture, and neglects the dispersion of the refractive index, inhomogeneous linewidth broadening and the influence of the electron-hole continuum absorption. In order to circumvent these limitations, a linear dispersion model is often used, which is based on the optical response of excitons.

2.3.3 Linear Dispersion Model

The intrinsic properties of strongly coupled systems, such as the normal mode splitting or the energy dispersion, can be well described in the linear regime without the need for a quantum picture. Nonlinear phenomena however, such as Bose-Einstein condensation [130] or polariton lasing [17], can only be described by a quantum model. Zhu and coworkers successfully explained the splitting of a resonant cavity coupled to an ensemble of barium atoms considered as Lorentz oscillators, by using a linear dispersion model [131]. The same is valid for semiconductor excitons coupled to a waveguide or cavity mode. Their optical response can be described by the Drude-Lorentz model explained in Section 1.2.6. The effect of this Lorentzian feature on the coupled system is an increase of n_{eff} at energies just below E_X and a decrease of n_{eff} just above E_X. An increased refractive index will cause an increase in optical distances (the product of distance and refractive index) and consequently, a shift towards longer wavelengths or smaller energies of the modes. Conversely, a decreased refractive index causes a blueshift of the modes. As a result, the optical mode is shifted away from E_X on both the high and low energy side of the exciton resonance, leading to the characteristic anticrossing behavior.

The advantage of this approach is that effects such as dispersion of the refractive index, field distribution in the waveguide, inhomogeneous linewidth broadening and absorption in the materials are intrinsically considered. The final step is to find the resonant modes in the system using an optical solving technique, such as transfer matrix simulations (TMS) [132], the finite element method or the finite-difference time-domain (FDTD) method. In this work, we mainly use an FDTD solver, which is elaborately explained in Appendix A. A TMS solver developed by J. Levrat, G. Rossbach and M. Glauser at EPFL-LASPE was occasionally used for modeling planar microcavities [97, 119, 133], which were considered for the sake of comparison

This linear dispersion model allows to directly compare the impact of γ_{inh} and γ_{hom} on the coupling regime of the system. It was shown by Houdré and coworkers that inhomogeneous broadening of the excitonic mode has no effect on the Rabi splitting of the system [134]. This is true as long as $\gamma_{inh} < g_0$ [97]. For larger inhomogeneous broadening, the splitting is reduced and the SCR is gradually lost [110]. For homogeneous broadening on the other hand, small values of γ_{hom} already reduce the splitting [97].

2.3.4 Microcavity and Waveguide Polaritons

The SCR was first observed in a sodium Rydberg atom cavity at room temperature in 1983 [135]. Almost a decade after this first demonstration, in 1992, Weisbuch and coworkers demonstrated the same phenomenon in a GaAs-based semiconductor planar microcavity at 4 K [136]. In the following decades a lot of research was conducted on these structures, where an optical cavity mode (Fabry-Perot mode confined by two DBRs) is strongly coupled to bulk or QW excitons. As an illustration, an $Al_{0.1}Ga_{0.9}N$ cavity with a 35 pair $Al_{0.83}In_{0.17}N/Al_{0.1}Ga_{0.9}N$ bottom DBR and an 8 pair SiO_2/Si_3N_4 top DBR is shown in Fig. 2.8(a), together with its optical mode. Due to the relatively weak spatial confinement of a typical DBR (which depends mainly on the RIC between the high- and low-index material), the optical mode extends quite far into the DBR region, resulting in a large $L_{eff} = 330$ nm. For comparison, a III-N waveguide consisting of the same materials is shown in Fig. 2.8(b). Here, the TIR confinement ensures a rapid decay of the optical mode in the cladding layers, leading to a small $L_{eff} = 88$ nm and a good overlap between the optical mode and the active region. Besides spatial confinement, the temporal confinement is also improved, i.e. the photon leakage is reduced in a waveguide with respect to a microcavity. The photon lifetime $\tau_{ph} = \frac{\hbar}{\gamma_{ph}}$ (with γ_{ph} expressed as an energy) in a microcavity is determined by the reflectivity $R = |r|^2$ of the mirrors. For a DBR, the peak reflectivity increases with the RIC between the high and low index material and the number of pairs. Typically, a DBR can reach 95 - 99.9% peak reflectivity, depending on the wavelength and the chosen material system. TIR, on the other hand, is in theory lossless. In a waveguide, τ_{ph} is limited by interface roughness scattering and absorption in the waveguide. A quantity that is widely used to describe the optical temporal confinement is the quality factor

$$Q = \omega_{ph}\tau_{ph} = \frac{E_{ph}}{\gamma_{ph}}. \tag{2.21}$$

It represents the number of oscillations the optical field makes within the photon lifetime.

One of the main reasons for the high scientific interest in microcavity polaritons is their very low effective mass, which is of the order of $10^{-4} m_0$. Indeed, looking at the energy dispersion of the microcavity described above, operating in the SCR (as shown in Fig. 2.8(c)), we find that the LPB has a curvature similar to the photonic mode near $\beta = 0$. Note that the exciton is nearly dispersionless at this scale due to its much larger mass. As a consequence of this very low mass and the bosonic nature of polaritons, Bose-Einstein condensation has been demonstrated at liquid He temperatures [130] in a CdTe-based microcavity, compared to the ~ 100 nK temperatures required to form such a condensate with much heavier cold atoms [137]. Polariton lasing, a phenomenon that is similar to Bose-Einstein condensation, but where the polaritons lack a thermal energy distribution, has even been demonstrated at room temperature in a III-N microcavity, both using a bulk active region [17], and a GaN/AlGaN MQW active region [18]. This condensation leads to interesting phenomena going from coherent light emission

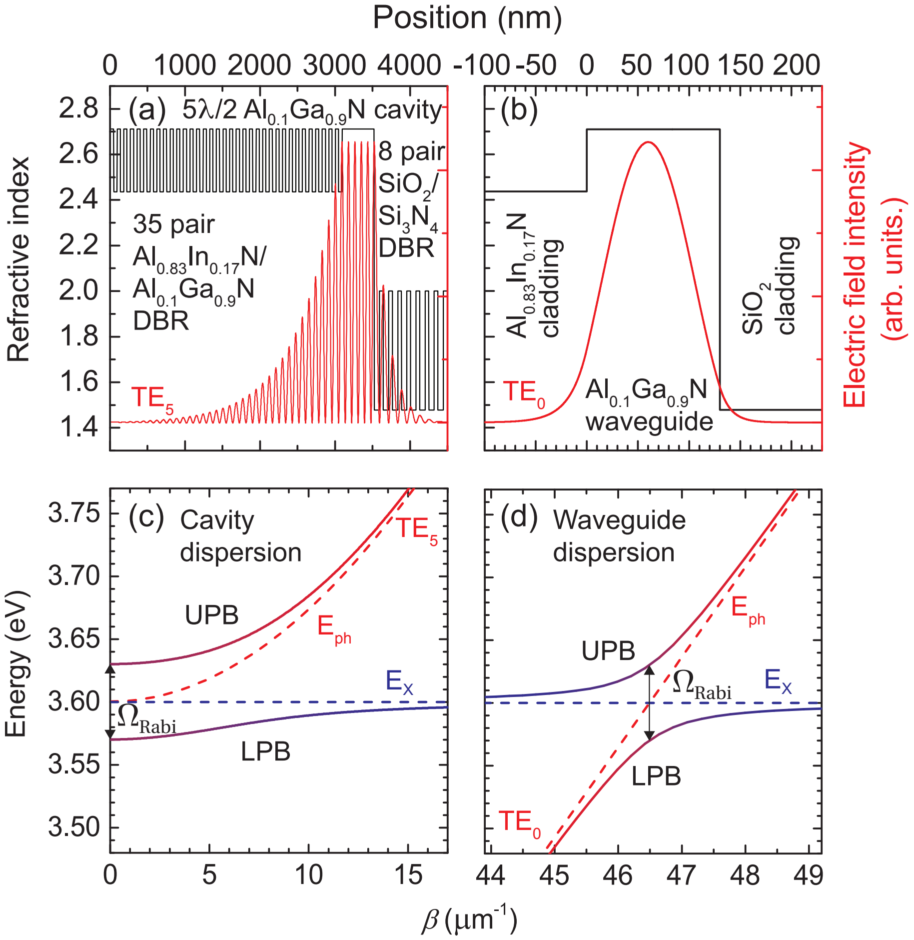

Figure 2.8 – Modal field profile and energy dispersion of a III-N microcavity and waveguide, tailored for an exciton energy of 3.6 eV. (a) Modal field intensity (red line) and refractive index profile (black line) of a $5\lambda/2$ $Al_{0.1}Ga_{0.9}N$ cavity with a 35 pair $Al_{0.83}In_{0.17}N/Al_{0.1}Ga_{0.9}N$ bottom DBR and an 8 pair SiO_2/Si_3N_4 top DBR. The optical mode extends substantially into the DBRs, especially the bottom one. (b) Modal field intensity (red line) and refractive index profile (black line) of a 130 nm $Al_{0.1}Ga_{0.9}N$ waveguide with an $Al_{0.83}In_{0.17}N$ bottom cladding and SiO_2 top cladding. The mode is well confined within the core layer. (c) Energy dispersion of the cavity shown in (a) containing QWs with an exciton energy (E_X, blue dashed line) of 3.6 eV. The UPB and LPB are shown for a coupling strength $g_0 = 30$ meV, as calculated with the COM. Note that in the case of 0 detuning at $\beta = 0$ shown here, δ is nowhere negative and the photon fraction of the LPB does not increase above 0.5. Near $\beta = 0$, the LPB has a similar curvature as the parabolic optical mode (E_{ph}, red dashed line), and therefore a similar effective mass of $1\times10^{-4}\,m_0$, compared to $5\times10^{-5}\,m_0$ for the optical mode. (d) Energy dispersion of the waveguide shown in (b) containing QWs with $E_X = 3.6$ eV. Here, the UPB and LPB are also calculated with the COM for $g_0 = 30$ meV. In a waveguide in the strong coupling regime, the LPB is characterized by a negative effective mass. The refractive index data are taken from [82] for (Al)GaN and [29] for AlInN. The dispersions in (c) and (d) were calculated using constant refractive index values, as shown in (a) and (b), respectively. The optical mode profile is calculated using TMS in (a) and FDTD calculations in (b).

without population inversion, which was originally proposed by Imamoglu *et al.* [138], over superfluidity [139] to quantized vortices [140]. Besides this rich and interesting physics, polariton microcavities have shown potential for several applications such as parametric amplifiers [141], spin switches [15] and all-optical active devices including all-optical transistors [142] and Mach-Zehnder interferometers [143].

Waveguides operating in the SCR have only recently gained attention from the scientific community using various material systems such as GaAs [144, 145], organic semiconductors [146, 147, 148] and wide-bandgap inorganic semiconductors [149, 150]. The energy dispersion of a waveguide LPB, as shown in Fig. 2.8(d) has a negative effective mass, and no ground state near the anticrossing point. As a result, condensation is not possible in these structures. However, another nonlinear effect has been demonstrated in polariton waveguides in the form of low-power optical solitons. Walker and collaborators have experimentally realized dark-bright spatio-temporal polariton soliton wavepackets with energies as low as 0.5 pJ in GaAs-based structures operating at 10 K [16].

Another key difference between waveguides and microcavities originates from the in-plane wavevector and group velocity of the polaritons. In a microcavity, anticrossing occurs around $\beta = 0$, whereas it occurs for much higher values (46.5 $\mu\mathrm{m}^{-1}$ for the waveguide shown in Fig. 2.8(d)) in a waveguide, resulting in high group velocities of the order of 10^7 m/s. This propagating nature of waveguide polaritons makes them well suited for polaritonic integrated circuits, compared to the more stationary microcavity polaritons.

From a structural point of view, waveguides are much simpler to grow than microcavities. The DBR layer thicknesses and cavity thickness must closely match the exciton energy in order to have a small detuning between the cavity and exciton mode near zero in-plane wavevector. For a waveguide on the other hand, the optical properties do not depend on the cladding thickness and only weakly on the core dimensions. Additionally, since the energy dispersion of the uncoupled waveguide mode is monotonically increasing with β, it will always cross the uncoupled excitonic mode, regardless of the exact waveguide structure, as long as the guided mode is not cut-off, leading to hybridization of the light and matter modes. Additionally, the waveguide geometry can allow for easy potential landscaping by electrical gating [145] and electrical injection of carriers –as is commonly done in edge-emitting LDs– as opposed to electrical injection through DBRs, which is a much more challenging task.

In the case of GaN/AlGaN QW-based microcavities and waveguides, the latter have the additional advantage that the bottom cladding can be lattice-matched to GaN. Since only a low-index material is required, lattice-matched AlInN can be used for this cladding.[2] In case of microcavities however, UV AlGaN/AlInN DBRs with a substantial amount of Al have to be used to avoid absorption. This induces a significant amount of lattice-mismatch with respect to the GaN buffer and requires the application of strain-management techniques [47].

---

[2] For reasons of material quality, which are explained in Section 1.1.3, GaN interlayers are required in thick AlInN films. These are of course also lattice-matched to the rest of the structure.

2.4 Optical Gain from an Electron-Hole Plasma

When an optical field of angular frequency ω interacts with a two-level electronic system, consisting of a ground state and an excited state, separated by an energy $\hbar\omega$, three possible processes can occur [75, 151]:

- Absorption
  A photon is absorbed from the optical field and the electron is promoted from the ground state to the excited state.

- Spontaneous emission
  The electron decays from the excited state to the ground state, due to a perturbation induced by the vacuum field. The emitted photon has a random phase, polarization and propagation direction.

- Stimulated emission
  The electron decays from the excited state to the ground state, due to a perturbation induced by the optical field. The emitted photon is coherent with the latter.

An optical signal that is propagating through an active region where these three processes can occur, will be attenuated by absorption α and amplified by stimulated emission, resulting in optical gain $g = -\alpha$. This is described by the Beer-Lambert law [117]

$$I(z) = I_0 \exp(-\alpha z) = I_0 \exp(gz). \tag{2.22}$$

Spontaneous emission is a source of noise in this context.

Devices such as lasers and optical amplifiers rely on stimulated emission to generate coherent light beams or to coherently amplify an optical signal, respectively. LEDs and optical spectroscopic techniques such as photoluminescence and cathodoluminescence (explained in Chapter B) function on the basis of spontaneous emission. Superluminescent LEDs are somehow intermediate, as they amplify spontaneous photons using stimulated emission.

Absorption and stimulated emission are opposite processes, and which one of the two will dominate, depends on their relative rate. If the majority of electrons are in the ground state, absorption dominates, while if the majority is in the excited state, stimulated emission will dominate and we have positive optical gain, or negative absorption. In a bulk semiconductor, where the two states are given by the valence and conduction band edges, the transparency criterion –i.e. $g = -\alpha = 0$– is given by the Bernard-Duraffourg condition [75, 125]

$$E_g \leq \hbar\omega \leq E_F^c - E_F^v, \tag{2.23}$$

where E_F^c and E_F^v are the quasi-Fermi level energies of the conduction and valence band, respectively. In other words, there will be positive gain as soon as there are sufficient electron-hole pairs in the system to separate the two quasi-Fermi levels by more than the bandgap. This concept can be easily transposed to the case of lower dimensionality systems.

Note that we consider an unbound electron-hole plasma here and we ignore excitonic effects. Indeed, even though gain from excitons is in principle possible and has been observed at room temperature in ZnO-based [94] and ZnSe-based structures [152] due to the elevated exciton binding energy in these materials, excitons in III-N structures dissociate before the onset of gain. Therefore, gain in III-nitrides is a phenomenon that is occurring beyond the Mott transition with a negligible excitonic contribution [124, 153].

In a typical LD or semiconductor optical amplifier (SOA), in order to enhance the light-matter interaction, the optical field that is to be amplified is confined in a waveguide and the active region consists of QWs. An important geometric parameter in such a structure is the confinement factor Γ, which is defined as the total normalized overlap integral between the QWs and the optical waveguide mode, and is determined as [75]

$$\Gamma = \sum_i \Gamma_i, \text{ with } \Gamma_i = \frac{\int_{y_i - d/2}^{y_i + d/2} \varepsilon(y) |E(y)|^2 dy}{\int_{-\infty}^{+\infty} \varepsilon(y) |E(y)|^2 dy} \tag{2.24}$$

where the index i represents the different QWs, Γ_i is the confinement factor of QW i, $\varepsilon(y)$ is the position-dependent dielectric permittivity, $E(y)$ represents the electric field amplitude of the optical mode and y_i the position of QW i. In a typical structure, a single QW has a confinement factor of a few % [153].

The optical gain that represents the amplification experienced by a waveguided optical field is the net modal gain g_{mod}. It is related to the material gain g_{mat} of the QWs and the waveguide absorption losses α_{wg} by

$$g_{mod}(\hbar\omega) = \Gamma g_{mat}(\hbar\omega) - \alpha_{wg}(\hbar\omega). \tag{2.25}$$

In order to adequately model the net modal gain, of a waveguide with GaN/AlGaN QWs, we have to take both the A and B valence bands into account [124]. The C band is too far away to be substantially populated with holes under typical conditions. Therefore, we consider the QW transitions occurring between the conduction and the A and B valence subbands, which are separated by transition energies E_{tr}^{A} and E_{tr}^{B}, respectively. The carrier population in these states is governed by the corresponding Fermi-Dirac distributions, f_c and f_v, respectively [75]:

$$f_c^j(\hbar\omega) = \left[1+\exp\left(\frac{E_{tr}^j + \frac{m_r^j}{m_e^*}(\hbar\omega - E_{tr}^j) - E_F^c}{k_B T}\right)\right]^{-1}, \tag{2.26}$$

$$f_v^j(\hbar\omega) = \left[1+\exp\left(\frac{-\frac{m_r^j}{m_j^*}(\hbar\omega - E_{tr}^j) - E_F^v}{k_B T}\right)\right]^{-1}, \tag{2.27}$$

with $j = A,B$, and where $m_r^{A/B} = (\frac{1}{m_e^*} + \frac{1}{m_{A/B}^*})^{-1}$ is the reduced mass with $m_{A/B/e}^*$ representing the effective mass of the A and B holes and that of the electron, respectively. The quasi-Fermi level of the conduction band can be easily determined as a function of injected carrier density N from:

$$E_F^c = E_{tr} + k_B T \ln\left(\exp\left(\frac{N}{N_c^e}\right) - 1\right). \tag{2.28}$$

In a valence band comprised of both an A and a B subband, E_F^v is determined implicitly from:

$$N = N_c^A \ln\left[1+\exp\left(\frac{E_A - E_F^v}{k_B T}\right)\right] + N_c^B \ln\left[1+\exp\left(\frac{E_B - E_F^v}{k_B T}\right)\right], \tag{2.29}$$

with E_A and E_B the band edge of the A and B subbands, respectively, and the two-dimensional (2D) critical carrier densities given by:

$$N_c^{A/B/e} = \frac{m_{A/B/e} k_B T}{\pi \hbar^2}. \tag{2.30}$$

The net modal gain is then given by:

$$g_{mod}(\hbar\omega) = -\alpha_{wg} + \sum_i \sum_{j=A,B} \Gamma_i \alpha_{2D}^j (f_c^j(\hbar\omega) - f_v^j(\hbar\omega))\theta(\hbar\omega - E_{tr}^j), \tag{2.31}$$

where the index i represents the different QWs, α_{wg} corresponds to the absorption loss in the waveguide, α_{2D}^j is the 2D absorption of the QWs in the two-band approximation as given by Eq. 1.32, and θ represents an inhomogeneously broadened step function, namely the convolution of a Heaviside and a Gaussian function, which can be approximated by [153]:

$$\theta(\hbar\omega - E_{tr}) = \frac{1}{2}\mathrm{erf}\left(\frac{\hbar\omega - E_{tr}}{\sqrt{2}\gamma_{inh}}\right) + \frac{1}{2}. \tag{2.32}$$

The model described above allows to accurately describe gain and absorption occurring in QW waveguides and will be used in Chapter 5 to analyze the experimental results.

3 Multiple Quantum Wells in Lattice-matched III-Nitride Waveguides

In this Chapter, we discuss the optical properties of lattice-matched III-nitride slab waveguides featuring a GaN/$Al_{0.1}Ga_{0.9}N$ MQW active region grown on an AlInN bottom cladding. These structures will be used in the next chapters to demonstrate strong exciton-photon coupling (Chapter 4) and optical gain (Chapter 5). Section 3.1 illustrates the structural properties and confinement of guided modes in these structures. The electronic band structure is discussed in Section 3.2. Finally, we investigate the optical QW properties in Section 3.3. Details about the experimental techniques used in this chapter can be found in Appendix B. Most of the results presented in this chapter were published in the following two papers:

- J. Ciers, J. G. Roch, J.-F. Carlin, G. Jacopin, R. Butté and N. Grandjean, *Propagating Polaritons in III-nitride Slab Waveguides*, Phys. Rev. Applied **7**, 034019 (2017).
- J. Ciers, G. Jacopin, G. Callsen, C. Bougerol, J.-F. Carlin, R. Butté and N. Grandjean, *Near-UV Narrow Bandwidth Optical Gain in Lattice-Matched III-Nitride Waveguides*, Jpn. J. Appl. Phys. **57**, 090305 (2018).

3.1 Sample Structure

From all the modes that can be confined in a c-plane III-N waveguide, the TE_0 mode is the most interesting one for light-matter coupling applications. It has no nodes in the waveguide core and extends little into the cladding layers, resulting in a good overlap with the active region, compared to higher-order TE modes. Since the A exciton and the A interband transition in GaN only couple to an electric field parallel to the c-plane, and the B exciton/interband transition preferentially couple to this polarization, as described in Section 1.2.4, the coupling to TE modes will be much stronger than to TM modes. Indeed, the in-plane electric field intensity, integrated over the active region, is over an order of magnitude smaller for TM modes compared to TE ones in the present structures, as calculated with FDTD [154].

In this work, we use waveguides with a GaN/AlGaN MQW active region operating around 345 and 370 nm, respectively, for their high quality and low inhomogeneous broadening [74]. An AlInN bottom cladding lattice-matched to GaN is used, which provides a large RIC with the active region of ~11% at 345 nm and ~7% at 370 nm, as discussed in Section 1.2.6, and assures a high crystalline quality of the QWs. The top cladding consists of either AlInN or SiO_2, as discussed below.

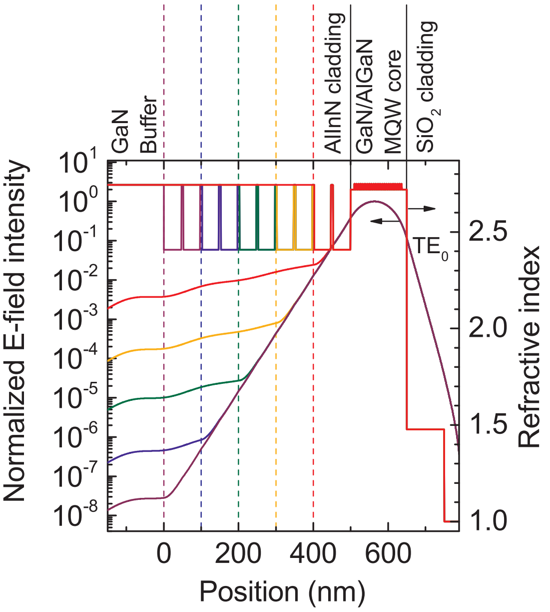

Figure 3.1 – Mode confinement and photon leaking into the GaN buffer of the TE_0 mode for various thicknesses of the AlInN cladding between 100 and 500 nm, as calculated by FDTD [154]. The different colors represent data for the different thicknesses (solid line). The dashed colored lines represent the corresponding interface between the cladding and GaN buffer. The refractive index for (Al)GaN was taken from [82], while it was taken from [29] for AlInN. The refractive index of SiO_2 was taken from experimental data.

In order to avoid coupling to multiple waveguide modes, which would act as a loss channel for the photogenerated carriers and would further complicate the analysis, we chose a core thickness that is small enough, to ensure that only the TE_0 and TM_0 modes are confined and the higher order modes are cut off. The coupling of the A and B transitions to TM-modes is negligible compared to the TE modes, as explained above. We did not choose to decrease the waveguide thickness even further, which would also cut off the TM_0 mode, since this would result in only a small reduction of L_{eff}, but a substantial reduction in N_{eff}^{QW} and Γ, and hence a decrease in light-matter coupling strength.

Since the entire structure has to be grown on a –high index– GaN buffer to ensure optimal material quality, we are in the case of frustrated total internal reflection. This means that the angle θ, as defined in Fig. 2.1 will again take a real value in the buffer and photons can leak through the bottom cladding. This is an undesirable photon loss channel that can be limited by increasing the AlInN cladding thickness, as illustrated in Fig. 3.1. For a cladding thickness of 400 nm, the probability to find photons in the buffer is $\sim 10^6$ times lower compared to the core, which is acceptably low, given that the absorption rate is only three orders of magnitude higher in the buffer (see Fig. 1.8) compared to the waveguide at 345 nm (see Chapter 4). This implies that losses due to photon leakage to the substrate are negligible compared to waveguide absorption for a bottom cladding thickness of 400 nm. At 370 nm, the situation is more favorable, as the buffer has a low absorption around 20 cm^{-1} [82]. Note that the 5 nm thick GaN interlayers have a negligible effect on the confinement of the optical mode.

A key feature to promote strong exciton-photon coupling up to room temperature is to have robust excitons with an elevated exciton binding energy. This can be obtained by employing narrow $GaN/Al_{0.1}Ga_{0.9}N$ QWs of 1.5 nm width, which have an exciton binding energy of 40 meV, as calculated using the $k\cdot p$ formalism [85]. An additional advantage of these narrow wells is a negligible impact of the QCSE [104] (see Section 1.2.3) leading to a large e-h overlap integral of 0.8 (also calculated using the $k\cdot p$ formalism), and a large oscillator strength of 1.1×10^{13} cm^{-2}, as determined from the experiments discussed in Chapter 4. The X_A transition of these wells varies between 345 nm (at low temperature) and 350 nm (at room temperature), as will be shown in Section 3.3. The dielectric material with the lowest absorption at these wavelengths is SiO_2 by plasma-enhanced chemical vapor deposition (PECVD) ($\sim$1 cm^{-1}).[1] This material also allows for the fabrication of high-quality grating couplers, as explained in Section 4.1. These features make SiO_2 an ideal top cladding material.

Taking these factors into account, a sample was grown by Dr. Jean-François Carlin, which will be called sample S1 throughout this manuscript. The structure is sketched in Fig. 3.2(a) and consists of a 130 nm thick active region with 22 GaN/$Al_{0.1}Ga_{0.9}N$ (1.5 nm/3.5 nm) QWs sandwiched between a 400 nm thick $Al_{0.83}In_{0.17}N$ bottom cladding lattice-matched to GaN and a 100 nm thick SiO_2 top cladding. A 2 μm GaN buffer, the bottom cladding and the active region were grown by MOVPE on a low dislocation density (10^6 cm^{-2}) freestanding c-plane GaN substrate. The AlInN bottom cladding layer contains seven 5 nm thick GaN interlayers positioned 50 nm apart in order to avoid kinetic roughening of the AlInN alloy [32], as explained in Section 1.1.3. The use of an AlGaN barrier width of 3.5 nm avoids any coupling between adjacent wells, as confirmed by $k\cdot p$ calculations [85], which are shown below. This structure is optimized to maximize the light-matter coupling strength g_0 between the guided photons and MQW excitons. The high number of QWs (22) combined with the large overlap between the optical mode and the QWs, which results in a confinement factor Γ of 28.6%, as illustrated in Fig. 3.2(b), and the large oscillator strength of the QWs result in a high g_0 value of 30 meV, which is demonstrated in Chapter 4. In Fig. 3.2, just like in the remainder of this manuscript, we chose the y axis parallel to the growth axis and set $y=0$ at the interface between the buffer and the bottom cladding.

A second sample (S2) was also grown to investigate the effect of an increased Al concentration in the barriers on the structural and optical quality. It features a nominally identical bottom cladding to S1 (400 nm of AlInN with seven 5 nm GaN interlayers), and a 52 nm thick active region with 7 GaN/$Al_{0.15}Ga_{0.85}N$ QWs. Just like in S1, the wells are 1.5 nm thick, while the barriers are 3.5 nm thick.

The optimal structure for the realization of optical gain is slightly different from the one of optimal exciton-photon coupling. A large number of QWs can provide elevated gain in a waveguide structure, but only provided that they are homogeneously pumped. Indeed, in an inhomogeneously pumped MQW structure, the wells with a low carrier density will absorb photons, i.e. they will have a negative gain, hence reducing the total MQW gain. Therefore, we chose a sample design with 6.2 nm wide GaN/$Al_{0.1}Ga_{0.9}N$ QWs, which emit below the bulk GaN bandgap (around 370 nm at room temperature) as a result of the QCSE, as explained in

---

[1] The absorption was determined by measuring the reflectivity and transmission of a 1 μm thick SiO_2 film grown on a double-side polished sapphire substrate using a Cary 500 spectrophotometer. The contribution the substrate was taken into account, and values were averaged between the interference fringes.

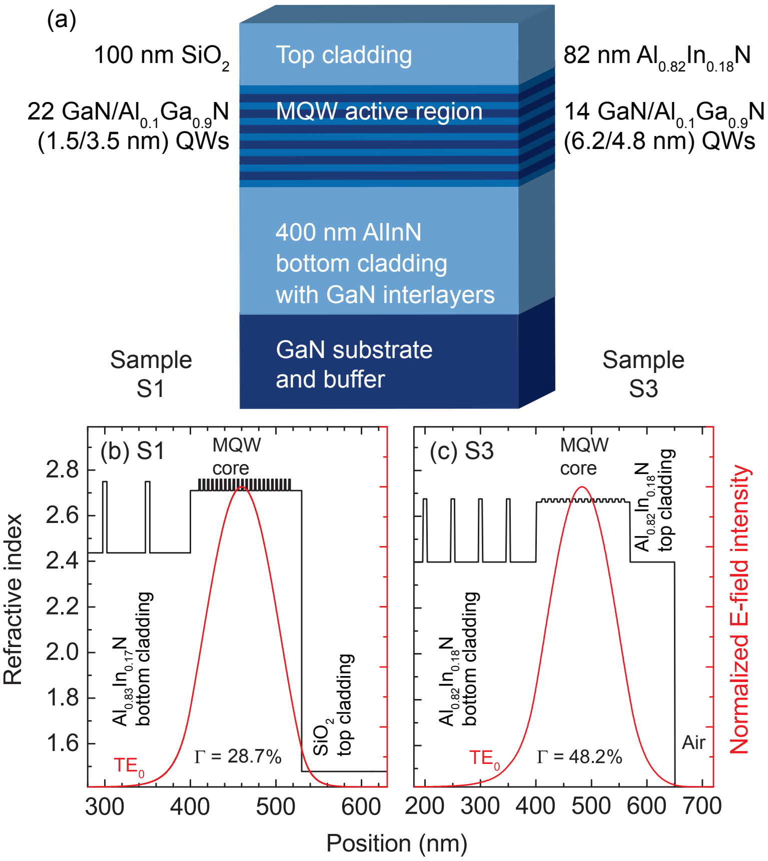

Figure 3.2 – (a) Sketch of the sample structure with details for samples S1 (left) and S3 (right). (b,c) Refractive index profile (black line) and optical mode profile (red line) of the TE$_0$ mode supported by waveguide S1 at 345 nm (b) and S3 at 370 nm (c). These mode profiles were calculated with an FDTD-solver [154]. The refractive index for (Al)GaN was taken from [82], while it was taken from [29] for AlInN. The refractive index of SiO$_2$ was taken from experimental data.

Section 1.2.3. Such wells can be excited by the available 355 nm laser, which is below the barrier absorption edge. Consequently, photons are only absorbed in the wells, and not in the barriers, which leads to a very homogeneous carrier injection, as detailed in Chapter 5. Note that we could have used narrower QWs if we had a shorter wavelength laser available, that is however still below the barrier band edge, with sufficient peak power to achieve the carrier densities required to reach optical gain. The reduced exciton binding energy in these wells of ~19 meV (calculated using the $k \cdot p$ formalism [85]) resulting from the QCSE (see Section 1.2.3) does not have any impact here, as the structure is operating beyond the Mott transition. The reduced electron-hole overlap of ~0.2 at low carrier density (also calculated using the $k \cdot p$ formalism [85]) does cause a decrease of the light-matter interaction, but this overlap is increased however, when the built-in field is screened under high injection, as explained in Section 1.2.7.

Under the typical optical injection conditions required for optical gain ($10^5 - 10^6$ W/cm^2), we observed that the SiO$_2$ films as used in S1, are damaged, likely due to local heating induced by laser absorption. Therefore, we also use a lattice-matched AlInN layer as top cladding, which is sufficiently robust and transparent (see Fig. 1.8) for this application. We chose a thickness of 82 nm to avoid extensive kinetic roughening without using a GaN interlayer [32]. As the latter would absorb some of the incoming pump photons.

Table 3.1 – Overview of the samples used in this work. All the structures were grown on c-plane freestanding GaN substrate.

	S1	S2	S3
Top cladding	100 nm SiO_2	none	82 nm $Al_{0.82}In_{0.18}N$
Active region	22 GaN/$Al_{0.1}Ga_{0.9}N$ (1.5/3.5 nm) QWs	7 GaN/$Al_{0.15}Ga_{0.85}N$ (1.5/3.5 nm) QWs	14 GaN/$Al_{0.1}Ga_{0.9}N$ (6.2/4.8 nm) QWs
Bottom cladding	400 nm (8 × 50 nm) $Al_{0.83}In_{0.17}N$ with seven 5 nm thick GaN interlayers	400 nm (8 × 50 nm) $Al_{0.82}In_{0.18}N$ with seven 5 nm thick GaN interlayers	400 nm (8 × 50 nm) $Al_{0.82}In_{0.18}N$ with seven 5 nm thick GaN interlayers

With this in mind, a third sample (S3) was grown, which is also sketched in Fig 3.2(a). It consists of a 170-nm-thick active region with 14 GaN/$Al_{0.1}Ga_{0.9}N$ (6.2 nm/4.8 nm) QWs sandwiched between bottom and top $Al_{0.82}In_{0.18}N$ claddings, which are lattice-matched to GaN. The 400 nm thick bottom cladding, just like in S1, contains seven 5-nm-thick GaN interlayers positioned 50 nm apart in order to avoid kinetic roughening of the AlInN alloy [32].

An overview of the samples discussed in this work can be found in Tab. 3.1.

The waveguide dimensions were chosen to support a single TE polarized mode, as described above, at 345 (for S1) and 370 nm (for S3), respectively. The mode profiles were calculated using FDTD calculations (see Appendix A) and are shown in Figs. 3.2(b) and 3.2(c), for S1 at 345 nm and S3 at 370 nm, respectively. The refractive index for (Al)GaN and AlInN layers were taken from refs. [82] and [29], respectively, and the SiO_2 data were issued from experiments. In both samples, the large RIC between the MQWs and the AlInN/SiO_2 cladding layers results in a small effective length L_{eff} of the TE_0 mode, of 88 and 99 nm, for S1 and S3, respectively, and a large overlap between the optical mode and the quantum wells. For S1, we calculated an effective number of QWs of 14.6 from this mode profile. In S3, the excellent spatial confinement, together with the large number of QWs, leads to a high Γ of 48.2%, compared to only a few % in standard laser diode structures featuring AlGaN claddings with low RIC [153]. Note, however, that such a high number of QWs cannot be efficiently pumped using an electrical injection scheme mainly due to the limited hole mobility. A similar WG with only 3 QWs near the peak of the modal field would have a Γ-value of 17% and would be better suited for electrical injection.

In order to examine the structural quality of the samples, high-resolution X-ray diffraction (HR-XRD) measurements were performed by Dr. Jean-François Carlin at LASPE, and are shown in Fig. 3.3. The experiments were performed in a Bruker D8 Discover X-ray diffractometer and the results were analyzed using the Bruker Leptos software. The coupled scans shown in Figs. 3.3(a), 3.3(b) and 3.3(c) for samples S1, S2 and S3, respectively, confirm the aforementioned layer thicknesses and compositions. We can see the main peaks coming from the GaN, AlGaN and AlInN layers, as well as the satellites from the MQW and AlInN/GaN superlattice. The MQW satellites in S3 are closer to the main AlGaN peak in reciprocal space compared to S1 and S2, due to the increased period in real space. We can also notice that the AlGaN peak is substantially broadened in S2, compared to S1 and S3, due to the increased Al content. Note a small difference in AlInN composition between samples S2 and S3 with ∼18% In, and sample S1 with ∼17% In. This is a consequence of the sensitivity to surface temperature during growth of the AlInN alloy, as discussed in Section 1.1.3. These compositions are however close enough from lattice-matching to GaN to obtain high-quality samples. This property is illustrated by the XRD reciprocal space map of S1 in Fig. 3.3(d), which shows that the bottom cladding and active region are fully pseudomorphic to the freestanding GaN substrate.

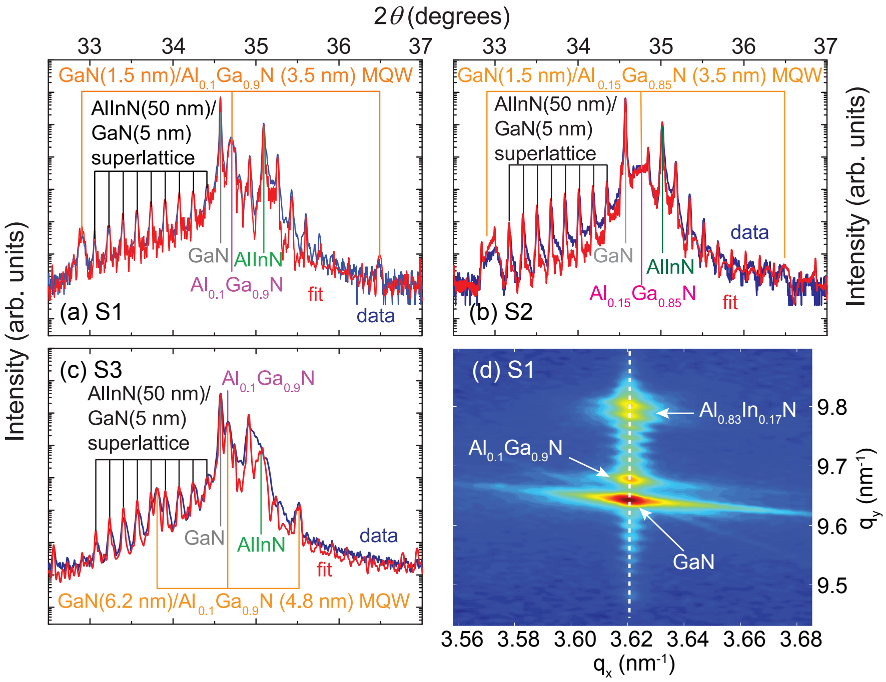

Figure 3.3 – XRD characterization of samples S1, S2 and S3. (a,b,c) Coupled HR-XRD scan of the (0002) reflex along the [0001] direction for samples (a) S1, (b) S2 and (c) S3 . A model of the structure (red) was fitted to the measured data (blue) with the layer thicknesses and the alloy composition used as fitting parameters. The results correspond to the values given in the text. (d) XRD reciprocal space map of the $(10\bar{1}5)$ asymmetric reflections on sample S1 showing that the bottom cladding and the active region are pseudomorphic to the freestanding GaN substrate.

High-resolution transmission electron microscopy (HRTEM) images were taken on a cross-section of sample S3 by Dr. Catherine Bougerol at Institut Néel, CEA and University of Grenoble, France, with a FEI-Tecnai 200 kV microscope using a high-angle annular dark-field detector in the [10-10] zone-axis orientation. These images are shown in Fig. 3.4 and are in good agreement with the XRD measurements. The HRTEM results show clear atomic planes and sharp interfaces between the QW and barrier layers. There is a fair contrast between the GaN and AlGaN layers, despite the low Al concentration in the latter.

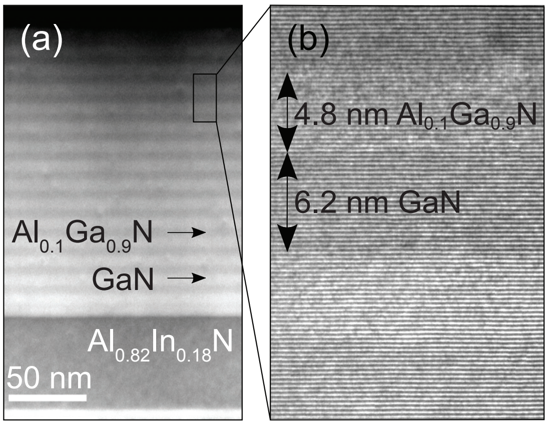

Figure 3.4 – (a) Scanning TEM image of the MQWs in sample S3 taken with a high-angle annular dark-field detector in the [10-10] zone-axis orientation. (b) High-resolution TEM image of the QWs in the same sample showing sharp interfaces and clear atomic planes. (Images courtesy of Dr. C. Bougerol, CEA and University of Grenoble)

3.2 Band Structure

In order to fully understand the optical properties of the samples under investigation and explain the experimental results that will be discussed below, we calculated their band structure in the one-electron picture using Nextnano [155]. Excitonic effects were added through a $k \cdot p$ solver [97, 119].

The resulting band structure for S1 is shown in Fig. 3.5(a). Due to the large spontaneous polarization mismatch between GaN and AlInN, the GaN interlayers in the bottom cladding have a large built-in electric field. For such structures, experimental values between 2.2 and 3.6 MV/cm have been reported [30, 52, 67]. Consequently, the photoluminescence (PL) emission of such 5 nm thick GaN interlayers lies in the green [67].

As a result of the geometric effect in MQW structures, the electric field in the GaN/$Al_{0.1}Ga_{0.9}N$ QWs is reduced to ~480 kV/cm [105]. The QW ground state electron and hole envelope wavefunctions that exist in such a potential are shown in Fig. 3.5(b). Note that the envelope wavefunctions of both the electron and hole fall to zero before reaching the adjacent well. This confirms the absence of both tunneling and hence minibands [76]. The overlap integral between the electron and hole amounts to 0.8 due to the narrow width of the QWs of 1.5 nm. Low-temperature excitonic energies $E_{X_A} = 3.590$ eV and $E_{X_B} = 3.600$ eV are obtained for X_A and X_B, respectively, using the calculated exciton binding energy of 40 meV in both cases [101]. The relative oscillator strength of the X_A (0.5 for light polarized along both x and z, 0 along y) and X_B excitons (0.495 for light polarized along both x and z, 0.01 along y) shows an exclusive coupling for X_A and a heavily preferential coupling for X_B to the in-plane electric field.

Analogous calculations for S2 reveal a built-in electric field of ~700 kV/cm, due to the increased spontaneous and piezoelectric polarization mismatch between the GaN wells and $Al_{0.15}Ga_{0.85}N$ barriers. The exciton binding energy amounts to 44 meV, for both X_A and X_B, as a result of the increased confinement. The e-h overlap integral remains equal to 0.8. This results in calculated values of $E_{X_A} = 3.615$ eV and $E_{X_B} = 3.625$ eV at low temperature. Note that the exciton energies are higher in these QWs, compared to S1, which confirms that the increased confinement

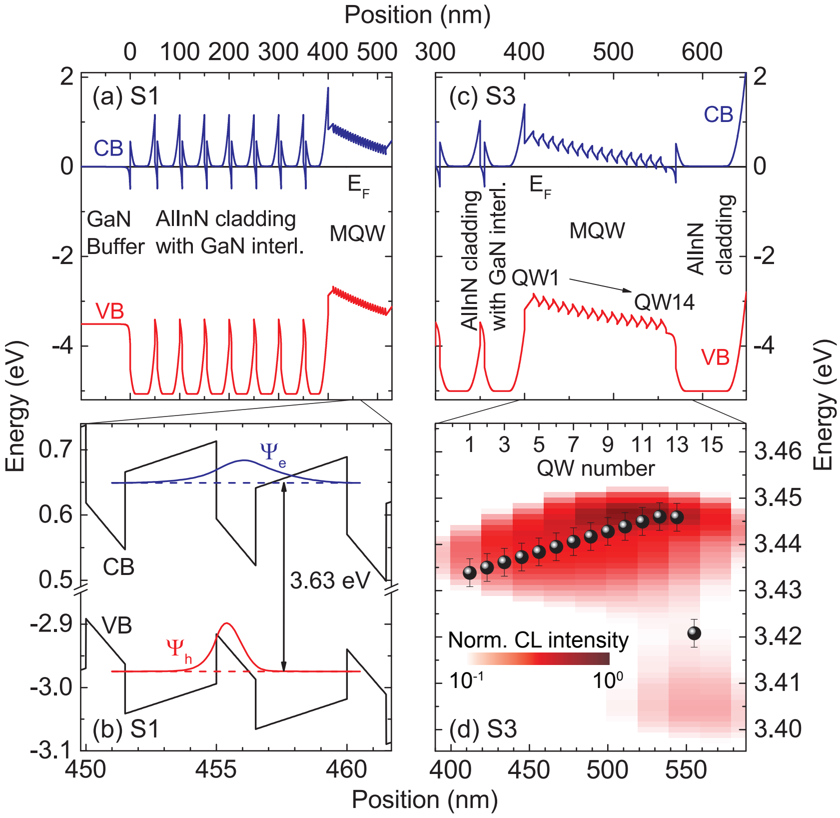

Figure 3.5 – Band structure of samples S1 and S3. (a) Full band diagram of S1, as calculated using Nextnano [155]. (b) Detail of the band structure of a QW in sample S1 (black), together with the electron (blue) and hole (red) envelope wavefunction of the QW ground state, as calculated using the $k \cdot p$ formalism [85]. (c) Band diagram of S3, as calculated using Nextnano [155]. (d) Low temperature ($T = 11$ K) cathodoluminescence (CL) cross-section mapping of the QW emission (logarithmic color scale) recorded with an acceleration voltage of 2 kV, along with the X_A energy of the different QWs (black dots) as deduced from the calculations shown in (c). The excitonic effects were calculated using the $k \cdot p$ formalism [85]. Under the present experimental conditions, the spatial CL resolution is ~50 nm.

dominates over the increased built-in electric field for this QW thickness of 1.5 nm [104].

In sample S3, the situation is more complicated as a result of the AlInN top cladding. The results of the band calculations are shown in Fig. 3.5(c). The Fermi energy was pinned to the mid-gap at the sample surface [156] and the electric field in the QWs was set to ~300 kV/cm, a value expected from the polarization mismatch between the multilayer constituents when taking into account the geometric effect [106]. We see that the elevated spontaneous polarization mismatch results in a 2DEG potential at the interface between the MQWs and the top cladding. In this situation, the residual donors in the MQW region are ionized and the resulting free electrons form a 2DEG just below the interface with the top cladding. The positively charged donors cause a slight band bending and a variation of the built-in electric field over the MQWs. Such an effect is not present in samples S1 and S2. The dangling bonds at the interface between the III-N and SiO_2, which result from the non-epitaxial character of the SiO_2 layer, will form interface states which partially compensate the plane charge that is due to the polarization mismatch between AlGaN and SiO_2. This phenomenon is modeled in Nextnano by Fermi pinning at this interface. Consequently, as can be seen in Fig. 3.5(a) for S1, the potential variation over the MQWs in S1 and S2 is small, and a negligible amount of unintentional donors is ionized. In this case, band-bending is absent and the different QWs therefore have the same built-in electric field and an equal transition energy. The residual doping level in sample S3 is difficult to assess experimentally –e.g., through C-V measurements[157]– for this sample due to the presence of the 2DEG at the interface between the MQW region and the top cladding layer. We know however that the typical residual n-type doping levels amount to 5×10^{18} cm^{-3} in similar AlInN layers [30] and $\sim 1 \times 10^{16}$ cm^{-3} in GaN/AlGaN QWs [157].

In order to be able to compare our calculations to experiments, we included excitonic effects through the $k \cdot p$ solver mentioned before [97, 119]. We found exciton binding energies of 19 ± 1 meV, depending on the exact built-in field magnitude in each QW, using the variational approach developed by Leavitt and Little [101]. The calculated low temperature QW exciton energies were compared to cathodoluminescence measurements recorded along the cross-section of sample S3 (Fig. 3.5(d)).[2] We observe an increase in the calculated exciton energy from QW1 to QW13 due to a decreasing built-in electric field, which is well-matched by the experiment. This is a direct consequence from the ionized unintentional donors in the MQWs and the presence of the 2DEG potential at the AlGaN/AlInN top interface, as discussed above. Note however that the top QW (QW14) deviates from this trend and has a lower emission energy and a higher built-in field due to its location near the 2DEG. The discrepancy between the calculated X_A energy and the emission is a consequence of bound exciton emission, which will be explained in Section 3.3.

3.3 Optical Characterization of the Quantum Wells

A series of spectroscopic experiments were conducted on samples S1, S2 and S3 in order to fully characterize the optical properties of the QWs. The results of these experiments will be illustrated in this Section. The micro (μ-)PL experiments on samples S1 and S2 discussed here were performed together with Jonas Roch, master student at EPFL-LASPE, under the supervision of the author. The time-resolved PL (TRPL) and PL excitation (PLE) measurements were performed by Dr. Gwénolé Jacopin and Dr. Gordon Callsen, respectively.

3.3.1 Intrinsic QW Transition energy

The intrinsic QW transition energies were studied experimentally by photoreflectance (PR) and PLE spectroscopy, for samples S1 and S3, respectively. The PR data for sample S1 between 10 and 300 K are shown in Fig. 3.6(a). Clear signatures can be observed for the X_A and X_B

---

[2] These experiments were conducted by Dr. Gwénolé Jacopin.

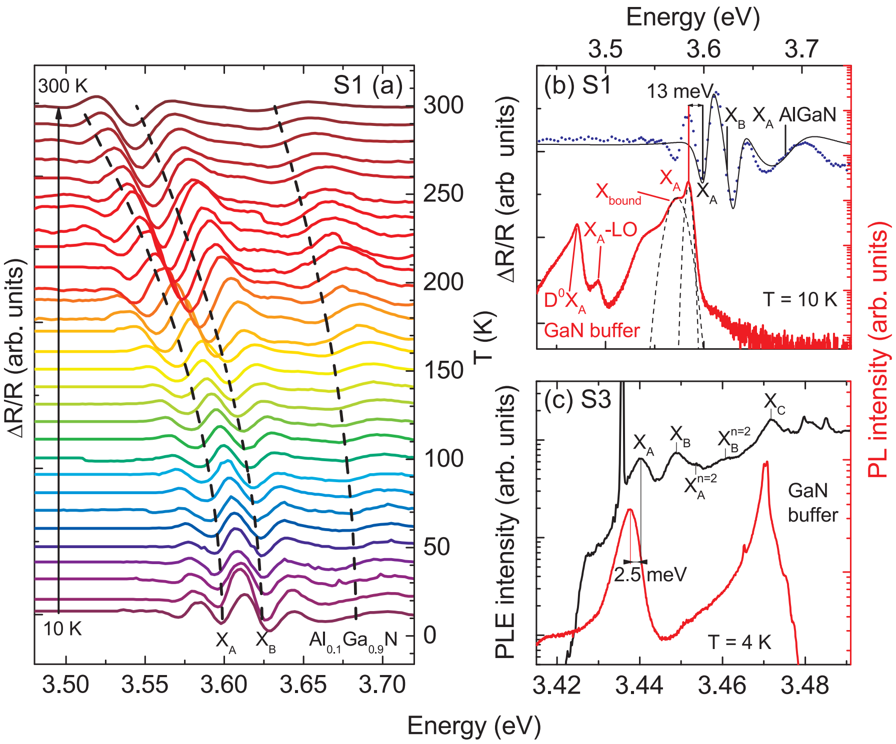

Figure 3.6 – (a) Photoreflectance measurements performed on sample S1 between 10 and 300 K. Features from the QW A and B excitons, as well as from the barrier A exciton can be clearly resolved. The critical points are traced by the black dashed lines. (b) Low temperature ($T = 10$ K) PR (blue dots) and μ-PL (red line) spectra taken at approximately the same location showing a Stokes shift of 13 meV in sample S1. A fit to the PR data according to Eq. 3.1 is shown (black solid line), as well as two Voigt functions that were simultaneously fitted to the X_{bound} and X_A PL peak (black dashed line). (c) Low temperature ($T = 4$ K) PLE spectrum (black line) and corresponding PL spectrum (red line) recorded at an excitation wavelength of 355 nm showing a Stokes shift of 2.5 meV in sample S3. The peak excitation power density was 60 kW/cm^2 for these measurements.

QW excitons as well as the X_A barrier exciton, which are located at 3.599, 3.623 and 3.683 eV, respectively, at $T = 10$ K. No signature of the underlying freestanding GaN substrate was observed in PR as the modulation induced by photogenerated carriers is limited by the pump laser absorption thickness of ~100 nm, and therefore essentially occurs in the topmost layers. The critical points were fitted using the approach introduced by Aspnes [110, 158], where the signature in differential reflectivity coming from a resonance at energy E_{tr} can be written as

$$\frac{\Delta R}{R}(\hbar\omega) = \Re\left(C_{PR}\exp(i\theta_{PR})(\hbar\omega - E_{tr} + i\gamma_{PR})^{-m_{PR}}\right), \tag{3.1}$$

where C_{PR} is a normalization factor, θ_{PR} is a phase factor which represents the asymmetry of the lineshape, γ_{PR} represents the width of the transition, and m_{PR} depends on the dimensionality of the critical point. In the case of a QW, m_{PR} is equal to 3 [159]. A fit to the measured data of Eq. 3.1 for the three critical points is shown in Fig. 3.6(b). We observe a redshift of 50 meV, 77 meV and 90 meV for the barrier band edge transition, QW X_B and QW X_A transitions between 10 and 300 K, respectively.

The comparison between low-temperature PL and PR spectra, as shown in Fig. 3.6(b), reveals a Stokes shift of 13 meV in S1, which is similar to that previously reported for a sample with 67 GaN/$Al_{0.2}Ga_{0.8}N$ (1.2/3.6 nm) QWs grown on sapphire [110]. We fitted the PL data to a Voigt function, which is a convolution of a Gaussian and a Lorentzian peak function, since we have a system that is both homogeneously and inhomogeneously broadened [77]. At low temperature, 10 K in this case, we have a purely Gaussian peak shape, since phonon-induced homogeneous broadening is negligible. With increasing temperature, the Lorentzian linewidth broadening increases, while the Gaussian part remains constant with temperature. The inhomogeneous broadening of the X_A PL peak is 8 meV, which compares favorably to state-of-the-art single GaN/AlGaN QW samples with a similar barrier composition. An inhomogeneous broadening of 11 meV was reported for a GaN/$Al_{0.09}Ga_{0.91}N$ single QW sample [74]. Note that since the PL and PR measurements were conducted with the sample mounted in different cryostats, there is an uncertainty of ~500 μm –comparable to the PR spot size– on the relative sample location probed in both experiments.

Low-temperature polychromatic PLE experiments were conducted on sample S3. A representative PLE spectrum obtained for an excitation power density of 60 kW/cm^2 is shown in Fig. 3.6(c). We verified that despite the high excitation power density, no shift in exciton energy was induced. In fact, the MQW region remains in the low carrier density regime due to the limited absorption –on the order of 1% per QW, as determined from the product $\alpha_{2D} d_{QW}$, cf. Eq. 1.32– occurring in the QWs for near-resonant excitation below the AlGaN barrier band edge. We observe resonances coming from the three free excitons at 3.440, 3.449 and 3.472 eV for X_A, X_B and X_C, respectively, which match well with the energies deduced from the $k \cdot p$ formalism, as well as weak absorption features ascribed to the $n = 2$ state from the A and B exciton hydrogen series [77](cf. Eq. 1.16). The measured PLE FWHM of 11 meV for the X_A transition corresponds well with the calculated energy spread of QW1 to QW13 shown in Fig. 3.5(d). The PL spectrum obtained during the same experiment for the excitation wavelength of 355 nm is also shown in Fig. 3.6(c). A PL linewidth of 5 meV is measured for the X_A QW peak while a Stokes shift of 2.5 meV is obtained with respect to the PLE peak.

These low values of the Stokes shift and PL linewidth, compared to an inhomogeneous PLE broadening of 11 meV, an be ascribed to the gradient in the MQW energies discussed in Section 3.2. Indeed, since the top QWs are transparent for the resonant energy of the bottom ones, the entire stack of QWs is probed using PLE. On the contrary, for PL measurements the laser excitation is mostly absorbed in the top QWs and hence emission is dominated by high-energy QWs. This reduces the measured Stokes shift and the PL linewidth. This effect is further enhanced for PL experiments where 325 nm excitation above the barrier band edge is used (these experiments are discussed below). Due to the shorter absorption length, PL emission is dominated by even fewer QWs. In this case the Stokes shift between the PLE and PL peaks is reduced to 1 meV. This is contrary to the case of sample S1, where all QWs have the same built-in field, and no reduction of the broadening or Stokes shift occurs, regardless of the injection conditions.

Let us note that the low inhomogeneous broadening of 5 meV deduced from low temperature PL measurements is likely inherited from the low E_B of 19 meV stemming from the small electron-hole wavefunction overlap of ~0.2. This E_B value translates into a large exciton Bohr radius $a_B = 5$ nm, compared to typical values around 3 nm in III-N quantum heterostructures. As a consequence, the exciton wavefunction is spread over a larger volume than for its narrow GaN/AlGaN MQW counterparts. For comparison, the elevated exciton binding energy of 40 meV in S1 results in an exciton Bohr radius of 2.5 nm. This means that the excitons in S1 will probe an area that is 4 times smaller in the QW plane, resulting in an increased sensitivity to well width fluctuations and alloy disorder, as illustrated by the differences in inhomogeneous broadening between S1 (8 meV) and S3 (5 meV). A substantial part of the latter value is coming from the difference in built-in electric field between the QWs.

3.3.2 Low Carrier Density Photoluminescence

We performed temperature-dependent photoluminescence measurement series on samples S1, S2 and S3, between 11 and 300 K. The results for S1 are shown in Fig. 3.7(a). For the low-temperature PL spectra, we can clearly identify the X_A MQW exciton at 3.591 eV together with its first LO-phonon replica, at ~92 meV below the main peak, which is the accepted LO-phonon energy for GaN [93]. An inhomogeneous broadening of 8 meV is measured at 11 K for the X_A peak. On the low-energy side of the X_A exciton, we observe a second peak which is likely due to a bound excitonic state, X_{bound}. This is compatible with the fact that this peak disappears for higher temperatures, as the bound excitons thermally escape. This bound state could originate from monolayer well-width fluctuations, since it is located 13 meV below the X_A peak. Indeed, this is exactly the position where one can expect the X_A energy of a similar QW with a built-in field of ~480 kV/cm which is 2.59 Å wider [49] (cf. $k \cdot p$ calculations [85]). At low temperatures, a third peak is present at ~3.55 eV. This energy corresponds to the maximum of the polariton emission –see Chapter 4– and as such, this peak could be the signature of scattered lower polaritons. From 30 K onwards, we can observe a shoulder on the high-energy side, which is likely originating from the X_B exciton. It is located 10 meV above the X_A peak, which is where we would expect X_B, according to the calculations discussed in the previous section. We do not observe any signature from the AlGaN barriers in PL measurements, since these layers are sufficiently thin and there is no strong localization due to alloy disorder, all carriers relax into the wells.

The analogous measurement series for sample S2 is illustrated in Fig. 3.7(b). We observe the same features as for S1 –X_A peak, X_{bound} peak and their LO-replicas–, albeit at higher energy –the X_A peak is at 3.621 eV for $T = 11$ K– and broader –the X_A peak has a linewidth of 10 meV at 11 K–. These effects are a result of the increased confinement and increased alloy disorder due

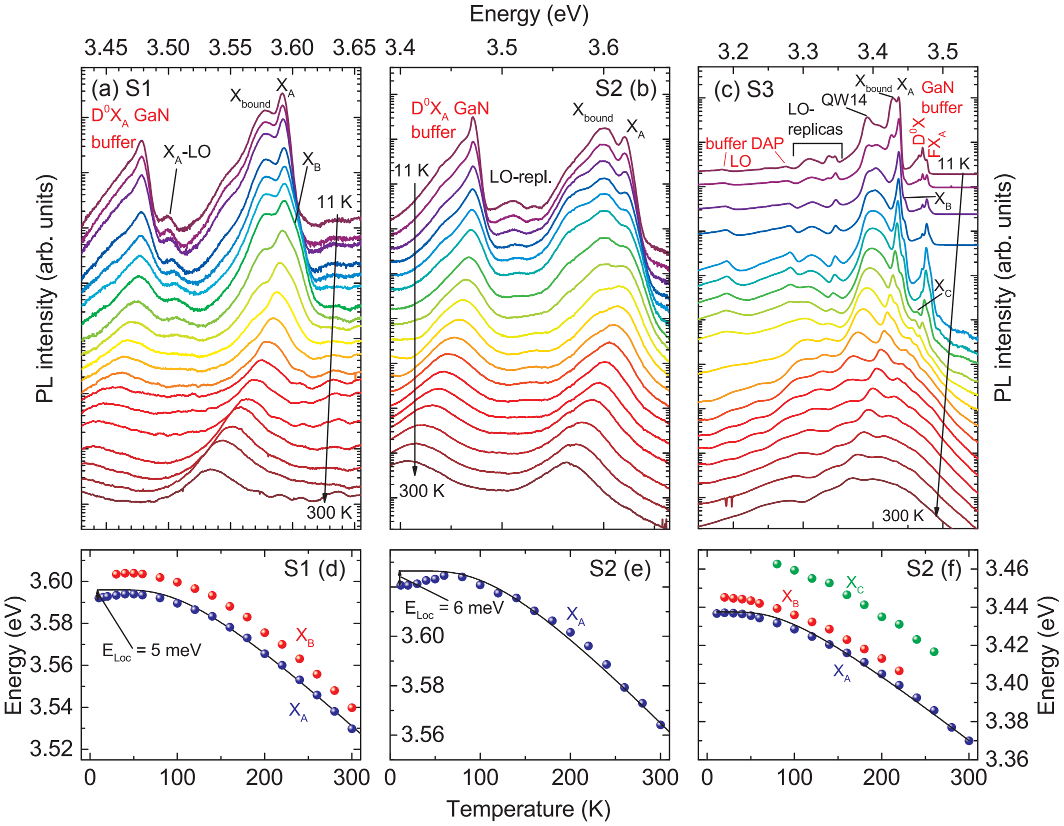

Figure 3.7 – (a,b,c) Temperature series between 11 and 300 K of PL spectra using the HeCd laser ($\lambda = 325$ nm) excitation obtained from sample (a) S1 with an excitation power density 20 W/cm^2, (b) S2 with 40 W/cm^2 and (c) S3 with 24 W/cm^2. The spectra are vertically shifted for clarity. Luminescence peaks coming from the GaN buffer are labeled in red, while peaks originating from the QWs are labeled in black. (d,e,f) Temperature dependence of the visible excitonic peaks as deduced from the PL measurements shown in (a,b,c), for samples (d) S1, (e) S2 and (f) S3, together with a fit of the X_A energy according to Eq. 1.6 (black line).

to the higher Al content in the barriers (15% vs. 10%). Also in this case we observe the X_{bound} peak at the energy where we would expect a QW that is one monolayer wider, which is now 20 meV below the X_A peak, due to the increased built-in field of 700 kV/cm. As a consequence of the increased broadening in this sample, we can not clearly resolve the X_B peak in these spectra.

The results for the PL temperature series performed on sample S3 are shown in Fig. 3.7(c). We observe the peaks from both QW1-13 and QW14. As for samples S1 and S2, we see both the free X_A and the bound exciton peak (likely due to monolayer well width fluctuations) for the top and lower lying QWs. Like in the previous two cases, we observe the bound exciton peak exactly where it is expected for a QW that is 1 monolayer thicker, namely 8 and 11 meV, for QW1-13 and QW14, respectively. the splitting is larger for QW14, due to the increased built-in field, as discussed in Section 3.2. Another consequence of the increased built-in field, is a larger penetration of the electron and hole envelope wavefunctions into the barriers, which results in

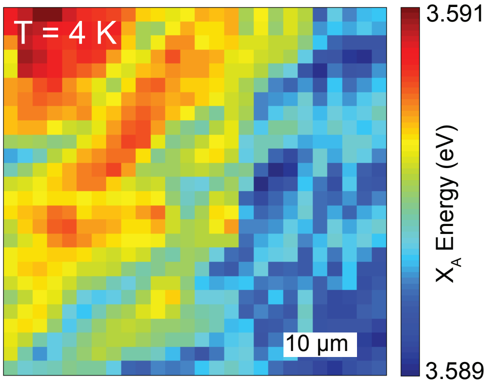

Figure 3.8 – μ-PL mapping of the X_A emission energy of sample S1 measured at 4 K. The observed standard deviation is as low as 0.42 meV over a 50 × 50 μm^2 area.

an increased inhomogeneous broadening of ∼14 meV for QW14, compared to 5 meV for QW1-13. The low magnitude of the latter value is a consequence of the increased exciton Bohr radius in these wide QWs, as explained before. We can also follow the X_B and X_C transitions of QW 1-13 from 20 and 60 K onward, respectively. Above 30 K, the contribution originating from the X_{bound} transition disappears likely due to exciton delocalization. We observe the LO-phonon replicas of both X_{bound} and both X_A peaks 92 meV below their respective main peaks. The two small peaks emerging around 3.275 and 3.183 eV at $T = 11$ K are attributed to the donor-acceptor pair (DAP) transition occurring in the buffer and its LO-phonon replica, respectively [160, 161].

We traced the PL emission energies of the excitonic peaks as a function of temperature, by fitting a sum of Voigt peak functions, as illustrated in Fig. 3.6(b). The results are shown in Fig. 3.7(d-f) for samples S1, S2 and QW 1-13 of sample S3, respectively. Upon fitting the measured X_A PL emission energies to Eq. 1.6, we find a localization energy E_{loc} of 5 meV for S1, 6 meV for S2 and –remarkably– a value as low as 1 meV for S3. The fit parameters that were used for Eq. 1.6, were $\alpha_B = 70$ meV and $\Theta_B = 345$ K for S1, $\alpha_B = 75$ meV and $\Theta_B = 370$ K for S2 and $\alpha_B = 58$ meV and $\Theta_B = 308$ K for S3. These values are in good agreement with those reported by Brunner *et al.* for bulk (Al)GaN layers [82].

The localization energies observed for samples S1 and S2 (5 and 6 meV, respectively) can be easily understood in terms of their inhomogeneous PL broadening (8 and 10 meV, respectively). At low temperature, the carriers relax to the lowest-energy states of the inhomogeneously broadened ensemble. This typically results in a localization energy that is comparable to the inhomogeneous broadening [133]. The situation in S3, however, requires some deeper analysis. The observed localization energy of 1 meV is substantially lower than the inhomogeneous broadening deduced from low temperature PL data. Just like the reduced PL linewidth and SS described above, this effect is a direct consequence of the built-in field gradient in the MQWs leading to a spread in the QW energy combined with the inhomogeneous pumping profile resulting from nonresonant excitation above the barrier band edge. At low temperature, the high-energy QWs are the main contributors to the observed X_A peak. With increasing temperature, carrier diffusion increases and the lower energy QWs receive a higher carrier density hence leading to a redshift in the X_A peak that compensates for the blueshift usually observed in the delocalization S-shape of GaN/AlGaN QWs [93]. In the case of samples S1 and S2, the inhomogeneous carrier distribution over the QWs does not lead to a reduction in the localization energy, since all QWs emit at the same energy, as explained in Section 3.2.

The in-plane homogeneity of sample S1 was also checked through μ-PL mapping performed at 4 K (Fig. 3.8), which leads to a standard deviation σ as low as 0.42 meV for the X_A energy over a $50 \times 50\ \mu\text{m}^2$ area. This shows the high degree of homogeneity of these samples, which is an important asset for both the control of waveguide polaritons [143] and the potential realization of photonic integrated circuits relying on such an approach, and for the realization of optical amplifier devices. This uniformity can likely be ascribed to the growth performed on low defect density freestanding GaN substrate, as these latter samples are expected to be much less affected by in-plane disorder than their counterparts grown on *c*-plane sapphire substrate [74, 162].

Comparing the experimental exciton energies with the calculated values, which were mentioned in Section 3.2, we observe a relatively good agreement. The energy of the free X_A exciton in sample S1 deduced fom PR measurements (3.599 eV at 10 K) and PL data in combination with Eq. 1.6 (3.596 eV at 11 K) is slightly higher than the value expected from $k \cdot p$ calculations (3.590 eV). The situation is similar in sample S2, with a value of 3.626 eV for E_{X_A} from PL and Eq. 1.6, compared to a calculated value of 3.615 eV. In sample S3 on the other hand, the values for E_{X_A} are in very good agreement, with 3.438 eV deduced from PL data and Eq. 1.6, and 3.440 eV for both the PLE peak and the average of the calculated energies for QW 1-13 (cf. Fig. 3.5). The observed underestimation of the X_A energy by the calculations for samples S1 and S2 can be explained by a reduction in the built-in field, e.g., due to screening by free carriers.

Due to the larger energy splitting between X_A and X_{bound} for QW14, the low temperature CL emission observed for this QW (see Fig. 3.5(d)) is mainly coming from X_{bound}, which is located about 15 meV below that of the free exciton, hence explaining the discrepancy seen between calculated and measured emission for this QW in Fig. 3.5(d). Note that in order to compensate for the lower emission energy experienced by the top QW due to its proximity with the AlGaN/AlInN interface, a correction in QW width or Al composition of the barrier could be implemented, or alternatively a larger barrier width before the waveguide/cladding interface could be used. It is worth pointing out that according to the mode profile shown in Fig. 3.2, the contribution of the top QW to the net modal gain amounts only to 40% of that of a QW located at the center of the waveguide.

If we consider the PL temperature series shown in Fig. 3.7, we notice that the integrated PL intensity of the QWs severely reduces with increasing temperature. This is a result of the linearly increasing radiative lifetime τ_r with temperature, which originates from the excitation of excitons out of the light cone when raising the temperature [163]. As a result of this reduced radiative recombination rate at higher temperatures, the internal quantum efficiency (IQE) is reduced. The

IQE is defined as the ratio of the radiative recombination rate on the total recombination rate:

$$\mathrm{IQE} = \frac{\frac{1}{\tau_r}}{\frac{1}{\tau_r}+\frac{1}{\tau_{nr}}} = \frac{\tau_{nr}}{\tau_r+\tau_{nr}}, \tag{3.2}$$

with τ_{nr} the nonradiative recombination lifetime. An approximate indicator of the IQE can be deduced from temperature-dependent PL measurements. If one assumes that nonradiative recombination is negligible at low temperature –a commonly used assumption that is not always correct [77]–, the IQE is approximately unity under these conditions. The IQE can then be approximated as

$$\mathrm{IQE}_{PL}(300\,\mathrm{K}) = \frac{I_{PL}(300\,\mathrm{K})}{I_{PL}(11\,\mathrm{K})}, \tag{3.3}$$

where I_{PL} represents the integrated PL intensity from the QWs, i.e. the X_A and X_{bound} peak combined. Here, the index 'PL' is used to distinguish this quantity from the real IQE. The IQE_{PL} of samples S1, S2 and S3 was measured for various excitation power densities in the low-density regime. In this regime, there is no screening in the built-in field and the radiative recombination rate is not enhanced by an increased e-h overlap. The observed changes in IQE with excitation power density, shown in Fig. 3.9, will therefore only be a consequence of the changing carrier density. The increase in IQE is ascribed to saturation of nonradiative recombination centers. Note that for these carrier densities, Auger recombination is negligible [163]. We notice that sample S3 has a lower IQE_{PL} than sample S1, which is a direct consequence of the increased radiative lifetime in S3, due to the reduced e-h overlap integral of 0.2, compared to 0.8 for S1. The IQE_{PL} of S2 rapidly decreases with decreasing power density, compared to S1. Since the QWs in both samples have similar e-h overlap integrals of 0.8, this could be explained by an increased nonradiative recombination rate in sample S2. Note that we do not expect an increased density of threading dislocations in S2, as all three samples are grown on similar freestanding GaN substrates with a low threading dislocation density on the order of 10^6 cm^{-2}.

3.3.3 Carrier Density Effects

Further characterization of the samples was performed by low-temperature excitation power dependent PL series, shown in Fig. 3.10. For sample S1, emission from the bound excitons dominates at low power (Fig. 3.10(a)), since excitons naturally relax into these potential traps, where they are well protected from nonradiative recombination centers. Upon increasing carrier density, bound exciton traps and nonradiative centers saturate, the free X_A peak appears and finally dominates the spectrum. We do not observe any blueshift of the emission with increasing excitation power, due to the negligible impact of the QCSE on these narrow wells

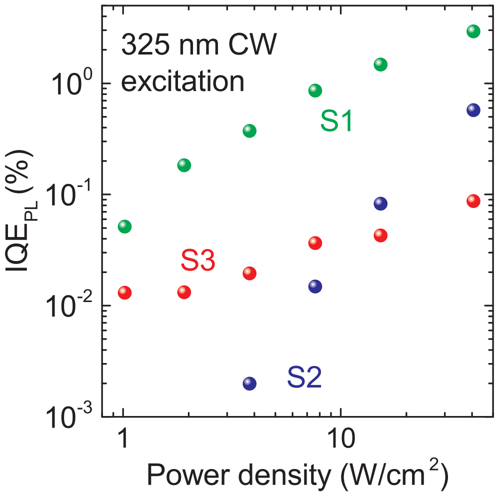

Figure 3.9 – Internal quantum efficiency of samples S1, S2 and S3 at room temperature under nonresonant continuous wave (CW) excitation.

[104]. If we increase the excitation power density by 5 orders of magnitude (as shown in Fig. 3.10(b)), using pulsed 266 nm laser excitation and a microscope objective, the X_{bound} peak again dominates over the free X_A. This is likely due to the biexciton emission coinciding with that of the bound exciton. The separation between the two peaks (12 meV) is close to the biexciton binding energy that can be expected following Haynes' rule [164, 165]. Additional support for this explanation will be given by the TRPL data discussed below. When further increasing the excitation power density, we observe a significant broadening of the emission, caused by phase-space filling and collisional broadening, as we go through the Mott transition [124]. An additional peak, that is attributed to amplified spontaneous emission (ASE), is observed for the highest power densities. Under these circumstances, broadening is usually mainly occurring on the high-energy flank of the peak [124], which is not the case here. This is likely a consequence of laser induced heating, which redshifts the emission with increasing power density. This can also explain the substantial redshift of ~20 meV of the X_A peak, with respect to the low carrier density PL experiments. Given the large number of QWs in this sample, which are inhomogeneously pumped above the barrier band edge in these experiments, a detailed quantitative analysis of these high-density effects is complex and outside of the scope of this thesis work.

Similar low carrier density low-temperature PL power series recorded on sample S3 are shown in Fig. 3.10(c). For low pump power densities, the top QW (QW14) dominates the emission spectrum due to its larger density of photogenerated carriers, and larger γ_{inh}, leading to a better radiative efficiency [93]. With increasing pump power density, the radiative efficiency of the other QWs (QW1-QW13) increases and they start to dominate the emission spectrum. We observe that both the emission from QW14 and that from QW1-QW13 consist of an X_{bound} and a free X_A peak, dominated in each case by X_{bound} at low power densities. In these wide QWs, we observe a very clear blueshift with increasing carrier density, due to screening of the built-in electric field. This is contrary to the case of sample S1, where no screening was observed due to the small impact of the QCSE on these narrow wells. This again confirms the importance of

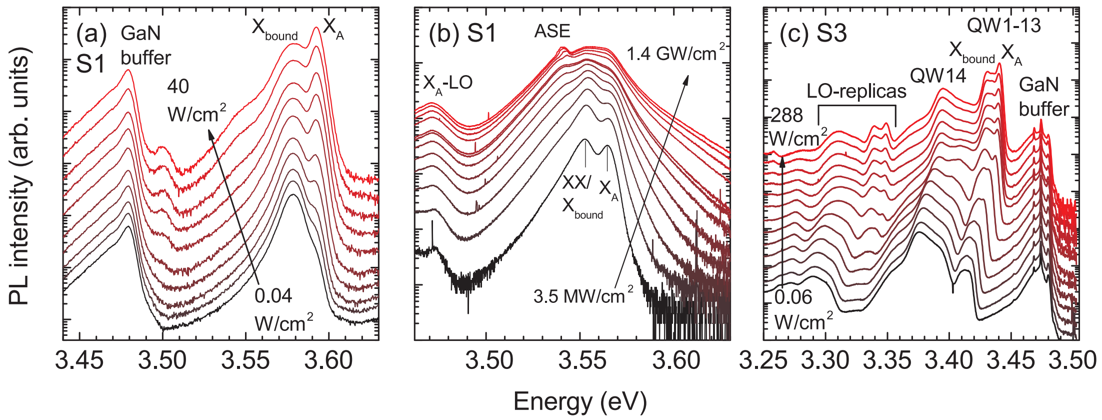

Figure 3.10 – Low-temperature PL excitation power dependent series performed on samples S1 and S3 under nonresonant excitation. (a) Low carrier density power series performed on sample S1 at $T = 11$ K using CW 325 nm excitation shows the emergence of the X_A peak with increasing excitation power density. (b) High density μ-PL power series measured on sample S1 at $T = 4$ K using pulsed 266 nm excitation focused to a 5 μm diameter spot. In the collection of the PL signal, we selected only the region of uniform peak power density through spatial filtering using a 50 μm pinhole. The biexciton peak is dominating the spectra at the lowest power densities and we observe a broadening of the peaks with increasing pump power due to the Mott transition to an e-h plasma. On the low-energy side of the biexciton peak, a new emission peak stemming from ASE appears for the highest power densities. (c) Low carrier density power series recorded on sample S3 at $T = 11$ K using CW 325 nm excitation. For low excitation power densities, the luminescence of the top QW (QW14) dominates the emission spectrum and no clear signature of the X_A peak is seen. The relative X_A intensity emerges only for sufficiently high carrier densities.

the QCSE on wide wells, like those used in sample S3 [104].

Low-temperature ($T = 15$ K) TRPL measurements recorded on sample S1 –shown in Fig. 3.11– confirm the conclusions of the low-temperature PL power series obtained on the same sample discussed above. Note also that in these measurements we did not observe any blueshift due to the screening of the built-in field. At low fluence (Fig. 3.11(a)), the bound exciton peak is dominant, while for medium fluence (Fig. 3.11(b)), the free X_A peak dominates. At even higher fluence, shown in Fig. 3.11(c), biexciton emission, which coincides with the X_{bound} peak, dominates the spectrum. This is also confirmed by the corresponding decay of the integrated intensities of both peaks shown in Figs. 3.11(d,e,f). If exciton and biexciton populations are in thermodynamic and chemical equilibrium –this equilibrium settles much faster than typical decay times [166]–, i.e. $2\mathrm{X} \rightleftharpoons \mathrm{XX}$, the mass action law requires that [166]

$$\frac{N_X^2}{N_{XX}} \propto \exp\left(\frac{-E_B^{XX}}{k_B T}\right). \tag{3.4}$$

In the case where radiative decay is dominant, and the PL intensity is proportional to the carrier

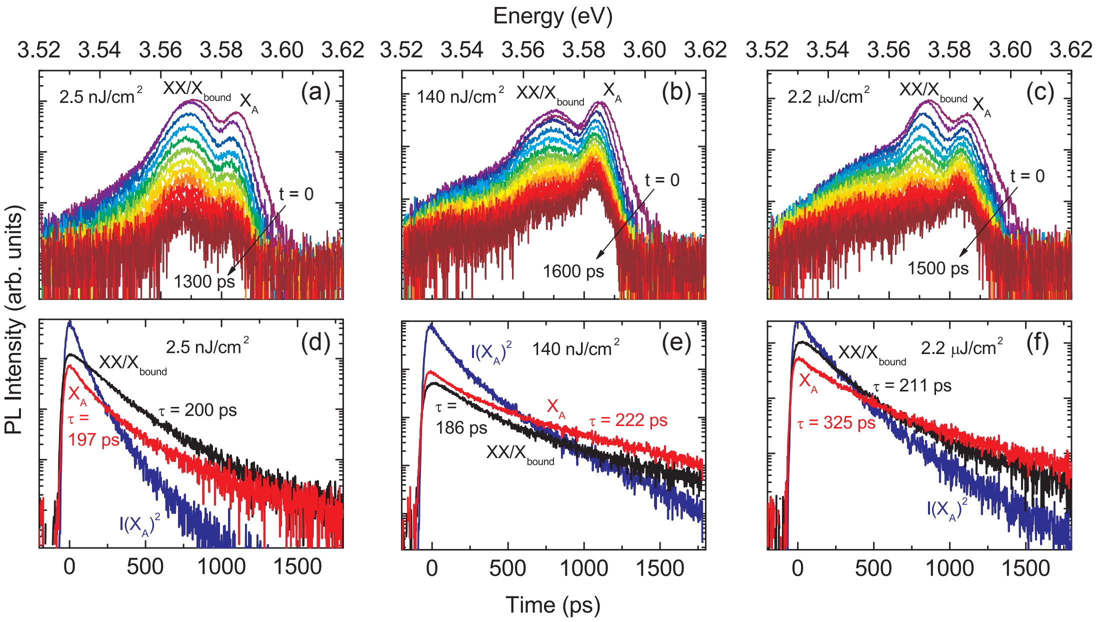

Figure 3.11 – TRPL measurements recorded on sample S1 at 15 K. (a,b,c) Time-resolved PL spectra for various time delays with respect to the arrival of the laser pulse. Consecutive spectra are separated by 100 ps. At low fluence (a), the bound exciton peak is dominant, while for medium fluence (b), the free X$_A$ peak dominates. At even higher fluence (c), however, the bound exciton peak seems to dominate again, which indicates a contribution of biexcitons to this peak at high carrier densities. (d,e,f) Decay of the integrated intensities of both peaks extracted from the measurements shown in (a,b,c), respectively, together with the squared intensity of the X$_A$ peak. We observe an increase in X$_A$ lifetime with increasing fluence, due to saturation of the non-radiative recombination channels. We also observe an increasing proportionality between the decay of the squared X$_A$ intensity and the XX/X$_{bound}$ intensity with fluence, which confirms an increasing contribution of biexcitons in the latter.

density of the corresponding species (which is the case for low temperature PL experiments), Eq. 3.4 implies that the squared intensity of the exciton emission should be proportional to the biexciton emission. Looking at the squared X$_A$ intensity decay in Figs. 3.11(d,e,f), we see that it is not proportional to the XX/X$_{bound}$ decay for the low fluence measurement shown in Fig. 3.11(d), but proportionality is improved with increasing fluence in Fig. 3.11(e) and especially in Fig. 3.11(f). This confirms an increasing biexciton contribution to the XX/X$_{bound}$ peak with increasing carrier density. We observe an increase in X$_A$ lifetime with increasing fluence due to saturation of alternative relaxation channels. We can therefore take the X$_A$ decay time of Fig. 3.11(f), as a good approximation of the radiative free X$_A$ lifetime.

The results discussed in this section highlight the high quality and the homogeneity of the present samples, which is a direct consequence of the lattice-matched nature of the structures. This makes them ideal for the study of propagating polaritons and narrow-bandwidth optical gain, which will be discussed in Chapters 4 and 5, respectively.

4 Waveguide Polaritons

In this Chapter, we discuss the properties of a lattice-matched III-nitride slab supporting waveguide polaritons originating from the hybridization of GaN/AlGaN MQW excitons with the propagating TE_0 optical mode. Section 4.1 explains the fabrication procedure for the grating couplers that were employed to study the waveguide dispersion, while Section 4.2 discusses the experimental technique used for dispersion measurements. Section 4.3 explores the light-matter coupling in the present sample and the polariton dispersion, while Section 4.4 illustrates the propagating polariton properties. Details about the experimental techniques used in this chapter can be found in Appendix B. Most of the results presented in this chapter were published in the following paper:

- J. Ciers, J. G. Roch, J.-F. Carlin, G. Jacopin, R. Butté and N. Grandjean, *Propagating polaritons in III-nitride slab waveguides*, Phys. Rev. Applied **7**, 034019 (2017).

4.1 Grating Coupler Fabrication

In order to couple the guided modes to free-space photons, grating couplers were defined on the sample [167]. Two types of gratings were used. The first experiments were done using a dielectric grating with a long coupling length of ~300 μm to avoid detrimental effects of the grating-induced photon loss on the SCR, while future experiments will make use of resonant excitation through a metal grating coupler with a much shorter coupling length of ~20 μm, due to the increased modulation in refractive index. These values were calculated by FDTD simulations [154]. The techniques that are used in the fabrication process are explained in Appendix B.

4.1.1 Dielectric Gratings

For the waveguides with dielectric grating couplers, the SiO_2 top cladding was deposited by PECVD on top of the active region. A 100 nm ZEP520A positive resist layer was spin-coated on the sample, the grating patterns were exposed with electron beam (e-beam) lithography, developed and subsequently etched into the SiO_2 layer with inductively coupled plasma reactive ion etching (ICP RIE) using CHF_3/SF_6 chemistry. This etching recipe allows a gentle etch that does not burn the ZEP resist layer and has a 2:1 selectivity with the resist. Early attempts using C_4F_8 chemistry burned the resist, resulting in rough and inhomogeneous gratings. Ultimately, the resist layer is removed with an oxygen plasma. The entire procedure is sketched in Figs.

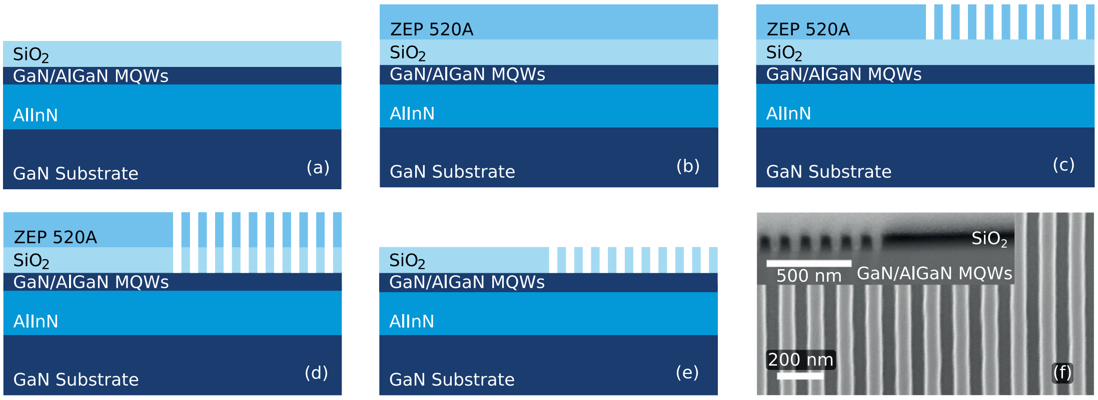

Figure 4.1 – Fabrication of dielectric grating couplers. (a) A 100 nm thick SiO$_2$ layer is deposited on the III-N structure by PECVD. (b) A ~100 nm ZEP resist layer is spin coated on the sample. (c) The resist is exposed using e-beam lithography and subsequently developed. (d) The grating pattern is etched into the SiO$_2$ layer using ICP RIE. (e) The resist layer is removed using an oxygen plasma. (f) SEM image of the dielectric grating coupler after etching, corresponding to (d). The main image shows the top view, while the inset shows a tilt-corrected cross-section view after focused ion beam milling.

4.1(a-e). A scanning electron microscopy (SEM) image of the fabricated structure in top view and cross-section is shown in Fig. 4.1(f). The etched sidewalls form an angle of 3° with the vertical. The aspect ratio of the etched slits is 5:3. The gratings have a period Λ of 125 ± 0.4 nm[1] with 50% fill factor and span over a 100×100 μm^2 area each.

4.1.2 Metal Gratings

Fabrication of the metal grating couplers is initiated by spin coating a poly(methyl methacrylate) (PMMA) double layer on the MQW region, where the bottom layer has a molecular mass of ~495 000 proton masses, and the top layer has a molecular mass of ~950 000 proton masses. Both the top and bottom layers are 40 nm thick, resulting in a total thickness of 80 nm. A thicker double layer reduces the resolution of the exposure, while a thinner layer further hinders the lift-off process. This makes the process inherently challenging and leads to a small resist thickness window where the process could work. After e-beam exposure and development, 20 nm of Al is evaporated on the sample, which is then left in acetone at 37°C for a few days. The gratings are then finally overcoated with SiO$_2$ by PECVD. The procedure is shown in Figs. 4.2(a-e). An SEM image of the fabricated structure in top view is shown in Fig. 4.2(f). The gratings have a period Λ of 130 nm with 50% fill factor and span over a 50×50 μm^2 area.

---

[1] The error bars on the grating period were determined from the angular linewidth of the outcoupled signal, as discussed in Section 4.4.

Figure 4.2 – Fabrication of metal grating couplers. (a) A PMMA double layer is spin coated onto the sample. (b) The resist is exposed using e-beam lithography and subsequently developed. The PMMA 495 layer has a lower dose threshold, which results in an undercut under the top PMMA 950 layer. (c) The Al film is deposited onto the sample using e-beam evaporation. Due to the undercut in the PMMA double layer, the parts of the Al film in the regions of exposed PMMA are not connected to the rest of the film and will not be affected by its lift-off. (d) The PMMA layer is lift-off with the superfluous Al in acetone at 37°C. (e) The SiO_2 top cladding is deposited. (f) Scanning electron micrograph of the Al grating coupler after lift-off, corresponding to (d).

4.2 Fourier-Space Spectroscopy with Real-Space Filtering

In order to determine the properties of propagating polaritons, which will be discussed hereafter, we need to measure the dispersion of the guided modes as a function of propagation distance. For this purpose, we used a laser excitation spot that can be scanned over the sample, since the distance between the excitation spot and the grating coupler is equal to the propagation distance. Moving the excitation spot proved to be more practical than moving the sample and grating coupler, since it does not require to realign the collection optics, and thus makes it easier to compare measurements. Second, in order to reconstruct the guided mode dispersion curve, we need information from both k-space (given by the emission angle from the grating coupler, as described by Eq. 2.11) and the frequency domain. Such information can be obtained by using Fourier-space spectroscopy (not to be confused with Fourier-transform spectroscopy, which is often used in the IR). To understand this technique, one should note that a lens performs a spatial Fourier transform between the front and back focal planes. Indeed, the light that is emitted from the front focal plane along a specific direction is focused onto a single point in the back focal plane. Therefore, the back focal plane –also called Fourier plane for this reason– can be seen as an angular map of the front focal plane. In order to measure the guided mode dispersion from our waveguides, we place the sample in the front focal plane of a large numerical aperture (NA = 0.55) microscope objective, in order to have a wide angular field of view, oriented such that polaritons propagate vertically, i.e., parallel to the spectrometer slit. The objective's Fourier plane is then imaged onto the entrance slit of an imaging spectrometer, which images the k-space information on the vertical axis of the charge-coupled device (CCD). The photons are energetically dispersed in the horizontal direction by the spectrometer grating and we obtain a dispersion measurement on the CCD in a single shot.

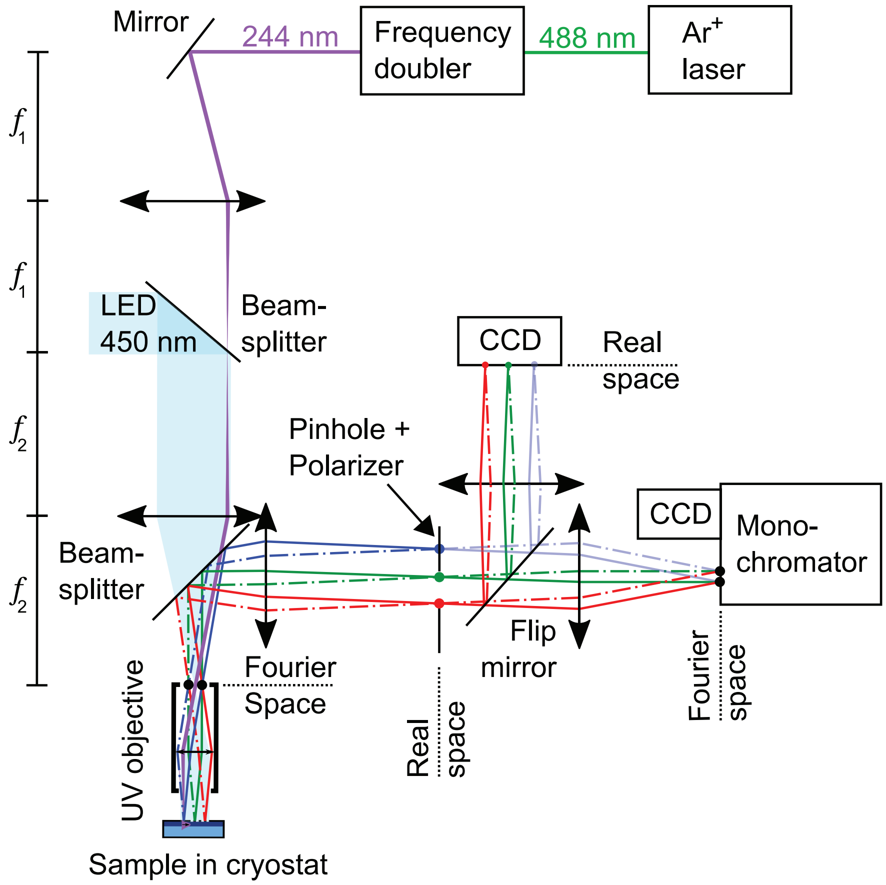

Figure 4.3 – Sketch of the Fourier-space spectroscopy setup. The excitation laser is represented in purple. The light emitted from the sample is represented in red, green and blue with the different colors indicating different locations on the sample. The solid and the dashed lines represent two different emission angles. The Fourier space is marked by black dots and the real space by colored dots.

The experimental setup was first developed by Jacques Levrat and Marlene Glauser [168] and was further improved for the present work. It is sketched in Fig. 4.3. A CW frequency-doubled Ar$^+$ laser emitting at 244 nm was used for the excitation. This laser beam was coupled into an 80× UV microscope objective – with NA = 0.55 and a 350 μm field of view – through a so-called $4f$-configuration of two lenses and a mirror. The laser spot diameter on the sample was about 5 μm. This configuration allows to scan the excitation spot over the sample within the field of view of the objective in the two dimensions by rotating the mirror. The light emitted by the sample was then collected through the same objective lens and the Fourier plane was imaged onto the spectrometer entrance slit by two lenses. The spectrometer consists of a liquid-nitrogen cooled back-illuminated UV-enhanced CCD mounted on a 55 cm focal length monochromator.

A pinhole was placed in the first real-space image plane of the sample to select only the light emitted from the grating coupler. The pinhole diameter of 1.5 mm corresponds to a 19 μm circle on the sample with the lens combination used here (objective with 2.5 mm focal length and lens with 200 mm focal length). A wire grid polarizer with an extinction coefficient of better than 100:1 between 300 and 400 nm was positioned immediately after the pinhole to perform polarization-dependent measurements and reduce the amount of randomly polarized PL signal with respect to the TE-polarized guided mode of interest. The first real-space image plane was imaged onto a second UV-enhanced CCD for real-space observation of the sample. A blue LED was used for illumination. The sample was mounted in a cold-finger continuous-flow liquid-helium cryostat, with a temperature controller that is continuously adjustable between 4 and 350 K.

4.2.1 Alignment and Measurement Procedure

To start a measurement, the sample should be mounted in the cryostat with the propagation direction that is to be measured along the vertical, and the grating lines along the horizontal. To facilitate this, it is convenient to have the gratings parallel or perpendicular to a specific edge of the sample, which can then be used for orientation with the naked eye. One should aim to get the angle between the propagation direction and the vertical smaller than a few degrees to get good results.

Second, the back focal plane of the objective has to be imaged onto the monochromator slit and CCD. In an imaging monochromator such as the one used here, the slit is automatically imaged onto the CCD. To do this, a homemade auxiliary part is used. This part is shown in Fig. 4.4(a) and features the same thread as the objective, and a drawing of a crosshair. When mounted in the objective holder, the plane of the crosshair coincides with the back focal plane of the objective, while the small circle indicates the size of the Fourier space. The two lenses in the collection line are to be positioned to image the crosshair onto the CCD. To achieve this, the crosshair is illuminated using the LED and the second lens of the excitation line. As a starting position, the crosshair should be in the front focal plane of the first lens and the spectrometer slit should be in the back focal plane of the second lens. Here, we used lenses with a focal distance of 20 cm and 25 cm, respectively. This gives a slight magnification of the Fourier space, so that it nicely fits the CCD. Note that the focal length of a lens decreases with decreasing wavelength, since the refractive index increases. The crosshair image can be found and coarsely brought onto the slit, using a piece of paper. The fine adjustment of the two lenses should be done observing the focus and position of the crosshair image onto the CCD.

Third, the laser excitation line should be setup. Once the pump laser and frequency doubler unit are well adjusted, a spatial filtering telescope can be inserted between the frequency doubler and the mirror if a small, diffraction limited spot size of ~1 μm is required onto the sample. However, this leads to much reduced excitation power. As a first step, the laser beam should be aligned to coincide with the optical axis without the two $4f$ lenses, using two pinholes. The laser should hit the crosshair right in the center. The two lenses can then be put into place. We

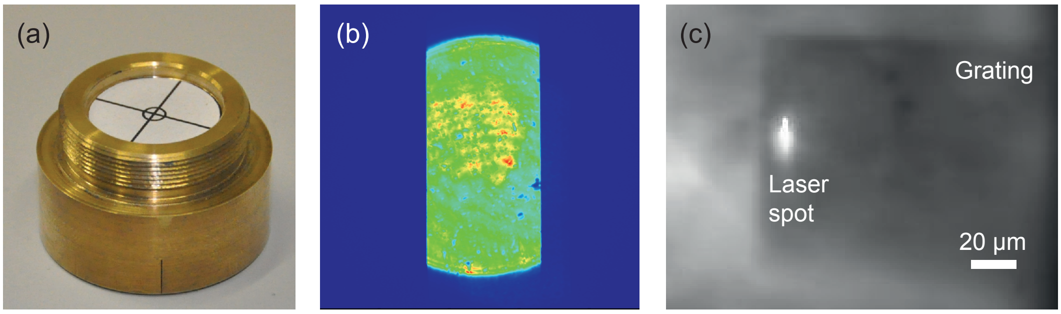

Figure 4.4 – Alignment procedure of the Fourier setup. (a) Home-made auxiliary part to image the back focal plane onto the spectrometer. Reproduced from [168]. (b) Image of the Fourier plane on the spectrometer CCD with open slit (of 2.2 mm). (c) Real space image of the sample, where we observe the grating coupler and the PL coming from the laser spot.

used a 30 cm focal length (27 cm at 244 nm) and a 15 cm focal length (13.5 cm at 244 nm) lens. The mirror should therefore be positioned 81 cm away from the objective's back focal plane. We put the lens with the shortest focal length in front of the objective to cover a larger incoupling angle, which corresponds to a larger scanning range over the sample. The fine adjustment of the two lenses can be achieved by verifying that the beam is parallel to the optical axis between the two lenses and always hits the crosshair in the center for every mirror angle.

Next, we mount the UV objective and put the sample in its focus. Adding a 280 nm long pass filter in the collection line allows to observe the sample PL in the spectrometer without reflected laser light. By fully opening the monochromator slit and setting the grating to zero-order diffraction, we observe an image of the slit on the CCD, corresponding to the Fourier plane of the emission. We then finely adjust the sample position and the two lenses in the collection line to image the Fourier plane in-focus. At the end of this procedure, the Fourier plane image should be a well-defined disk in the center of the CCD, as shown in Fig. 4.4(b). We know that the edges of this disk correspond to the NA of the objective, which is 33° in this case. We can therefore use the top and bottom edge to calibrate the emission angle onto the CCD.

After that, the real-space CCD and lens have to be aligned such that a sharp real-space image of the sample can be seen on the former, under illumination with the LED, such as shown in Fig. 4.4(c). The LED beam is focused onto the back aperture of the objective, which results in a large spot on the sample, covering nearly the entire field of view. Then, we put the pinhole in the real space plane to select the grating region, and put the laser excitation spot in the center of the collection region. This allows fine adjustment of the sample focus by observing the Fourier image. If the sample is out of focus, the outer part of the Fourier image will be clipped by the pinhole.

Finally, we move the laser spot away from the collection region (the dimensions of the grating coupler can be used to determine the distance), close the slit, and put the monochromator grating to the wavelength where the emission is expected. The waveguide dispersion can then be observed onto the CCD. One should be careful however not to close the slit too much at first, since the waveguide dispersion can be slightly off the slit center due to a slight rotation of the

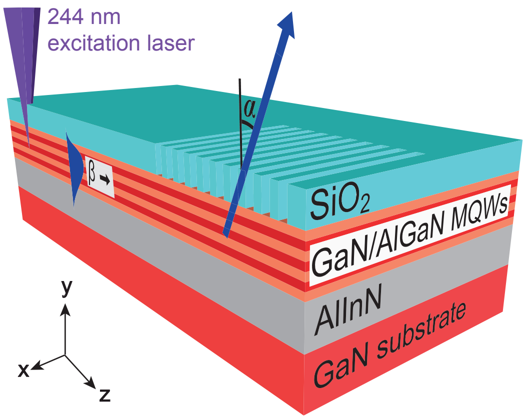

Figure 4.5 – Sketch of the polariton waveguide under investigation in this chapter.

sample or an imperfect centering of the Fourier image on the slit. In general, 0.5 mm is a good first step to find the dispersion curve. After the dispersion curve signal intensity is optimized by horizontally adjusting the collection line, the slit can be closed further, down to 0.2 or even 0.1 mm. The relative intensity of the dispersion curve with respect to the background can be increased by adding a (wire grid) polarizer in the collection line. Since the mode we studied here is TE polarized, the electrical field lies in the plane of the optical table and the polarizer should be oriented accordingly.

4.3 Strong Light-matter Coupling in III-N waveguides

The waveguide that will be studied in this chapter, is sketched in Fig. 4.5. It is based on sample S1, which was presented in Chapter 3 and features several dielectric grating couplers, as described in Section 4.1.

In the present structure, three different light-matter coupling regimes can potentially coexist in distinct zones of the energy vs. β diagram shown in Fig. 4.6. Photons with an in-plane wavevector outside the active region light cone do not exist. Therefore, radiative recombination of excitons in this region is forbidden and these are called dark excitons. In the k-space region between the bottom cladding and the active region light cone, photons are tightly confined in the waveguide by TIR and, as will be shown hereafter, they hybridize with the X_A excitons. Inside the bottom cladding light cone, TIR is lost at the bottom interface and the active region becomes a lossy resonator with broad optical modes. Therefore excitons and photons are weakly coupled in this region. Inside the top cladding light cone, TIR is also suppressed at the top interface and the structure forms a low quality factor Fabry-Perot resonator with $Q \sim 1$. As a result, we simultaneously have three populations of excitations in the sample under CW non-resonant excitation: dark excitons, waveguide polaritons, and weakly coupled excitons. The latter population allows us to probe the bare excitonic properties inside the air light cone using conventional optical spectroscopy techniques as shown in Chapter 3.

The waveguide dispersion curve was measured using Fourier-space spectroscopy with real-

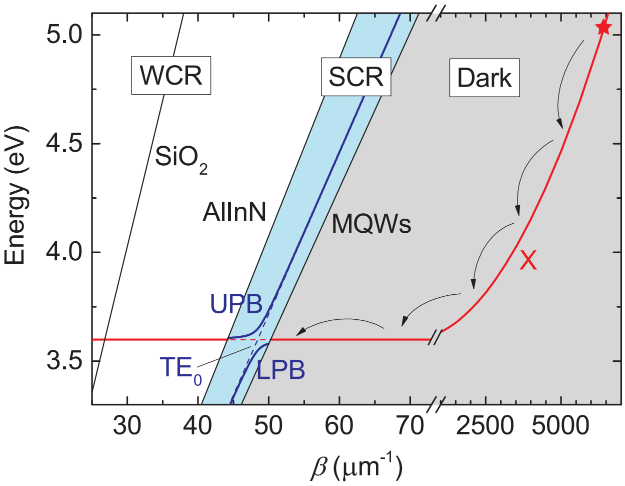

Figure 4.6 – Eigenmode dispersion of the present structure for TE polarization, i.e. along x. The light cones of the MQWs, bottom cladding (AlInN) and top cladding (SiO_2) are represented in black. They mark the transitions between the different light-matter coupling regimes. The dark regime occurs outside the active region light cone (marked in grey) where photons do not exist. Between the active region and the bottom cladding light cone, the exciton (X, red) and TE_0 guided mode are in the strong coupling regime (SCR, blue) and form an upper (UPB) and a lower polariton branch (LPB). Within the bottom cladding light cone, photons are poorly confined and couple weakly with the excitons (WCR, white). The star marks the energy at which carriers are injected in the present experiments. The arrows represent carrier relaxation. For simplicity, refractive index dispersion was neglected in this plot. The considered optical refractive index values are those expected at 3.6 eV (2.756 for the active region [82], 2.42 for the bottom cladding [29] and 1.47 for the top cladding). The exciton dispersion is calculated within the effective mass approximation.

space filtering, which is explained in Section 4.2, for various propagation distances, by moving the excitation spot away from the grating outcoupler between 4 and 100 K. The measured signal intensity is relatively weak for two reasons. First, only excitons lying outside the cladding light cone and inside the MQW light cone are expected to form polaritons, as shown in Fig. 4.6, hence the fraction of excitons outside this region does not contribute to the signal. Second, due to the radial symmetry of the waveguide around the excitation spot, only a small fraction of the generated polaritons actually reaches the grating coupler. This will be further illustrated in Section 4.4.

Additionally, the IQE of the active medium decreases with increasing temperature, which further reduces the signal intensity at higher temperatures. This is illustrated in Fig. 4.7. The LPB intensity, integrated over the entire branch and measured 50 μm away from the excitation spot, decreases with temperature. This is a consequence of the same physical phenomenon that reduces the luminescence IQE explained in Section 3.3.2. Excitons are excited out of the region of SCR, which is marked in blue in Fig. 4.6, when raising the temperature. If we compare the LPB intensity with the MQW PL intensity (obtained for a similar carrier density as for the LPB observation spot, $\sim 1 \times 10^{10}$ cm^{-2}), we see that the former drops much more rapidly than the

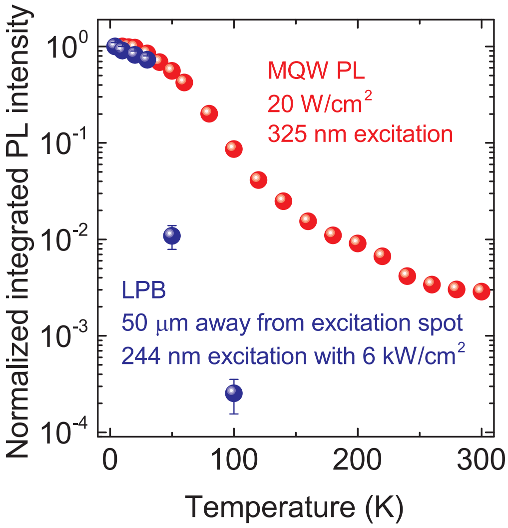

Figure 4.7 – Integrated LPB intensity (blue dots) at a distance of 50 μm from the excitation spot, compared to the integrated MQW PL intensity (red dots) as a function of temperature. In both cases, the low-temperature density of excitons/polaritons was $\sim 1 \times 10^{10}$ cm^{-2} at the observed location. The total carrier density in the excitation spot was 2×10^{12} cm^{-2} for the polariton intensity shown here, resulting in a carrier density per QW that is an order of magnitude lower. For the MQW PL, this density was estimated from the injected laser power. For the LPB, the density was estimated from the measured signal intensity. For the LPB, the intensity was integrated over the entire branch.

latter with temperature above 30 K. Several physical mechanisms might explain this strong decrease in LPB signal intensity. There could be an increased sensitivity to nonradiative defects due to the delocalized character of polaritons [77]. The hybrid light-matter nature of polaritons results in a wavefunction with an intermediate size between the exciton Bohr radius and the optical wavelength. As such, these polaritons probe the QW potential landscape averaged over 10 – 100 nm [169]. On these scales, disorder is small and localization is negligible in this sample, as was illustrated in Chapter 3. Polaritons are therefore more likely to encounter a nonradiative defect, reducing the intensity of the measured signal. In addition, thermally activated interactions of polaritons with acoustic phonons –such as the E_2^{low} phonon, which has an energy below 18 meV near the center of the first Brillouin zone [170]– might lead to a depopulation of the LPB. It could occur towards both the dark and WCR regions shown in Fig. 4.6. This picture would be consistent with the increase of the density of phonon states between 0 and 20 meV [170], and could therefore account for the observed reduction in LPB intensity above 30 K.

Above 100 K, the signal intensity became too weak to perform any reliable measurements. Note however, that this does not imply that the SCR could not be maintained above 100 K, since the lifetime broadening associated with the nonradiative recombination –which is far below 1 meV, as discussed in Section 1.2.5– is negligible with respect to the normal mode splitting of ~60 meV we observe here (see hereafter).

The detected signal intensity could be significantly increased by using resonant excitation, which would couple most of the pump power directly into the waveguide polariton states, and/or by implementing ridge structures for lateral confinement. Note that in the case of resonant excitation through a grating coupler, polaritons are injected with a well-defined wavevector. Consequently, they will propagate in a single direction –towards the grating outcoupler– and dilution should be drastically reduced, even without lateral confinement. Such approaches

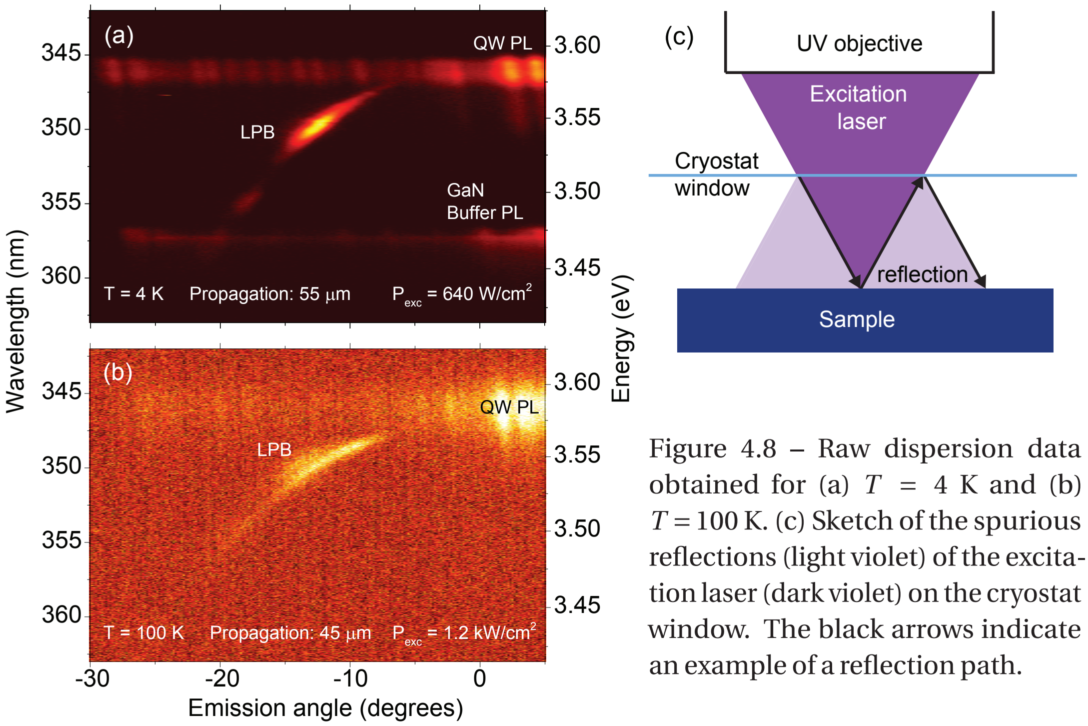

Figure 4.8 – Raw dispersion data obtained for (a) $T = 4$ K and (b) $T = 100$ K. (c) Sketch of the spurious reflections (light violet) of the excitation laser (dark violet) on the cryostat window. The black arrows indicate an example of a reflection path.

would circumvent the current limitations of our measurements and likely allow for polariton propagation studies up to higher temperatures.

Two examples of dispersion curves measured at $T = 4$ and 100 K are shown in Figs. 4.8(a) and 4.8(b), respectively. We clearly see a pronounced curvature in the measured signal, which is ascribed to the anticrossing of lower polaritons with the uncoupled free X_A transition. The signal-to-noise ratio of the measurement at 100 K is severely reduced, due to the decreasing IQE described above. We also notice a dispersionless signal at the PL emission energy of the QWs and the substrate. This spurious PL signal could have two origins: (i) PL emission at the excitation spot that propagates to the collection spot, through reflections on the sample interfaces and/or the cryostat window, e.g., or (ii) laser light that arrives at the collection spot, due to reflections on the cryostat window, as illustrated in Fig. 4.8(c). Tests with a patterned mesa sample, which was provided by Ian Rousseau from EPFL-LASPE, showed that (ii) is the dominant mechanism. This spurious PL complicates the analysis of the data and even renders the LPB signal invisible for short propagation distances. As a result, it is not possible to perform meaningful measurements for propagation distances shorter than ~20 μm.

We did not observe the UPB in any of the experiments. Such an absence is a well-known feature of wide band gap systems [103, 171], which is mainly due to absorption occurring above the MQW band gap and the large Ω_{Rabi} value, which hinders the thermal promotion of polaritons to the UPB [172]. However, let us note that even in GaAs-based polariton waveguides, the UPB luminescence is usually rather weak or even absent [144, 145, 173]. For the same reasons, we

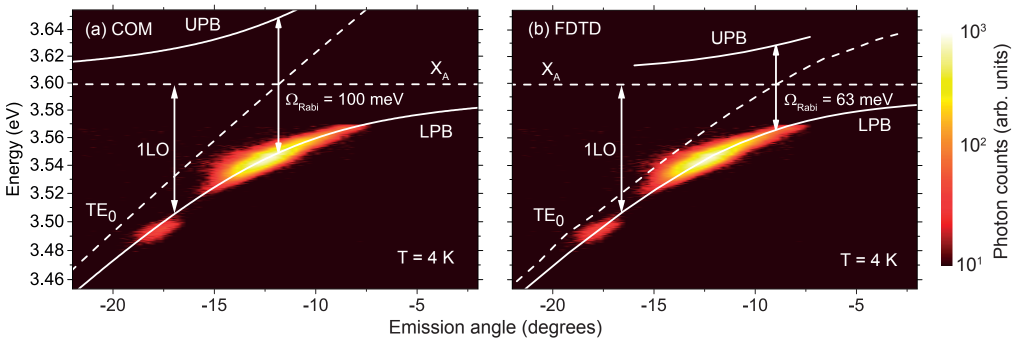

Figure 4.9 – Measured polariton dispersion for a propagation distance of 55 μm measured at $T = 4$ K with an excitation power density of 640 W/cm^2. The background signal from the bare excitons was subtracted for clarity. (a) A conventional COM is fitted to the data and the resulting UPB and LPB are shown in white, together with the uncoupled exciton (X_A) and the TE$_0$ mode. This model leads to a normal mode splitting of 100 meV. (b) Full 2D-FDTD mode calculations were performed for various values of the exciton oscillator strength. A good correspondence with the measurement was found for $f_X = 1.1 \pm 0.05 \times 10^{13}$ cm^{-2} (shown in white). We find a normal mode splitting of 63 meV using this method. The same experimental data are shown in both (a) and (b).

did not observe any spectral signature in the polariton dispersion data that could be related to the X_B exciton, such as the presence of a middle polariton branch. We therefore fully neglected X_B in the analysis and the modeling of the dispersion curves.

Figure 4.9 shows the same measurement as shown in Fig. 4.8(a), where the spurious PL signal coming from bare excitons was removed for clarity. We compared the measured signal at 4 K to both a simple coupled oscillator model (explained in Section 2.3.2) and full 2D FDTD calculations (cf. Appendix A). The COM uses a constant value of n_{eff}, and therefore a linear dispersion for the uncoupled TE$_0$ waveguide mode. By fitting this model (the results are shown in Fig. 4.9(a)), we find a normal mode splitting of 100 meV for this measurement. Application of Eq. 2.12 results in an oscillator strength of 3.0×10^{13} cm^{-2} for the QW excitons. The 2D-FDTD calculations on the other hand take the material refractive index dispersion into account. The resulting uncoupled TE$_0$ mode is curved due to the increase in refractive index of the QWs and barriers near the band edge, located at 3.64 and 3.71 eV, respectively, as shown in Fig. 4.9(b). The 2D-FDTD calculations were performed for various values of f_X, and a good fit to the data was found for $f_X = 1.10 \pm 0.05 \times 10^{13}$ cm^{-2}. The corresponding normal mode splitting is 63 meV. The discrepancy in the obtained values of f_X and Ω_{Rabi} between the COM and the 2D-FDTD calculations is mainly due to the neglected refractive index dispersion in the former case. Since the uncoupled mode is bent in the same direction as the anticrossing by the increasing refractive index toward the band edge, a smaller oscillator strength is required to reproduce the measured dispersion. A COM featuring a constant effective refractive index therefore systematically overestimates the exciton oscillator strength and the normal mode splitting. This comparison shows the importance of the effect of the refractive index dispersion in the analysis of photonic structures operating near the band edge of a semiconductor. Note

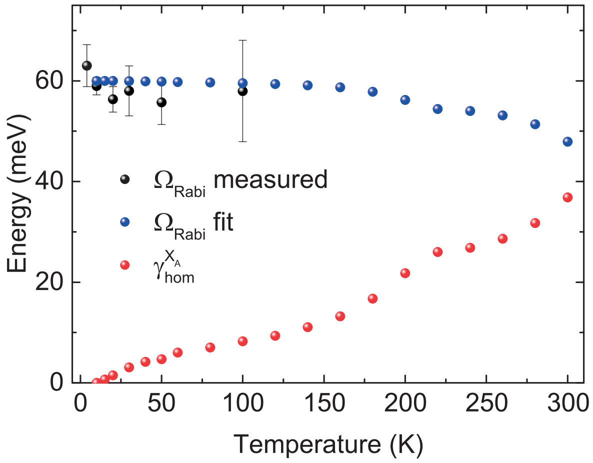

Figure 4.10 – Temperature dependence of Ω_{Rabi}. Measured values (black dots) and extrapolation up to room temperature (blue dots) obtained from Eq. 2.19, calculated using the homogeneous X_A exciton linewidth obtained from the measurements shown in Fig. 3.7(a) (red dots).

that a value of $f_X = 2.1 \times 10^{13}$ cm^{-2} was previously reported for similar QWs embedded in a strongly coupled MC using transfer matrix simulations accounting for dispersion [110]. Let us stress that the observed curvature in the dispersion cannot be explained by the increase in the refractive index of the active region near the band gap as can be seen in Fig. 4.9(b), which confirms that the present structure is operating in the SCR.

The signal intensity from the highly excitonic tail of the LPB is negligible in all measurements, most likely because polaritons rapidly relax to lower energy states and because the outcoupling rate is proportional to their photon fraction. The photonic tail of the LPB is hardly visible in the measured polariton dispersions, likely due to the relaxation bottleneck of highly photonic polaritons [172]. As the polaritons become more photonic, they loose the ability to relax through interaction with acoustic phonons. Note that there is a second maximum in the polariton emission intensity at ~92 meV below the localized X_A emission energy. This could be explained by the LO-phonon assisted relaxation of excitons to the LPB as already reported in the planar MC case [174, 175, 176].

By comparison with 2D-FDTD calculations, we find a normal mode splitting of 63 meV for the curve measured at 4 K (Fig. 4.9(b)) and an average splitting of 60 meV between 4 and 100 K. Such a value has to be compared to the 56-60 meV reported by Christmann *et al.* for a III-nitride planar MC containing 67 GaN/AlGaN QWs [18]. The similar value of Ω_{Rabi} recorded for the two geometries is the direct manifestation of the increased overlap between the guided mode and the active region, as represented by the $\frac{N_{QW}^{eff}}{L_{eff}}$ value. We can compare the present values of the normal mode splitting to the reported values of 5-6 meV in the case of a single QW GaAs-based polariton waveguide [144] and 290 meV in the case of excitons in organic semiconductors coupled to Bloch surface waves [148]. The difference between these values is essentially coming from the difference in f_X between the different material systems.

We did not observe any renormalization effects, i.e., any decrease in the normal mode splitting, with increasing pumping power up to 6 kW/cm^2. This is because we cannot measure any dispersion relation for propagation distances shorter than ~20 μm, as explained before. Therefore, we essentially probed regions where the reduction in the polariton density coming from their radial outspread is significant and renormalization should not be expected [143, 162].

Even though we were not able to measure the polariton dispersion up to room temperature, additional information on the temperature dependence of the SCR can be obtained by considering Eq. 2.19, namely $\Omega_{Rabi} = \sqrt{4g_0^2 - (\gamma_X - \gamma_{ph})^2}$.

We assume the photonic linewidth γ_{ph} to be temperature-independent. The homogeneous excitonic linewidth of the X_A exciton, $\gamma_{hom}^{X_A}(T)$, was extracted by fitting a Voigt peak profile (which is illustrated in Fig. 3.6(b)) to the temperature-dependent PL data shown in Fig. 3.7(a). Note that we only take the homogeneous broadening into account, since the normal mode splitting does not depend on the inhomogeneous broadening when $\gamma_{inh} < g_0$ [110, 134, 177]. The calculated values of $\Omega_{Rabi}(T)$ are shown in Fig. 4.10, together with $\gamma_{hom}^{X_A}(T)$. Based on these calculations, we can predict a slight decrease in the normal mode splitting down to 48 meV at 300 K. This again confirms the strong potential of the present platform to investigate the SCR up to room temperature.

4.4 Propagating Polariton Properties

Since the present slab waveguide is radially symmetric, waveguide polaritons will propagate isotropically from the excitation spot. Therefore, only polaritons within the angle covered by the collection zone can contribute to the signal and its intensity will approximately decrease as the reciprocal of the propagation distance r. This approximation holds well if the size of the collection region is substantially smaller than the propagation distance. Here, the collection region is 19 μm and the propagation distances used in the experiments range between 30 and 200 μm. This outspread is illustrated in Fig. 4.11.

In addition to this geometric reduction in polariton signal intensity with propagation distance, polariton decay will also reduce the amount of outcoupled photons with propagation distance. Indeed, as waveguide polaritons propagate, they experience an intrinsic decay following an exponential Beer-Lambert law, mainly due to photonic losses for the present exciton-photon de-

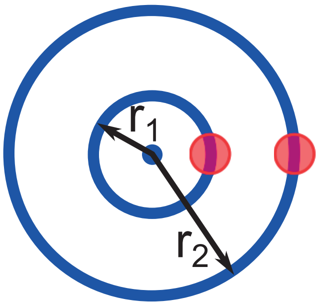

Figure 4.11 – Sketch of the collection for two different propagation distances, r_1 and r_2. Polaritons (blue) are created at the excitation spot and propagate isotropically in the waveguide plane. The red circles represent the collection areas. A smaller fraction of polaritons is captured with increasing propagation distance.

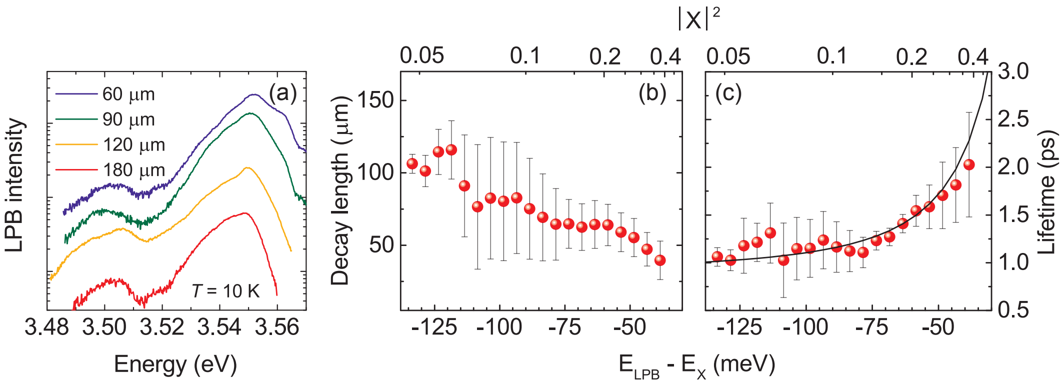

Figure 4.12 – Low temperature decay of waveguide polaritons. (a) Measured intensity of the LPB for different propagation distances at 10 K and for an excitation power density of 1.2 kW/cm^2. The spectra are not vertically shifted. (b) Polariton decay length as a function of polariton energy. (c) Lifetime of the guided polaritons. Measured data (red dots) and fit to Eq. 4.1 (black line). The mean value and error bars in (b,c) were deduced from a set of several measurements taken between 4 and 30 K. No substantial difference in the lifetime and the decay length was observed within this temperature range. The top axis in (b,c) represents the excitonic fraction of polaritons at the corresponding LPB energy.

tunings (δ) between -25 and -150 meV. The reduction in LPB signal intensity is illustrated in Fig. 4.12(a). In order to determine their intrinsic decay length – defined as the distance over which the integrated polariton PL intensity at the excitation spot is reduced by a factor e – and hence their lifetime, the measured integrated PL intensity is multiplied by the propagation distance –to cancel out the $\frac{1}{r}$ from the geometric outspread–, and this product is fitted to an exponential decay. The obtained decay length as a function of polariton energy is shown in Fig. 4.12(b). Polaritons with a large photonic fraction in excess of 0.94 are characterized by a decay length larger than 100 μm, which decreases as the excitonic fraction becomes larger. Consequently, the LPB emission redshifts with increasing propagation distance, as can be seen in Fig. 4.12(a), since the high-energy polaritons propagate less. To further support this analysis, the absorption coefficient in the waveguide was determined by the variable stripe length (VSL) method to be 60 cm^{-1} at around 200 meV below the free X$_A$ energy, as shown in Fig. 4.13. This value of the absorption coefficient corresponds to a decay length of 167 μm. This puts an upper limit to the propagation length of photons and highly photonic polaritons in the present sample and is mainly limited by residual absorption from the QWs. We can expect the absorption to be higher —and the corresponding decay length lower— for higher energies. Since the value of 167 μm only slightly exceeds the measured polariton decay lengths at energies between 120 and 140 meV below X$_A$, absorption is most likely the limiting factor of polariton propagation. The absorption losses could be reduced by increasing the Al content in the QW barriers, thus shifting the band-edge up.

Another essential figure of merit to qualify the present structure is the polariton lifetime $\tau_{pol}(\beta)$. The inverse of the latter is determined as the weighted average of the inverse lifetimes of the

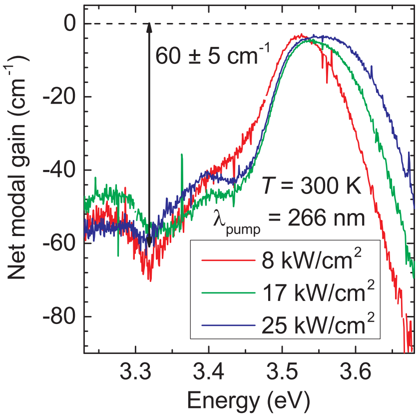

Figure 4.13 – VSL measurements of the present waveguide leading to an intrinsic absorption of 60 cm^{-1} below the gain band. We observe a broadening on the high-energy side of the gain band with increasing pump power due to band filling in the QWs. Note that the peak net modal gain does not increase with pump power. This is likely a consequence of the inhomogeneous pumping profile that results from absorption of the 266 nm pump laser in the barriers. This leads to a low carrier density in the bottom QWs.

photon (τ_{ph}) and the exciton (τ_X), and is given by

$$\frac{1}{\tau_{pol}(\beta)} = \frac{|P(\beta)|^2}{\tau_{ph}} + \frac{|X(\beta)|^2}{\tau_X}, \tag{4.1}$$

where P and X are the Hopfield coefficients, as defined in Section 2.3.2 [96]. The polariton lifetime $\tau_{pol}(\beta)$ was determined by dividing the measured polariton decay length by the group velocity of the LPB, defined as $\frac{\partial\omega}{\partial\beta}$, and is shown in Fig. 4.12(c). Values ranging between 1 and 2 ps were derived for polaritons with an exciton fraction between 0.05 and 0.4. The radiative free X_A lifetime was determined by time-resolved PL to be 325 ps at $T = 15$ K (cf. Section 3.3.3). A fit from Eq. 4.1 to the data leads to a value of 0.9 ps for τ_{ph}, which corresponds to a photonic linewidth $\gamma_{ph} = 0.73$ meV and an optical quality factor of 4.9×10^3. This photonic lifetime is about a factor of 5 larger than that reported for comparable III-nitride planar MCs [178]. This is essentially due to the improved photon confinement provided by TIR.

Note that we do not directly observe the photonic and excitonic linewidths stated above in the measured dispersion signal for highly photonic and excitonic polaritons, respectively. In addition to this broadening along the energy axis, there is indeed an extra source of broadening in the emission angle due to fabrication inhomogeneities in the grating coupler. For highly photonic polaritons, the energy linewidth becomes relatively small and the observed signal broadening is of purely angular origin. In this limit, we observe an angular FWHM $\Delta\alpha$ of 1.2°, which corresponds to a FWHM wavevector linewidth $\Delta\beta$ of 0.34 μm^{-1} and a FWHM error on the grating period $\Delta\Lambda = 0.8$ nm through Eq. 2.11.

The normal mode splitting of 60 meV corresponds to a Rabi period, i.e., the period of the coherent oscillations between the photon and exciton fraction of the polariton, as short as 69 fs. We find a Rabi period that is over an order of magnitude shorter than the polariton lifetime. As explained in Section 2.3, it is a key requirement for the SCR to have Rabi oscillations that are faster

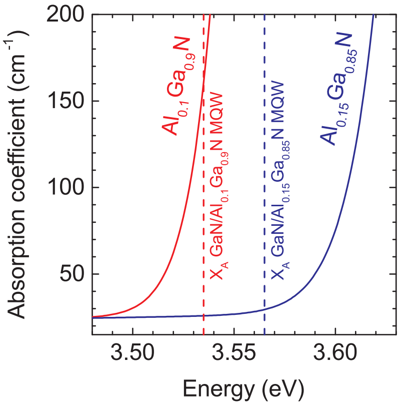

Figure 4.14 – Room temperature absorption coefficient of $Al_{0.1}Ga_{0.9}N$ and $Al_{0.15}Ga_{0.85}N$ epilayers, based on [82]. The X_A energy of GaN/AlGaN MQWs with a well thickness of 1.5 nm and a barrier thickness of 3.5 nm, containing 10 and 15% Al in the barriers is shown for reference.

than the polariton lifetime. When comparing the present values to those obtained in GaAs-based waveguides, where decay lengths up to 400 μm and lifetimes between 9 and 11 ps were demonstrated [144], the shorter decay lengths and lifetimes in III-nitride structures are likely due to the combination of an enhanced sensitivity to photonic disorder in short wavelength systems, together with the increased QW absorption below the band gap and the high number of QWs. If we compare the obtained values for the decay length to the ballistic condensate propagation on the order of 10 μm reported by Hahe *et al.* in a ZnO planar MC [179], the much larger decay length in the present case can be well accounted for by TIR confinement and the larger polariton propagation velocity, which ranges between 3 and 4×10^7 m/s in the present case.

A possible pathway to reducing the absorption losses occurring in the waveguide could be an increase in the Al content of the QW barriers. This would move the barrier band edge to higher energy and reduce the polariton absorption. Increasing the Al content to 15% would blueshift the AlGaN band edge by ~110 meV, while blueshifting the QW X_A energy by ~30 meV for the present geometry. The resulting reduction in absorption coefficient at the LPB energy (25 to 150 meV below X_A for the measurements shown in this chapter) is shown in Fig. 4.14. Increasing the Al content in the barriers would also increase the exciton binding energy (from 40 meV for 10% to 44 meV for 15%, cf. Section 3.2) and increase the inhomogeneous broadening (from 8 meV for 10% to 10 meV for 15%, cf. Fig. 3.7). Note that an inhomogeneous broadening of 10 meV would still have a negligible effect on the normal mode splitting, since the former is smaller than $g_0 = 30$ meV [110].

5 Optical Gain in GaN/AlGaN MQWs

In this Chapter, we investigate the optical gain properties of sample S3 presented in Chapter 3. The gain-specific features of the sample under investigation are discussed in Section 5.1. The gain experiments and modeling will be illustrated in Section 5.2. Details about the experimental techniques used in this chapter can be found in Appendix B. Most of the results presented in this chapter were published in the following paper:

- J. Ciers, G. Jacopin, G. Callsen, C. Bougerol, J.-F. Carlin, R. Butté and N. Grandjean, *Near-UV Narrow Bandwidth Optical Gain in Lattice-Matched III-Nitride Waveguides*, Jpn. J. Appl. Phys. **57**, 090305 (2018).

5.1 Sample Structure and Pumping

Compared to a single QW structure, a MQW structure has more electronic states available over an equal spectral range. As a result, a MQW structure exhibits an increased optical gain over a narrow band. In a single QW structure, the band filling required to reach elevated gain also causes a broadening of the gain band. However, a key requirement to achieve high optical gain in MQW structures is the homogeneous pumping across the QWs. As explained in Sections 2.4 and 3.1, absorption will be the dominating process in insufficiently pumped QWs, reducing the overall gain. For this reason, it is important to use optical pumping in the QWs, with an excitation energy below the barrier band edge. This is illustrated in Fig. 5.1 for the present sample. A 325 nm pump, which is above the $Al_{0.1}Ga_{0.9}N$ band edge, has an absorption thickness[1] of ~100 nm. A 355 nm pump on the other hand, which is situated between the QW and barrier band edge, is only absorbed in the QWs. Considering Eq 1.32:

$$\alpha_{2D}(\lambda_0) = \frac{\pi e^2 E_P m_r}{3\lambda_0 n_r \varepsilon_0 E_g^2 d_{QW} m_0},$$

we find that every QW absorbs $\alpha_{2D} d_{QW} \approx 1\%$ of the incoming power. This results in a very homogeneous pumping of the QWs. For this reason, sample S3 was designed with wide

---

[1] We define the absorption thickness as the distance over which the intensity is reduced by a factor e, Euler's number. With this definition, the absorption thickness is the inverse of the absorption coefficient, such that an $\alpha = 10^5$ cm^{-1} leads to an absorption thickness of ~100 nm.

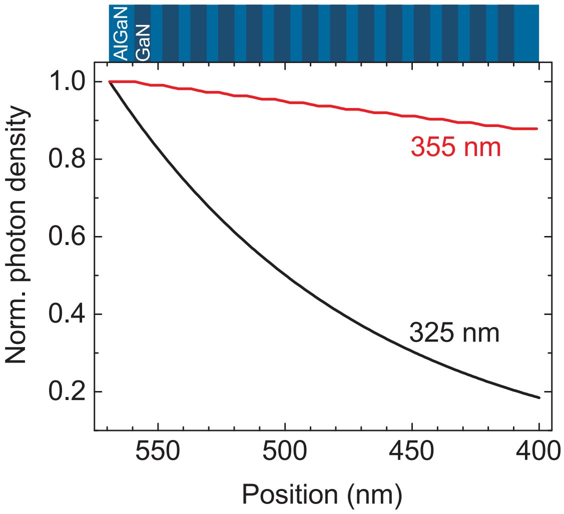

Figure 5.1 – Photon absorption in the MQW region for both a 325 nm (black) and a 355 nm (red) laser. A value of 1×10^5 cm^{-1} is taken for the absorption coefficient in the GaN QWs and AlGaN barriers at 325 nm [82]. At 355 nm, values of 1.54×10^4 cm^{-1} (cf. Eq. 1.32) and 50 cm^{-1} [82], are considered, respectively. These profiles are valid at photon densities for which no absorption saturation is at play. The position is determined with respect to the GaN buffer/AlInN bottom cladding layer interface.

GaN/$Al_{0.1}Ga_{0.9}N$ QWs of 6.2 nm width, such that they could be pumped below the barrier band edge with the available 355 nm laser.

Note that if the requirement of optical pumping with a 355 nm laser is relaxed, either through electrical injection or optical pumping with a different wavelength, the emission wavelength of this type of structures could be easily tuned toward the 350 nm spectral range by decreasing the QW thickness, i.e. approaching the MQW structure of sample S1, without any loss in material quality. The smaller weight of the QCSE and hence the larger overlap between electron and hole wavefunctions in thinner QWs could lead to reduced transparency and lasing thresholds in samples with thinner QWs. The internal losses will however also increase with increasing energy.

5.2 Gain Experiments and Modeling

The net modal gain g_{mod} was measured at room temperature by means of the VSL method, which is explained in Section B.2.5, using a Q-switched frequency-tripled Neodymium-doped yttrium aluminum garnet (Nd:YAG) 355 nm pump laser emitting 520 ps long pulses with a repetition rate of 8.7 kHz. Examples of PL emission spectra that were collected during these experiments are shown in Fig. 5.2(a) for 400 and 800 μm stripe length. On the high-energy flank of the emission, the intensities for both stripe lengths are nearly equal. This means that from the additional 400 μm pumped stripe, no extra photons are collected, implying that the absorption is large for these wavelengths. On the low energy flank of the emission, the 800 μm stripe has a higher intensity, leading to net modal gain values in the [-100 cm^{-1}, +100 cm^{-1}] range, as shown in 5.2(b). We observe that the peak modal gain increases with increasing pump power, up to ~80 cm^{-1}.

The results were fitted to Eq. 2.31, using the fully fermionic model, where we consider only an electron-hole plasma, without any excitonic effects, that was explained in Section 2.4, and has

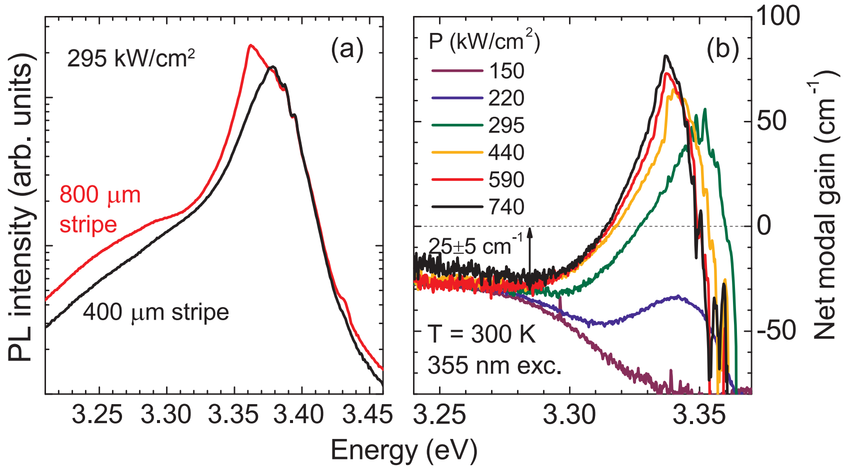

Figure 5.2 – VSL measurements performed on sample S3. (a) Raw PL emission intensity as measured in the VSL geometry from the facet for a stripe length of 400 μm (black line) and 800 μm (red line). (b) Net modal gain values determined by VSL for different power densities, as explained in Section B.2.5.

shown to accurately describe similar structures [124]:

$$g_{mod}(\hbar\omega) = -\alpha_{wg} + \sum_i \Gamma_i g_{mat,i}, \tag{5.1}$$

where the material gain can be calculated as

$$g_{mat} = \sum_{j=A,B} \alpha^j_{2D}(f^j_c(\hbar\omega) - f^j_v(\hbar\omega))\theta(\hbar\omega - E^j_{tr}). \tag{5.2}$$

Equation 5.2 is illustrated in Fig. 5.3 for a carrier density of 3×10^{12} cm^{-2}. This model takes both the A and B hole subbands into account, which is required to accurately model such structures [124]. We implemented the impact of the progressive screening of the built-in field on the transition energy through self-consistent Schrödinger-Poisson-$k \cdot p$ calculations [97], the results of which are shown in Fig. 5.4. A redshift in the QW transition energy due to band gap renormalization was implemented through Eq. 1.36. Taking these contributions into account, the QW transition energy becomes

$$E^j_{tr}(N) = E^j_{tr,0} + \Delta E_{QCSE}(N) - \Delta E_{BGR}(N) \text{ with } j = A, B, \tag{5.3}$$

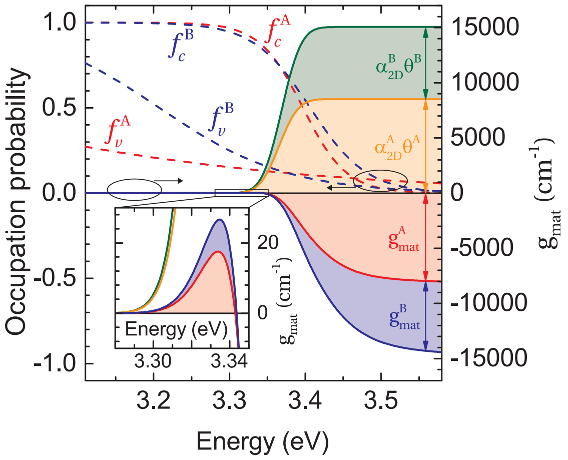

Figure 5.3 – Material gain per QW of the present structure, calculated as $g_{mat} = \sum_{j=A,B} \alpha_{2D}^j (f_c^j(\hbar\omega) - f_v^j(\hbar\omega))\theta(\hbar\omega - E_{tr}^j)$, for a carrier density of 3×10^{12} cm^{-2}. The differences in the slopes of the Fermi-Dirac distributions are a consequence of the differences in effective masses of the different particles, while the differences in quasi-Fermi energy and transition energy leads to the different positions. The inset shows a zoom on the gain band, where the Bernard-Duraffourg condition [125] is fulfilled, resulting in a positive material gain.

where $E_{tr,0}^j$ is the transition energy measured at low carrier density, $\Delta E_{QCSE}(N)$ is the energy shift due to progressive screening of the built-in field with increasing carrier density and $\Delta E_{BGR}(N)$ is the energy shift due to band gap renormalization. The carrier density in each QW was estimated from the incoming photon density I including a Lorentzian saturation curve for the QW absorption [180]:

$$\alpha_{2D,sat} = \frac{\alpha_{2D}^A + \alpha_{2D}^B}{1 + I/I_{sat}}. \tag{5.4}$$

Using an ad hoc saturation photon density $I_{sat} = 2.7 \times 10^{14}$ photons/cm^2 = 300 kW/cm^2, we could consistently fit all experimental data. The numerical values of all parameters used for the modeling are given in Table 5.1.

Given the specificity of the structure, which is composed of QWs emitting at slightly different energies –as explained in Section 3.2– and subjected to different carrier densities, quantitative modeling of the modal gain seems rather challenging. However, the high structural and optical quality of the sample, which was illustrated in Chapter 3, allows for a precise determination of its properties in the low-density regime, hence minimizing the number of unknown parameters. Note, however, that for the sake of simplicity, we did not include any LO-phonon contribution [181] or collisional broadening [124] to the modeling of the gain spectra. Since these phenomena both broaden the gain band, an increased value by a factor of ~2 of γ_{inh} is required in the model to obtain good fits, i.e., a value of 20 meV compared to 11 meV as determined through PLE experiments.

The obtained gain spectra are shown in Fig. 5.5(a), together with the fits. The resulting fitting parameters –carrier density and low-density transition energy– are given in Figs. 5.5(b) and 5.5(c). Experimentally, we observe a fast increase in g_{mod} for pump power densities ranging

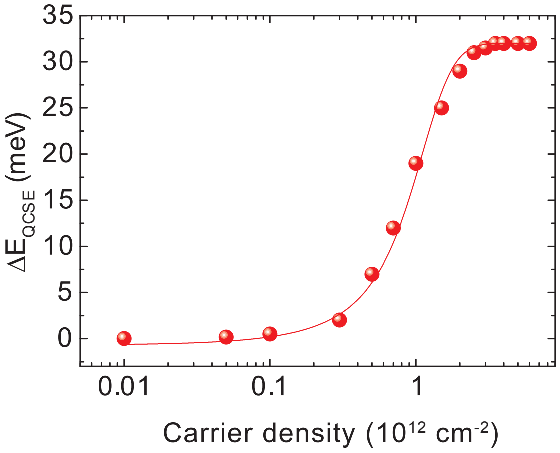

Figure 5.4 – Calculated energy shift experienced by the QW ground state transition due to screening of the built-in field with increasing carrier density as calculated by means of a self-consistent Schrödinger-Poisson-$k \cdot p$ solver (symbols) [97, 119]. The red line serves as a guide to the eye.

from 220 to 295 kW/cm^2. This is ascribed to the large number of QWs and the high Γ value, which results in a large increase in g_{mod} for a moderate increase in material gain of each individual QW. When the pump power density is further increased, the peak modal gain value and the average carrier density exhibit a saturation-like behavior with a peak g_{mod} value of ~80 cm^{-1}. This is likely originating from the limited pump absorption by the QWs due to efficient band filling. From the absorption saturation term included in the model, we deduce a saturation photon density of 2.7×10^{14} photons/cm^2 = 300 kW/cm^2 with the 355 nm pump laser. A residual waveguide absorption loss of 25 ± 5 cm^{-1} is deduced from the g_{mod} spectra, as illustrated in Fig. 5.5(a). This value can be explained by looking at the overlap of the optical field intensity $\varepsilon|E|^2$ of the TE$_0$ mode as shown in Fig. 3.2(c) with the active region and cladding layers, which amount to 89.7 and 10.3%, respectively. Since the absorption in these AlInN layers is typically ranging between 80 and 100 cm^{-1} at these wavelengths [68], a residual absorption coefficient between 16 and 19 cm^{-1} in the waveguide region can account for the present overall absorption of 25 cm^{-1}. Note that a residual waveguide absorption of 35 cm^{-1} was reported for commercial InGaN/GaN-QW-based laser diode samples operating at 375 nm [153]. The obtained fits do not describe the experimental results adequately on the low-energy flank for low pumping fluences. This is likely a consequence of the omitted LO-phonon contribution, which causes a broadening on the low-energy side of the gain spectra [181].

We also observe a redshift of the gain band with increasing pump power. This is opposite to the commonly observed blueshift in such experiments, which is mainly a consequence of band filling [157, 182, 183]. This spectral shift can be accounted for by considering two of the phenomena at play, namely band filling and the shift of the transition energy E_{tr} with increasing carrier density N. The latter is described by Eq. 5.3.

Let us briefly discuss the contributions of the different phenomena. Band filling will cause a blueshift of the emission with increasing carrier density, which is mainly dependent on the γ_{inh} value of the MQWs. Indeed, systems characterized with a large γ_{inh}, such as InGaN/GaN QWs emitting in the visible or near UV [157, 183] or AlGaN/Al(Ga)N QWs emitting in the deep UV [182] will experience a much larger blueshift than a system with low inhomogeneity such as the

Table 5.1 – Parameters used for the Schrödinger-Poisson-$k \cdot p$ and the gain calculations. The effective masses for the $Al_{0.1}Ga_{0.9}N$ barriers are derived from a linear interpolation between GaN and AlN values.

Parameter	Value	Source
Effective electron mass in GaN $m_{e,GaN}$	$0.2m_0$	Ref. [90]
Effective A hole mass in GaN $m_{A,GaN}$	$1.8m_0$	Ref. [90]
Effective B hole mass in GaN $m_{B,GaN}$	$0.45m_0$	Ref. [90]
Effective electron mass in AlN $m_{e,AlN}$	$0.32m_0$	Ref. [90]
Effective A hole mass in AlN $m_{A,AlN}$	$3.1m_0$	Ref. [90]
GaN layer thickness	6.2 nm	HRTEM and XRD
$Al_{0.1}Ga_{0.9}N$ layer thickness	4.8 nm	HRTEM and XRD
Internal absorption in the waveguide α_{wg}	25 cm^{-1}	VSL measurements
Exciton binding energy E_B	19 meV	$k \cdot p$
Exciton Bohr radius a_B	5 nm	$k \cdot p$
Kane energy E_P	17.3 eV	Ref. [90]
QW absorption for the A transition α_{2D}^{A} (355 nm)	8.7×10^3 cm^{-1}	Eq. 1.32
QW absorption for the B transition α_{2D}^{B} (355 nm)	6.7×10^3 cm^{-1}	Eq. 1.32
QW refractive index n_r (355 nm)	2.7	Ref. [82]
Inhomogeneous broadening γ_{inh}	20 meV	Input parameter

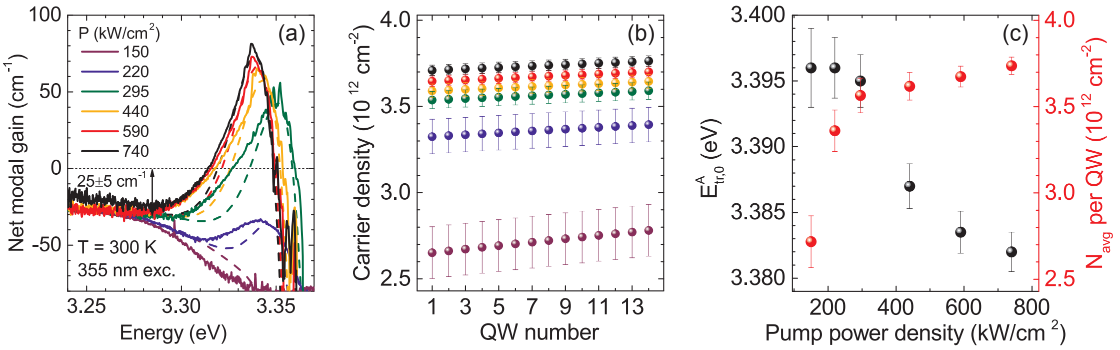

Figure 5.5 – Experimental net modal gain spectra and fit parameters used to fit the data. (a) Net modal gain (continuous lines) measured at RT for the present sample using the VSL method. Fits relying on a Schrödinger-Poisson-$k \cdot p$ formalism (dashed lines) show a good quantitative agreement with experiments. (b) Calculated carrier densities corresponding to the fits shown in (a). (c) Parameters extracted from the modeling: low carrier density transition energy (black dots) and average carrier density (red dots). The error bars in (b) and (c) represent the standard error resulting from the fit procedure.

present MQW structure. Band filling is well accounted for in the model through the Fermi-Dirac distributions. [124].

QWs subjected to a built-in field will experience the usual blueshift observed with increasing carrier density, as illustrated in Fig. 5.4. Band gap renormalization arises from interparticle interactions and causes a redshift that is accounted for by Eq. 1.36:

$$\Delta E_{BGR}(N) = 3.1 a_B^{2/3} E_B N^{1/3}.$$

E_0^A was kept as a fitting parameter in the model (E_0^B was fixed at $E_0^A + 9$ meV, corresponding to the PLE measurements of Fig. 3.6) whose value as a function of power density is shown in Fig. 5.5(c). We notice a redshift of E_0^A of ~14 meV, which is comparable to the MQW energy spread deduced from the calculations and CL measurements shown in Fig. 3.5(d). This indicates that the lower-energy QWs have an increasing relative weight in the g_{mod} spectra with increasing pump power, which is consistent with the carrier densities shown in Fig. 5.5(b). Due to the larger saturation experienced by the higher energy top QWs, the lower emitting bottom ones will be relatively more populated at higher pump power, hence explaining the overall redshift of the gain band. An overall saturation of the pump laser absorption can be observed through the saturation of the average carrier density in Fig. 5.5(c), as the pump power density goes beyond the saturation power density $I_{sat} = 300\ \mathrm{kW/cm^2}$.

In addition to the narrow gain band and high gain values, the moderate shift of the gain band reported here could prove useful for the realization of devices where the output power needs to be varied with minimal changes in the output wavelength such as SOAs or LDs.

6 Conclusion and Outlook

6.1 Summary of the Results

During this thesis work, we have studied light-matter interaction in *c*-plane III-nitride waveguides grown by MOVPE on low threading dislocation density (10^6 cm^{-2}) freestanding GaN substrates. These waveguides feature GaN/AlGaN MQWs and AlInN cladding layers for optical confinement, which are nearly lattice-matched to GaN. The absence of lattice-mismatch leads to a high structural and optical quality, as evidenced by XRD and TEM measurements, and various spectroscopic techniques. The AlInN claddings provide a large RIC of 7-11% with $Al_{0.1}Ga_{0.9}N$ between 345 and 370 nm, the present wavelength range of interest. This contrast results in a small effective length of the TE_0 mode, of 88 and 99 nm, for waveguides with a thickness of 130 and 170 nm, operating at 345 and 370 nm, respectively. We found an inhomogeneous broadening as low as 8 meV over 22 GaN/$Al_{0.1}Ga_{0.9}N$ QWs with a thickness of 1.5 nm in PL and 11 meV over 14 GaN/$Al_{0.1}Ga_{0.9}N$ QWs with a thickness of 6.2 nm in PLE. Note that a large fraction of the latter value is due to a gradient in built-in electric field over the MQWs, and not due to structural disorder. This gradient is a consequence of a complex interplay between the spontaneous polarization mismatch between the claddings and the MQW region together with the residual doping in the active region. The high structural quality leads to a standard deviation of only 0.42 meV over a 50×50 μm^2 area in the X_A emission energy. We also observed biexciton emission from the 1.5 nm wells at higher PL power densities. A presentation of the samples, together with a detailed discussion of these results can be found in Chapter 3. We calculated the band structure and we determined the transition energies of the MQWs using self-consistent Schrödinger-Poisson $k \cdot p$ calculations and found a good agreement with experiments.

In Chapter 4, we described the properties of propagating polaritons, which arise from hybridization between GaN/AlGaN MQW excitons with the propagating TE_0 waveguide mode. The strong coupling regime was observed up to 100 K with an average normal mode splitting as high as 60 meV due to the large overlap between the QWs and the waveguide mode. Beyond 100 K, the signal intensity is reduced due to decreasing IQE of the active region and can no longer be measured. However, we expect the strong coupling regime to be maintained up to room temperature. The guided polaritons feature a decay length of 50 to 100 μm and a lifetime of 1-2 ps, which are well accounted for by residual absorption in the waveguide. Absorption losses could be reduced by increasing the Al content in the barriers.

Chapter 5 studies the properties of waveguides featuring 6.2 nm wide GaN/$Al_{0.1}Ga_{0.9}N$ MQWs

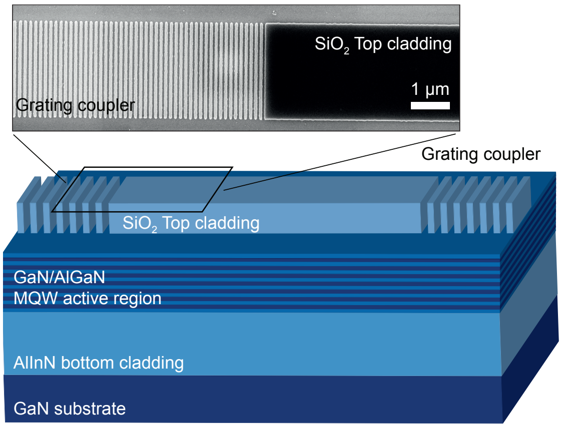

Figure 6.1 – (bottom) Sketch of a ridge polariton waveguide structure. Such a geometry would provide latteral confinement to the propagating polaritons and would be more appropriate for devices. (top) Top view SEM image of the fabricated structure.

above the Mott transition, where an electron-hole plasma in the MQWs generates optical gain. Thanks to the large RIC between the core and the cladding layers, a Γ value as large as 48% is achieved. Consequently, net modal gain values in excess of 80 cm^{-1} are measured, whose value is limited by absorption of the near-resonant pump laser. Due to the small disorder in the sample, the gain band is as narrow as 20 meV. It exhibits a small redshift with increasing pump power, which is a consequence of the gradient in built-in electric field over the QWs. The measured net modal gain spectra are successfully reproduced using a self-consistent Schrödinger-Poisson-$k \cdot p$ formalism.

6.2 Perspectives

The good optical and structural quality of these waveguides, together with the high light-matter coupling strength –which is illustrated by the large values of $\Omega_{Rabi} = 60$ meV and $g_{mod} = 80$ cm^{-1}– provides an ideal platform for light-matter coupling applications on both sides of the Mott transition.

In the excitonic regime, these structures show great potential for photonic and polaritonic integrated circuits up to room temperature. In this perspective, ridge waveguides, as sketched in Fig. 6.1, with lateral confinement would prove a more practical geometry for devices, as they would prevent the isotropic propagation of polaritons. Consequently, the signature of waveguide polaritons should be measurable over longer distances (on the order of ~500 μm) and up to nearly room temperature. They would also open the possibility to explore polariton nonlinearities using resonant excitation through a grating coupler, e.g. polariton soliton wavepackets [16], up to room temperature. For such measurements, metal grating couplers featuring a short coupling length on the order of ~20 μm, are crucial to efficiently couple light into the waveguide. Based on these nonlinearities, active all-optical devices such as optical logic gates or optical transistors [14, 15] could be developed, with potential applications in information processing, photonic integrated circuits or sensing [184].

Due to the large overlap between the optical mode and the QWs (we obtained a ratio $\frac{N_{QW}^{eff}}{L_{eff}} =$

0.166 QW nm^{-1}), which is a result of the excellent optical confinement by total internal reflection, the exciton-photon coupling g_0 is stronger than in III-nitride microcavities with a similar number of QWs. Therefore, the strong light-matter coupling regime might be achievable using InGaN/GaN QWs. In microcavities, this regime is challenging to achieve, since the large number of wells required results in excessive strain, relaxation and large inhomogeneous broadening [110, 185]. The high $\frac{N_{QW}^{eff}}{L_{eff}}$ ratio and small number of QWs required in a waveguide geometry could result in a situation where the inhomogeneous broadening is smaller than g_0, and strong coupling is achieved. The associated reduction in polariton energy has the additional benefit of easier p-type doping –opening the way to electrically injected polariton waveguides– and reduced absorption. A residual absorption of ~20 cm^{-1}, such as reported in ref. [153] for a 405 nm LD, would result in a decay length of ~500 μm and a lifetime of ~6 ps for highly photonic polaritons. Also for GaN/AlGaN QW-based waveguides, electrical injection is possible, in a similar way as for UV LDs [25], and a reduction in residual absorption might be achievable by increasing the barrier Al content, or by reducing the impurity levels during growth. Note that n- and p-doped AlInN layers have been demonstrated with a net donor concentration of 9×10^{18} cm^{-3} and a net acceptor concentration of 5.3×10^{18} cm^{-3}, respectively [33, 35]. In AlInN/GaN superlattices, such as the bottom claddings used here, net acceptor concentrations above 1×10^{19} cm^{-3} were reported [35]. The successful application of these layers as cladding material in a blue InGaN/GaN-based LD [35] shows that electrically injected waveguide structures operating in the strong light-matter coupling regime could be achieved.

Also for structures operating above the Mott transition, i.e. in the electron-hole plasma regime, the realization of electrically injected lattice-matched waveguides is within reach. This could lead to compact LDs or SOAs with low current threshold, elevated gain, narrow gain bandwidth, and reduced emission wavelength shift with increasing carrier density. Operation in the 350-370 nm wavelength range is achievable by implementing the QWs used in this work. Room temperature wavelengths below 350 nm could be reached by increasing the Al content in the barriers and eventually in the wells [25]. Also for these wavelengths, structures featuring AlInN claddings (optionally with In concentrations below 17%), could provide improved material quality and optical confinement in comparison to their AlGaN-based counterparts.

A Finite-Difference Time-Domain Calculations

A.1 What is FDTD?

In a finite-difference time-domain solver, solutions to Maxwell's equations are calculated numerically over a determined region in space and time. The starting point of the calculation are Faraday's and Ampère's law

$$\frac{\partial \mathbf{B}}{\partial t} = -\nabla \times \mathbf{E}, \tag{A.1}$$

$$\frac{\partial \mathbf{D}}{\partial t} = \nabla \times \mathbf{H} - \mathbf{J}, \tag{A.2}$$

where **E**, **H**, **D** and **B** are the electric and magnetic fields, the electric displacement and magnetic induction fields, respectively, and **J** is the electric current density [186]. In dielectric media, $\mathbf{J} = \mathbf{0}$. For linear nonmagnetic media, we can write $\mathbf{D} = \varepsilon_{rel}\varepsilon_0 \mathbf{E}$ and $\mathbf{B} = \mu_0 \mathbf{H}$, with μ_0 the vacuum permeability. By substituting this in Eq. A.1 and Eq. A.2, we get

$$\frac{\partial \mathbf{H}}{\partial t} = -\frac{1}{\mu_0} \nabla \times \mathbf{E}, \tag{A.3}$$

$$\frac{\partial \mathbf{E}}{\partial t} = \frac{1}{\varepsilon_{rel}\varepsilon_0} \nabla \times \mathbf{H}. \tag{A.4}$$

This gives us two equations that link the time derivative of the $\mathbf{E}(\mathbf{H})$-field to the spatial derivative of the $\mathbf{H}(\mathbf{E})$-field. This allows to calculate, e.g., the x-component of $\mathbf{E}(x, y, z)$ at time t_1 in a leapfrog manner from the x-component of $\mathbf{E}(x,y,z)$ at $t_1 - \Delta t$ and the derivative with respect to x of the **H**-field between $(x - \frac{\Delta x}{2}, y, z)$ and $(x + \frac{\Delta x}{2}, y, z)$ at $t_1 - \frac{\Delta t}{2}$. The other components of **E** and **H** can be calculated in an analogous way. Here Δx, Δy, Δz and Δt represent the discretization steps in space and time, respectively. This naturally leads to a staggered mesh, or Yee grid [187], where the values of the electric and magnetic fields are sampled at different points in space and time, offset by half of the discretization step. Doing so allows the time and space derivatives to be formulated as center-difference approximations. Further details can be found ,e.g., in ref. [188].

In order to reach numerical accuracy, at least 10 sampling points per wavelength are required [188]. Additionally, the spatial discretization steps along a certain direction should be substantially smaller than the smallest feature of the structure in that direction. In the structures studied in this work, the QWs are the smallest feature in the y-direction that will determine Δy. The time step is determined by the size of the spatial grid. Since electromagnetic waves propagate at the speed of light in the medium, $\frac{c}{n_{op}}$, the time step should correspond to the time required to cross the diagonal of a cell at this speed [188].

In typical time-domain calculations, all fields are zero over the entire region before $t = 0$. Then, source fields –usually a Gaussian pulse electric dipole source with a Gaussian envelope modulating a sinusoidal oscillation in the time domain and a Gaussian profile centered on the sinus frequency in the frequency domain– are added to one or more pixels at $t = 0$. The generated electromagnetic waves propagate through the structure for a certain simulated time, typically until all fields have died out.

Since computer memory and computation time are limited, the simulation region and simulated time must also be limited. Several options exist for the boundaries of the simulation region. Periodic or Bloch boundary conditions can be used in case of a periodic structure. Perfectly matched layers (PMLs) [188]–which are designed such that all incident radiation is absorbed and not reflected– could be used to simulate an isolated structure, where all electromagnetic waves eventually go to infinity.

In most cases, we are interested in the spectral behavior, rather than the temporal one, of the optical structure under investigation. This can be achieved by taking the Fourier transform of the recorded fields. Therefore, the source must cover the frequency range of interest.

A.2 Calculating Eigenmodes and Eigenfrequencies of a Resonator

To track the resonant modes of a cavity or waveguide using FDTD, the following procedure is used. A source, covering the frequency range of interest, is located in the resonator. The fields are left propagating in the structure for a sufficiently long time, until only the constructively interfering eigenfrequencies are left, and the other frequencies have died out. We observe a peak in the emitted power of the source in the frequency domain for the eigenfrequencies. This power is proportional to the local density of optical states (LDOS) in the waveguide [189] and the presence of a peak in the LDOS indicates a resonant mode. The spatial distribution of the fields at such an eigenfrequency corresponds to the eigenmode profile. One should be careful in positioning the source, as a source located at a node of the eigenmode, or with a polarization perpendicular to the eigenmode polarization will not couple to this mode. As such, the eigenmode will not appear in the simulation results.

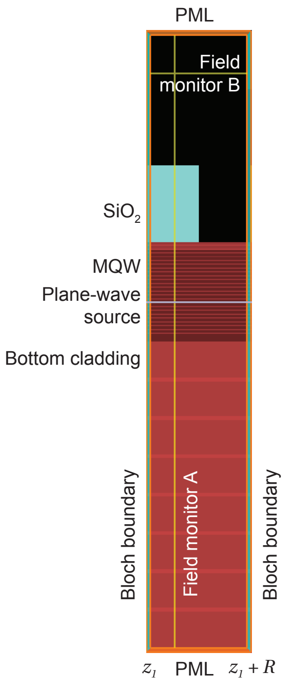

Figure A.1 – Simulation region for the FDTD dispersion calculations. One period of the grating coupler is included in the simulation, while the rest of the structure is added through the Bloch boundary conditions. Field monitor A records the guided mode profile of the eigenmodes, while the spatial Fourier transform of field monitor B gives the far-field emission angle of the outcoupled light.

In this case, we are interested in the dispersion of a 2D slab waveguide, i.e. the eigenfrequency as a function of the in-plane wavevector. To calculate this, we first calculate the eigenmodes and -frequencies for a single, well determined, in-plane wavevector β along z. For this reason, a plane wave source –which is essentially a collection of line sources in the xz-plane with a phase relation $\exp(i\beta z)$ between them– is used, which assures that all injected fields, and therefore the calculated eigenenergies, correspond to the correct β. When using a plane wave source, it is essential to use Bloch boundary conditions, which conserve the phase relation, in all directions which are not parallel to the source. In our case, we have a 2D simulation in the yz-plane (with y the sample growth direction and z the propagation direction of the guided modes), since the structure is supposed to be extended infinitely in the x-direction. The Bloch boundary condition for the z-direction then becomes in phasor notation

$$\mathbf{E}(y, z_1 + R) = \mathbf{E}(y, z_1)\exp(i\beta R) \text{ and } \mathbf{H}(y, z_1 + R) = \mathbf{H}(y, z_1)\exp(i\beta R), \tag{A.5}$$

where z_1 and $z_1 + R$ are the location of the left and right boundary, respectively.

In addition to the in-plane wavevector, the corresponding grating coupler emission angle can be calculated by integrating at least one period of the grating coupler in the simulation region, as illustrated in Fig. A.1. The far-field emission angle can be calculated from the spatial Fourier transform of the fields above the grating coupler. Repeating the calculation for different values of β results in the desired mode dispersion. This procedure is illustrated in Fig. A.2.

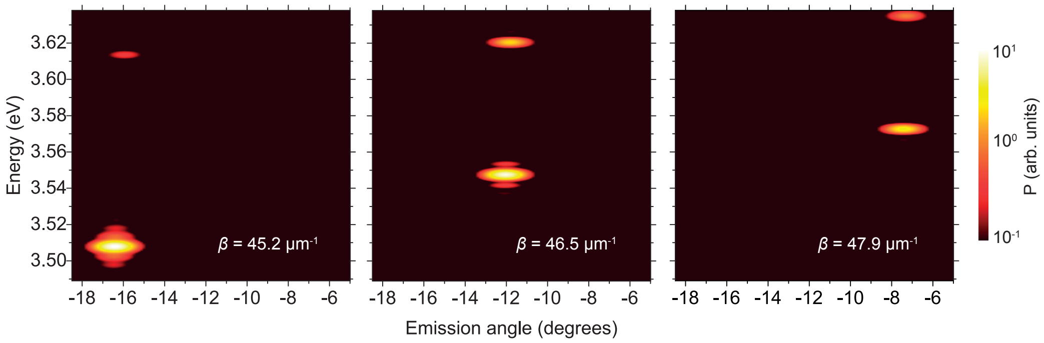

Figure A.2 – Illustration of the 2D-FDTD calculations of the waveguide mode dispersion. The emitted power P from the waveguide grating is calculated in the far field as a function of emission angle and energy for a broadband source with fixed in-plane wavevector β. The peak in emitted power corresponds to the guided mode spectral position. Calculations are repeated for different values of β to reproduce the modal dispersion.

These calculations were performed using Lumerical FDTD solutions [154]. We can determine the emission angle and energy of the guided mode corresponding to this particular in-plane wavevector from the peak position. Note that the peak in the LDOS disappears when approaching the exciton energy due to increasing absorption. We limited the spectral range of the calculation at the MQW band edge energy (3.64 eV) on the high-energy side in order to avoid problems related to the cusp shape in the MQW refractive index dispersion close to the band edge, which was illustrated in Section 1.2.6. Lumerical FDTD uses a Lorentz oscillator model for sampled refractive index data that does not fit very well to this type of features [190]. This limits the range where we can calculate the UPB. The parameters used to model the refractive index of the layers are summarized in Table A.1.

Table A.1 – Parameters used for the 2D-FDTD calculations at $T = 4$ K of sample S1.

Parameter	Value at 4 K	Comment
E_X(AlGaN)	3.683 eV	Deduced from PR measurements
E_B(AlGaN)	28.1 meV	Linear interpolation between bulk values of GaN (25 meV) [91] and AlN (56 meV) [92]
E_X(QW)	3.599 eV	Deduced from PR measurements
E_B(QW)	40 meV	ref. [101]
Γ_{inh}(QW)	8 meV	Deduced from PL measurements
Γ_{hom}(QW)	Negligible	

B Experimental Methods

This Appendix discusses the experimental techniques that were deployed in the framework of this PhD thesis. Section B.1 explains the methods used in the fabrication process of the grating couplers, while Section B.2 sheds light on the spectroscopic techniques applied for the characterization of the waveguides.

B.1 Nanofabrication

B.1.1 Plasma-Enhanced Chemical Vapor Deposition

Chemical vapor deposition (CVD) techniques rely on the reaction of chemicals in the gas phase to grow a film of the desired material. In traditional CVD techniques, such as MOCVD, described in Section 1.1.3, the chemical reaction energy is provided by maintaining the substrate at an elevated temperature. In plasma-enhanced CVD (PECVD), however, part of the reaction energy is provided by a radio-frequency (RF) plasma source, allowing a lower deposition temperature, down to 100°C in some cases. In this work, an Oxford Plasmalab System 100, which is sketched in Fig. B.1, was used for the deposition of amorphous SiO_2 films. It operates by injecting the precursor gases –a mixture of 98% N_2 and 2% SiH_4 as a Si precursor and N_2O as an O precursor– between two parallel electrodes. The bottom electrode carries the substrate, which is heated to 300°C, and is grounded, while the top one applies the RF voltage. A plasma is generated by the oscillating electric field with a power of 20 W, and the reactant species are excited. This allows the desired reaction to occur on the substrate, resulting in the deposition of the SiO_2 film with a rate of ~64 nm/min in this case. SiO_2 layers deposited with this technique have a very low absorption in the UV ($\sim 1\ \text{cm}^{-1}$ around 345 nm, as measured with a Cary 500 spectrophotometer). Besides SiO_2, PECVD is also commonly used for deposition of Si_3N_4, SiC and amorphous silicon.

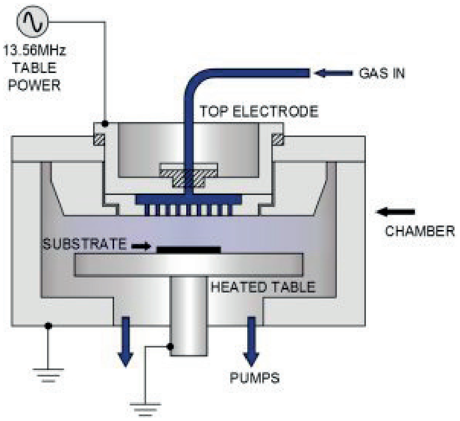

Figure B.1 – Sketch of the PECVD reactor. Reproduced from [191].

B.1.2 Electron Beam Lithography

In lithography, the sample is covered with a photosensitive, for optical lithography, or electrosensitive, for electron beam lithography, resist layer, which undergoes a chemical modification under exposure with light or electrons, respectively. After exposure, the sample is developped in a solution that removes only the exposed regions, for a positive resist, or only the non-exposed regions, for a negative resist. Subsequent etching techniques allow to transfer the created resist pattern to the layers underneath. After this step, the resist layer is typically no longer needed and is removed. Alternatively, in cases where etching is chemically not possible or practically difficult, the material to be patterned can be evaporated onto the patterned resist. The latter is subsequently removed with the evaporated material on top, while the material on the resist-free regions remains. This process is called lift-off.

The resolution and minimal feature size that can be obtained with this technique depends mainly on the wavelength λ of the radiation used, as described by the Rayleigh equation

$$l_{min} = \frac{c_1 \lambda}{\mathrm{NA}}, \tag{B.1}$$

where c_1 is a constant that accounts for the specific factors related to the resist, development, etc. of the process, and NA is the numerical aperture of the optical system. The shortest wavelength optical lithography systems that are commercially available are based on 193 nm ArF excimer lasers. Since the grating couplers we wish to fabricate for this work have a feature size of ~65 nm, this is not possible with optical lithography.

The relativistic de Broglie wavelength of an electron with kinetic energy E_k is given by

$$\lambda_e = \frac{hc}{pc} = \frac{hc}{\sqrt{E_k^2 + 2E_k m_0 c^2}}, \tag{B.2}$$

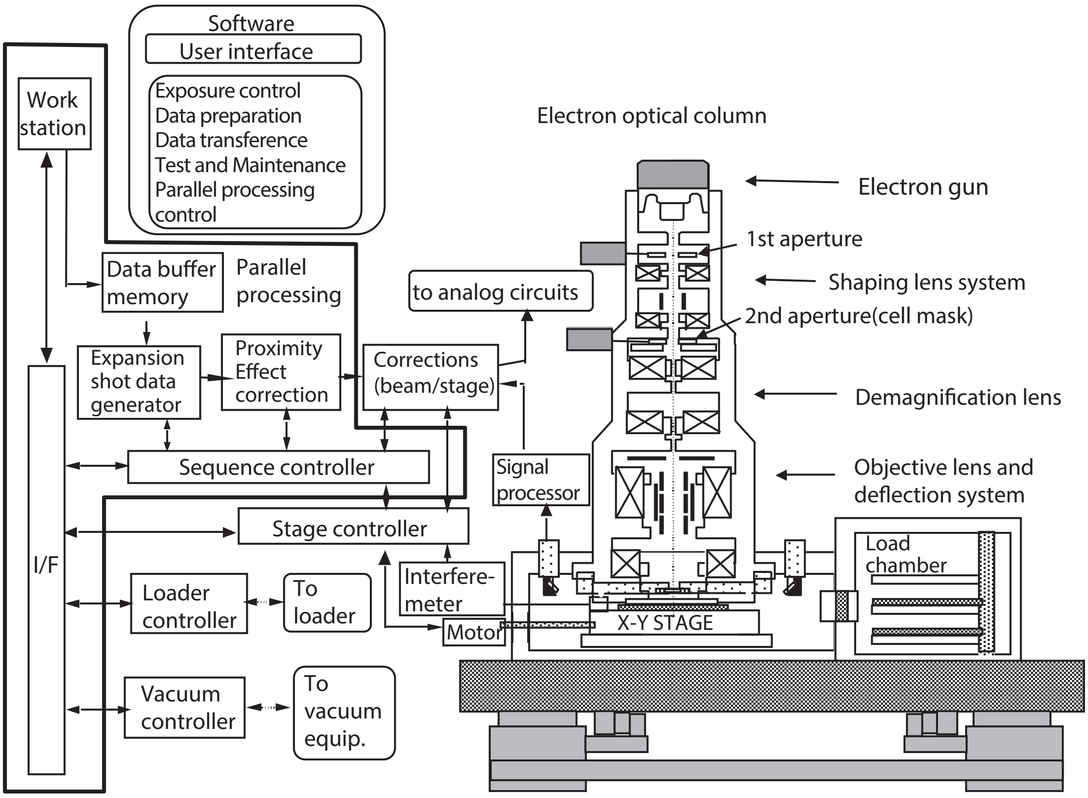

Figure B.2 – Schematic illustration of an electron beam lithography system. Reproduced from [192].

where h is Planck's constant, p is the electron momentum, and $m_0c^2 = 511$ keV is the electron rest mass. For a commonly used acceleration voltage of 100 kV, this results in $E_k = 100$ keV and $\lambda_e = 3.7$ pm. This very small value implies that a much higher resolution can be obtained with electron beam (e-beam) lithography compared to optical lithography. In practice, the resolution is not limited by diffraction, but by the quality of the objective lens, electron-electron repulsion in the focus point (which increases the spot size) at high current, and backscattered electrons from the substrate. These backscattered electrons are typically spread over a region with ~50 μm radius around the beam focus. This implies that the effective dose will depend on the distance to other features in the pattern. This phenomenon is known as proximity effect. In many cases, the exposure dose is corrected for this effect.

The first dedicated e-beam resists have been developed in the late 1960s[193]. The first electron beam exposure system, which was based on a modified SEM, was reported by Bell Laboratories in 1975 [194].

A typical e-beam exposure system is sketched in Fig. B.2. It consists of

- An electron column containing (from top to bottom): (i) an electron gun from which the electrons are emitted, (ii) an ensemble of electromagnetic coils, called lenses, that collimate the electron beam and an ensemble of apertures that control the current, (iii) a beam deflection system where a set of electromagnetic coils is used to deflect the electron beam over the sample to the area that needs to be exposed, and (iv) an ensemble of focusing and objective lenses to focus the beam on the sample. The whole column is under high vacuum ($< 10^{-8}$ mbar) to ensure a mean free path that is substantially longer than the column.

- A mechanical system, comprising of a stage, which moves the sample in the xy-plane, and a load lock chamber with loading arm.
- Control electronics to manage the entire system.
- A workstation with software to handle the pattern preparation, the conversion from a computer-aided design (CAD) file to a writing file readable by the machine, the control of the exposure procedure and the overall monitoring and maintenance of the e-beam equipment.

In this work we use a 100 kV Vistec EBPG5000 system at the center for micro and nanotechnology (CMi) at EPFL. The beam deflection system allows a maximum deflection of $\pm 100\ \mu$m in both the x and y directions. This implies that structures larger than the 200 μm × 200 μm field size will be divided in smaller pieces that will be patterned on their respective location on the sample through a movement of the xy-stage. This can lead to stitching errors.

In this work, we use ZEP 520A (based on styrene methyl acrylate) as an etch mask resist and PMMA for lift-off. Both are positive resists.

B.1.3 Inductively-Coupled Plasma Reactive Ion Etching

RIE uses a chemically reactive plasma in a low-pressure environment to remove material from the sample. High-energy ions from the plasma attack the exposed sample surface and form volatile products, which are subsequently evacuated. In an ICP RIE machine, the plasma is generated by an RF powered magnetic field, which results in a high-density plasma. This dry etching technique (referring to the absence of any liquid phase in the process) produces an anisotropic downward etch, opposed to the very isotropic etching in a wet etch process.

In this work, we use an SPTS Advanced Plasma System at CMi EPFL. This ICP RIE system is optimized for etching dielectrics. We use CHF_3/SF_6 etch chemistry, which produces a gentle etch of SiO_2 at 165 nm/min with a 2:1 selectivity to ZEP, while generating minimal damage to the latter. Other etch chemistries can burn the ZEP, which makes it impossible to remove afterwards.

B.1.4 Metal Evaporation and Lift-off

Al grating couplers were also fabricated in the framework of this thesis. Since it is not straightforward to etch Al layers with a good quality result, a lift-off procedure is used. The main aspect

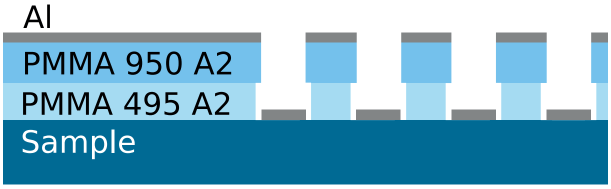

Figure B.3 – Sketch of a patterned PMMA resist doublelayer after exposure, development and Al evaporation. 495 and 950 refer to the molecular mass, while A2 refers to the concentration of PMMA in anisole.

to obtaining good quality lift-off is to avoid a continuous connection of the deposited material between the regions which should remain, and the ones that will be lifted-off. Indeed, if a continuous film is formed over the regions with and without resist, then (i) the solvent that is used to dissolve the resist might not be able to reach the resist layer, and (ii) the patches that are supposed to stay on the sample might be lifted-off with the other parts. For this reason, the resist and deposition technique are chosen to avoid this type of contact.

For the resist, we use a PMMA doublelayer with different molecular masses, i.e. different chain lengths. First, we spin-coat a layer of PMMA 495 (with a molecular mass of ~495 000 proton masses), and subsequently a second layer of PMMA 950 (molecular mass of ~950 000 proton masses). Since the shorter chains are more easily removed by the developer after the molecular chain scission events during the exposure, PMMA 495 has a lower threshold dose for removal. Consequently, every feature will be slightly oversized in the PMMA 495 layer, compared to the PMMA 950 layer and there will be an undercut in the resist layer. This is illustrated in Fig. B.3. As a result, material that is deposited anisotropically from normal incidence will be disjoint from the resist layer, and therefore also disjoint from the material deposited on the remaining resist. This will be true if the deposited layer is around a factor of two thinner than the bottom resist layer (empirical rule of thumb).

For this reason, the deposition technique should be highly directional, with a very small angular distribution around the sample normal. Therefore, we use a Leybold Optics LAB 600 H e-beam evaporator at CMi, EPFL to deposit the Al layer. In this tool, the sample is placed upside down in a vacuum chamber above a crucible filled with solid Al. The Al is locally heated by an electron beam, which causes Al atoms to evaporate. The large working distance of 1 m between the crucible and the sample results in a small angular spread of $\pm 0.5^\circ$, which is ideal for lift-off. A second advantage of the long working distance is that the sample can be maintained close to room temperature, which avoids damaging the resist. There are also two downsides to a large working distance. First, since the evaporated species are diluted over a large area, the deposition rate is low, on the order of ~100 nm/h. Second, a large chamber takes a long time to pump down to low pressure, which is required to ensure a mean free path that is substantially larger than the working distance. The LAB 600 H has a powerful two-stage cryogenic pump that allows to reach 10^{-6} mbar (corresponding to ~100 m mean free path, which is sufficient for the process) after around 1 h of pumping.

B.2 Optical Characterization

B.2.1 Photoluminescence

PL is one of the most commonly used techniques to investigate the optical properties of bulk semiconductors and semiconductor nanostructures. In PL, carriers are generated by a laser with a photon energy that is superior to the bandgap of the sample under investigation. Subsequently, the emitted light from the sample is collected and sent to a spectrometer for analysis. The main advantage of this technique is that in addition to extended states, localized or bound states can also be probed, contrary to the case of absorption-based techniques, such as photoluminescence excitation or photoreflectance, explained below, where these states are difficult to probe due to their small oscillator strength.

PL experiments were conducted with the sample mounted in a closed-cycle helium cryostat. The cryostat has a heating element with a proportional–integral–derivative (PID) controller that allows to maintain the sample at any temperature between 11 and 350 K with a precission of ± 0.1 K. Photocarriers were generated using a CW HeCd laser at 325 nm with the laser beam focused down to a 50 μm diameter spot size on the sample. The resulting emission was imaged onto the entrance slit of a 32 cm focal length Horiba iHR 320 monochromator equipped with a Peltier-cooled back-illuminated UV-enhanced CCD.

In μ-PL measurements, the same principle is applied, but the excitation and collection happen through a microscope objective in back-scattering geometry. This results in a small laser spot size below ~5 μm. For the μ-PL mapping experiments (a hyperspectral image where an emission spectrum is recorded for every pixel), the excitation laser beam was spatially filtered to approach a Gaussian beam profile, which results in a reduced spot size below 1 μm.

The μ-PL experiments were performed with the sample mounted in a cold-finger continuous-flow liquid-helium cryostat. This cryostat allows to control the sample temperature between 4 and 350 K with a precision of ± 0.2 K through a heating element with PID controller. A CW frequency-doubled Ar^+ laser emitting at 244 nm was used for the excitation in most of the experiments. Alternatively, we used the fourth harmonic of a Q-switched Nd:YAG laser operating at 266 nm, emitting 440 ps long pulses with a repetition rate of 9 kHz. The laser beam was coupled into an 80× UV microscope objective. The emitted light was collected through the same objective lens and sent to the spectrometer entrance slit by two lenses. The spectrometer consists of a liquid-nitrogen cooled back-illuminated UV-enhanced CCD mounted on a 55 cm focal length monochromator.

Time-Resolved Photoluminescence

In TRPL, the PL emission intensity is monitored as a function of time. This gives information about the carrier dynamics in the structure under investigation. To achieve this, a pulsed laser is used for excitation and a streak camera is mounted on the monochromator. Incoming photons from the sample are first horizontally dispersed according to their wavelength by the monochromator grating and then hit a photo-cathode which subsequently emits electrons due to the photo-electric effect. These electrons are accelerated and pass in between two capacitor plates, which apply an oscillating vertical electric field, synchronized to the laser repetition frequency, in the so-called synchroscan mode. Consequently, the electrons are vertically deflected depending on their time-delay with respect to the laser pulse. Finally, the electrons hit a fluorescence screen, which is imaged on a CCD. With this configuration, we can read the photon wavelength on the horizontal axis of the CCD, and the time delay on the vertical axis in a single measurement.

TRPL experiments were performed by Dr. Gwénolé Jacopin at EPFL with the sample mounted in a closed-cycle helium cryostat at $T = 15$ K. The third harmonic of a Ti:Al_2O_3 mode-locked laser (with pulse width of 2 ps and repetition rate of 80.7 MHz) was used, with the excitation wavelength set to 285 nm. The PL decay was recorded with a Hamamatsu streak camera working in synchroscan mode mounted on a 32 cm focal length Horiba iHR 320 monochromator. The temporal resolution of this setup is ~5 ps.

B.2.2 Cathodoluminescence

The electron beam in a SEM can also be used to generate carriers in a semiconductor sample. When a primary electron passes by the sample with ~kV-level kinetic energy, the Fourier transform of the transient electric field that is seen by the sample contains frequency components up to several tens of eV. This means that electronic transitions up to these energies can be realized using such an electron beam, which acts as a broadband excitation source. In CL, the resulting light emission is collected by a mirror and sent to a spectrometer for analysis. This technique is ideal for the study of wide bandgap semiconductors for which excitation lasers above the bandgap energy are hardly available. Additionally, the small size of the excitation spot on the order of ~10 nm allows to probe the spatial variation of the optical properties with high resolution. By raster scanning the electron beam, high-resolution hyperspectral images can be created.

The CL spectroscopy experiments shown in this work were performed by Dr. Gwénolé Jacopin in an Attolight Chronos CL microscope operating at $T = 11$ K with an acceleration voltage of 2 kV. The CL emission was recorded in hyperspectral mode (64 pixels × 64 pixels) with a dwell time of 10 ms using a Horiba iHR 320 monochromator coupled to a Peltier-cooled CCD.

B.2.3 Photoluminescence excitation

PLE spectroscopy is an absorption technique that allows to probe the intrinsic states of semiconductor (nano)structures. A tunable monochromatic light source[1] is focused on the sample and the intensity of the emitted light is measured for each excitation wavelength. The emitted intensity will peak if the absorption reaches a maximum, i.e. if the laser is resonant with an electronic transition in the sample.

---

[1] This can be a tunable laser or a broadband lamp filtered by a monochromator.

The PLE measurements presented here were performed by Dr. Gordon Callsen at TU Berlin with the sample mounted in a cold-finger helium-flow cryostat. We used a tunable dye laser as excitation source with 2-methyl-5-t-butyl-p-quaterphenyl as active medium, dissolved in 1,4-dioxane. The dye laser was pumped by a XeCl excimer laser emitting at 308 nm with a repetition rate of 100 Hz, enabling a pulse duration of 12 ns for the dye laser. The excitation laser has a linewidth of 40 μeV and a side-mode suppression ratio of two orders of magnitude. The excitation light was impinging on the sample at an incidence angle of 45 degrees with respect to the sample normal and focused using a UV achromatic lens doublet with a focal length of 20 cm leading to an excitation spot size diameter of ~100 μm. The sample luminescence was collected along the normal to the sample and imaged onto a Spex 1404 double monochromator with 85 cm focal length. This geometry efficiently suppresses reflection of the laser light into the detection line while the double monochromator unit further reduces the laser stray light. This monochromator was equipped with two 1200 l/mm gratings (500 nm blaze wavelength) employed in second order to achieve an optical resolution better than 50 μeV in the wavelength region of interest. Finally, the dispersed light was monitored with a UV-enhanced CCD. For each excitation wavelength, we recorded a PL spectrum hence leading to so-called polychromatic PLE scans.

B.2.4 Photoreflectance

PR is a type of modulation spectroscopy and a powerful optical technique to study and characterize the properties of semiconductors. The concept behind modulation spectroscopy techniques is to measure and interpret changes in the sample's optical response caused by modifying the measurement conditions. This results in sharp derivative-like features at the critical points in the sample's band structure. In photoreflectance, the change in reflectance ΔR is measured under optical injection of carriers in the sample by a laser source.

The PR setup that was used in this work was developed by Christian Mounir in the framework of his Master's thesis at EPFL-LASPE [195] and is shown in Fig. B.4. The sample was placed in a closed-cycle helium cryostat. Carriers were generated by a frequency-quadrupled Nd:YAG laser emitting at 266 nm, mechanically chopped at 170 Hz. The laser spot was defocused to a diameter of ~1 mm, to ensure a low carrier injection regime and to avoid screening of the built-in electric field in the QWs. The incident probe light on the sample (spot size ~500 μm) was coming from a xenon lamp coupled to a monochromator. The reflected light intensity was measured by a UV-enhanced Si photodiode and the modulation – caused by the photogenerated carriers – was controlled by a lock-in amplifier.

B.2.5 Variable Stripe Length Method

The VSL method is a technique that allows to measure the net modal gain in a waveguide structure and was first developed in the early 1970's at Bell labs [196].

The VSL setup used here was first constructed by Marco Malinverni in the framework of his PhD

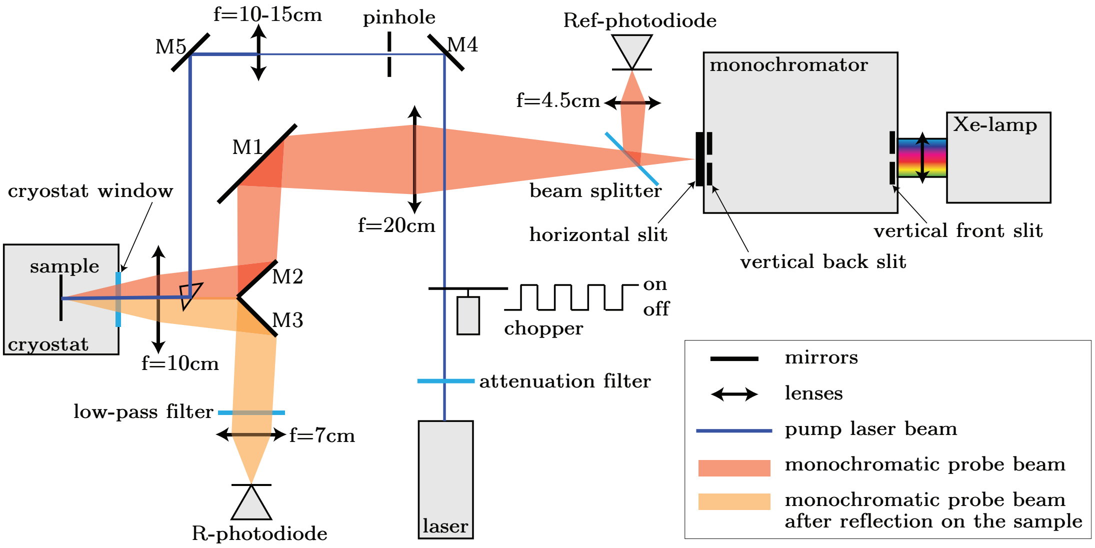

Figure B.4 – Schematic representation of the photoreflectance setup. Reproduced from [195].

thesis at EPFL-LASPE [157] and is shown in Fig. B.5. The measurements were performed on the waveguide sample at 300 K. The sample was pumped from the sample surface with a 25 μm wide and a 400 μm (L) or 800 μm ($2L$) long rectangular laser spot. We use the third (fourth) harmonic of a Q-switched Nd:YAG laser operating at 355 (266) nm, emitting 520 ps (440 ps) long pulses with a repetition rate of 8.7 kHz (9 kHz), which was magnified using a 10× beam expander and then refocused with a cylindrical lens. The beam was clipped at the correct position to achieve a pump stripe of the desired length. We aligned the sample with the maximum of the beam profile to ensure a homogeneous excitation stripe. The light generated in the waveguide was collected from a cleaved facet with an optical fiber using either two lenses to focus the emission in the fiber (as shown in Fig. B.5) or end-fire coupling without any optics (not shown), and subsequently sent to a Horiba iHR 320 spectrometer with a Peltier-cooled CCD. The net modal gain g_{mod} was determined by comparing the intensities of the measured signal for the two stripe lengths I_{2L} and I_L [196]:

$$g_{mod}(\lambda) = \Gamma g(\lambda) - \alpha(\lambda) = \frac{1}{L}\ln\left(\frac{I_{2L}(\lambda)}{I_L(\lambda)} - 1\right), \tag{B.3}$$

where Γ, $g(\lambda)$, and $\alpha(\lambda)$ are the optical confinement factor, the material gain, and the waveguide absorption losses, respectively.

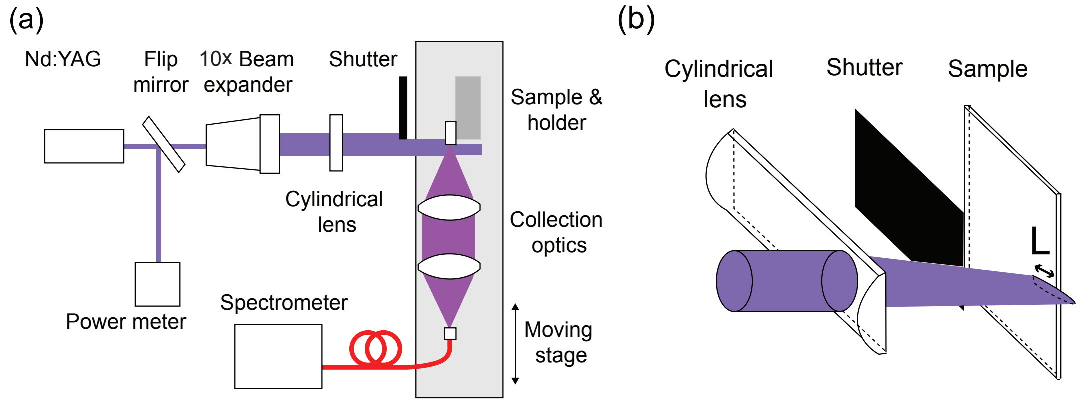

Figure B.5 – (a) Schematic representation of the variable stripe length setup. The sample and collection optics are mounted on the same stage in order to align the sample with respect to the laser stripe maximum, without affecting the collection alignment. (b) Detail of the pumping scheme and stripe length control. Reproduced from [157].

Bibliography

[1] S. Nakamura, *Nobel Lecture: Background story of the invention of efficient blue InGaN light emitting diodes*, Rev. Mod. Phys. **87**, 1139 (2015).

[2] H. Amano, M. Kito, K. Hiramatsu, and I. Akasaki, *P-Type Conduction in Mg-Doped GaN Treated with Low-Energy Electron Beam Irradiation (LEEBI)*, Jpn. J. Appl. Phys. **28**, L2112 (1989).

[3] S. Nakamura, T. Mukai, M. Senoh, and N. Iwasa, *Thermal Annealing Effects on P-Type Mg-Doped GaN Films*, Jpn. J. Appl. Phys. **31**, L139 (1992).

[4] S. Nakamura, T. Mukai, and M. Senoh, *Candela-class high-brightness InGaN/AlGaN double-heterostructure blue-light-emitting diodes*, Appl. Phys. Lett. **64**, 1687 (1994).

[5] S. Nakamura, M. Senoh, S.-i. Nagahama, N. Iwasa, T. Yamada, T. Matsushita, H. Kiyoku, and Y. Sugimoto, *InGaN-Based Multi-Quantum-Well-Structure Laser Diodes*, Jpn. J. Appl. Phys. **35**, L74 (1996).

[6] Blu-ray Disc Association, *Physical Format Specifications for BD-ROM* (2010).

[7] N. Singla and J. A. O'Sullivan, *Influence of Pit-Shape Variation on the Decoding Performance for Two-Dimensional Optical Storage (TwoDOS)*, IEEE International Conference on Communications, Istanbul, Turkey (2006).

[8] D. A. B. Miller, *Device Requirements for Optical Interconnects to Silicon Chips*, Proc. IEEE **97**, 1166 (2009).

[9] P. Dong, W. Qian, S. Liao, H. Liang, C.-C. Kung, N.-N. Feng, R. Shafiiha, J. Fong, D. Feng, A. V. Krishnamoorthy, and M. Asghari, *Low loss shallow-ridge silicon waveguides*, Opt. Express **18**, 14474 (2010).

[10] ATLAS Collaboration, *Evidence for light-by-light scattering in heavy-ion collisions with the ATLAS detector at the LHC*, Nature Phys. **13**, 852 (2017).

[11] R. Boyd, *Nonlinear Optics* (Academic Press, Cambridge, 2008).

[12] G. A. Wurtz and A. V. Zayats, *Nonlinear surface plasmon polaritonic crystals*, Laser & Photon. Rev. **2**, 125 (2008).

[13] S. Pekar, *Theory of electromagnetic waves in a crystal with excitons*, J. Phys. Chem. Solids **5**, 11–22 (1958).

[14] T. C. H. Liew, A. V. Kavokin, and I. A. Shelykh, *Optical Circuits Based on Polariton Neurons in Semiconductor Microcavities*, Phys. Rev. Lett. **101**, 016402 (2008).

[15] A. Amo, T. C. H. Liew, C. Adrados, R. Houdré, E. Giacobino, A. V. Kavokin, and A. Bramati, *Exciton-polariton spin switches*, Nat. Photon. **4**, 361 (2010).

[16] P. M. Walker, L. Tinkler, D. V. Skryabin, A. Yulin, B. Royall, I. Farrer, D. A. Ritchie, M. S. Skolnick, and D. N. Krizhanovskii, *Ultra-low-power hybrid light-matter solitons*, Nat. Commun. **6**, 8317 (2015).

[17] S. Christopoulos, G. B. H. von Högersthal, A. J. D. Grundy, P. G. Lagoudakis, A. V. Kavokin, J. J. Baumberg, G. Christmann, R. Butté, E. Feltin, J.-F. Carlin, and N. Grandjean, *Room-Temperature Polariton Lasing in Semiconductor Microcavities*, Phys. Rev. Lett. **98**, 126405 (2007).

[18] G. Christmann, R. Butté, E. Feltin, J.-F. Carlin, and N. Grandjean, *Room temperature polariton lasing in a GaN/AlGaN multiple quantum well microcavity*, Appl. Phys. Lett. **93**, 051102 (2008).

[19] M. Kneissl and J. Rass, *III-Nitride Ultraviolet Emitters: Technology and Applications* (Springer International, Cham, 2016).

[20] M. Kneissl, T. Kolbe, C. Chua, V. Kueller, N. Lobo, J. Stellmach, A. Knauer, H. Rodriguez, S. Einfeldt, Z. Yang, N. M. Johnson, and M. Weyers, *Advances in group III-nitride-based deep UV light-emitting diode technology*, Semicond. Sci. Technol. **26**, 014036 (2011).

[21] An update with the latest results can be found at http://www.ifkp.tu-berlin.de/?id=agkneissl.

[22] R. G. Banal, M. Funato, and Y. Kawakami, *Optical anisotropy in [0001]-oriented* $Al_xGa_{1-x}N/AlN$ *quantum wells* ($x > 0.69$), Phys. Rev. B **79**, 121308 (2009).

[23] T. Wunderer, C. L. Chua, J. E. Northrup, Z. Yang, N. M. Johnson, M. Kneissl, G. A. Garrett, H. Shen, M. Wraback, B. Moody, H. S. Craft, R. Schlesser, R. F. Dalmau, and Z. Sitar, *Optically pumped UV lasers grown on bulk AlN substrates*, Phys. Status Solidi C **9**, 822 (2012).

[24] Y. Taniyasu, M. Kasu, and T. Makimoto, *An aluminium nitride light-emitting diode with a wavelength of 210 nanometres*, Nature **441**, 325 (2006).

[25] H. Yoshida, Y. Yamashita, M. Kuwabara, and H. Kan, *Demonstration of an ultraviolet 336 nm AlGaN multiple-quantum-well laser diode*, Appl. Phys. Lett. **93**, 241106 (2008).

[26] T. Oto, R. G. Banal, K. Kataoka, M. Funato, and Y. Kawakami, *100 mW deep-ultraviolet emission from aluminium-nitride-based quantum wells pumped by an electron beam*, Nat. Photon. **4**, 767 (2010).

[27] M. A. Kneissl, T. Kolbe, J. Schlegel, J. Stellmach, C. L. Chua, Z. Yang, A. Knauer, V. Kueller, M. Weyers, and N. Johnson, *AlGaN-based Ultraviolet Lasers - Applications and Materials Challenges*, CLEO 2011 p. JTuB1 (2011).

[28] R. Butté, E. Feltin, J. Dorsaz, G. Christmann, J.-F. Carlin, N. Grandjean, and M. Ilegems, *Recent Progress in the Growth of Highly Reflective Nitride-Based Distributed Bragg Reflectors and Their Use in Microcavities*, Jpn. J. Appl. Phys. **44**, 7207 (2005).

[29] J.-F. Carlin, C. Zellweger, J. Dorsaz, S. Nicolay, G. Christmann, E. Feltin, R. Butté, and N. Grandjean, *Progresses in III-nitride distributed Bragg reflectors and microcavities using AlInN/GaN materials*, Phys. Status Solidi B **242**, 2326 (2005).

[30] R. Butté, J.-F. Carlin, E. Feltin, M. Gonschorek, S. Nicolay, G. Christmann, D. Simeonov, A. Castiglia, J. Dorsaz, H. J. Buehlmann, S. Christopoulos, G. Baldassarri Höger von Högersthal, A. J. D. Grundy, M. Mosca, C. Pinquier, M. A. Py, F. Demangeot, J. Frandon, P. G. Lagoudakis, J. J. Baumberg, and N. Grandjean, *Current status of AlInN layers lattice-matched to GaN for photonics and electronics*, J. Phys. D: Appl. Phys. **40**, 6328 (2007).

[31] G. Cosendey, J.-F. Carlin, N. A. K. Kaufmann, R. Butté, and N. Grandjean, *Strain compensation in AlInN/GaN multilayers on GaN substrates: Application to the realization of defect-free Bragg reflectors*, Appl. Phys. Lett. **98**, 181111 (2011).

[32] G. Perillat-Merceroz, G. Cosendey, J.-F. Carlin, R. Butté, and N. Grandjean, *Intrinsic degradation mechanism of nearly lattice-matched InAlN layers grown on GaN substrates*, J. Appl. Phys. **113**, 063506 (2013).

[33] Y. Taniyasu, J.-F. Carlin, A. Castiglia, R. Butté, and N. Grandjean, *Mg doping for p-type AlInN lattice-matched to GaN*, Appl. Phys. Lett. **101**, 082113 (2012).

[34] A. Castiglia, J.-F. Carlin, E. Feltin, G. Cosendey, J. Dorsaz, and N. Grandjean, *Emission characteristics of GaN-based blue lasers including a lattice matched* $Al_{0.83}In_{0.17}N$ *optical blocking layer for improved optical beam quality*, Appl. Phys. Lett. **97**, 111104 (2010).

[35] Y. Taniyasu, J.-F. Carlin, A. Castiglia, R. Butté, and N. Grandjean, *Lattice-matched AlInN/GaN Heterostructures: n- and p-type doping and UV-LEDs*, Photonics West, San Francisco (2013).

[36] K. Ikeyama, Y. Kozuka, K. Matsui, S. Yoshida, T. Akagi, Y. Akatsuka, N. Koide, T. Takeuchi, S. Kamiyama, M. Iwaya, and I. Akasaki, *Room-temperature continuous-wave operation of GaN-based vertical-cavity surface-emitting lasers with n-type conducting AlInN/GaN distributed Bragg reflectors*, Appl. Phys. Express **10**, 102101 (2016).

[37] A. Muoz and K. Kunc, *High-pressure phase of gallium nitride*, Phys. Rev. B **44**, 10372(R) (1991).

[38] H. Xia, Q. Xia, and A. L. Ruoff, *High-pressure structure of gallium nitride: Wurtzite-to-rocksalt phase transition*, Phys. Rev. B **47**, 12925 (1993).

[39] T. Lei, M. Fanciulli, R. J. Molnar, T. D. Moustakas, R. J. Graham, and J. Scanlon, *Epitaxial growth of zinc blende and wurtzitic gallium nitride thin films on (001) silicon*, Appl. Phys. Lett. **59**, 944 (1991).

[40] O. Ambacher, J. Majewski, C. Miskys, A. Link, M. Hermann, M. Eickhoff, M. Stutzmann, F. Bernardini, V. Fiorentini, V. Tilak, B. Schaff, and L. F. Eastman, *Pyroelectric properties of Al(In)GaN/GaN hetero- and quantum well structures*, J. Phys.: Condens. Matter **14**, 3399 (2002).

[41] K. Lorenz, N. Franco, E. Alves, I. M. Watson, R. W. Martin, and K. P. O'Donnell, *Anomalous Ion Channeling in AlInN/GaN Bilayers: Determination of the Strain State*, Phys. Rev. Lett. **97**, 085501 (2006).

[42] V. Darakchieva, M. Beckers, M.-Y. Xie, L. Hultman, B. Monemar, J.-F. Carlin, E. Feltin, M. Gonschorek, and N. Grandjean, *Effects of strain and composition on the lattice parameters and applicability of Vegard's rule in Al-rich $Al_{1-x}In_xN$ films grown on sapphire*, J. Appl. Phys. **103**, 103513 (2008).

[43] N. A. Fichtenbaum, T. E. Mates, S. Keller, S. P. DenBaars, and U. K. Mishra, *Impurity incorporation in heteroepitaxial N-face and Ga-face GaN films grown by metalorganic chemical vapor deposition*, J. Cryst. Growth **310**, 1124 (2008).

[44] S. F. Chichibu, A. Setoguchi, A. Uedono, K. Yoshimura, and M. Sumiya, *Impact of growth polar direction on the optical properties of GaN grown by metalorganic vapor phase epitaxy*, Appl. Phys. Lett. **78**, 28 (2001).

[45] O. Ambacher, *Growth and applications of Group III-nitrides*, J. Phys. D: Appl. Phys. **31**, 2653 (1998).

[46] P. Sohi, D. Martin, and N. Grandjean, *Critical thickness of GaN on AlN: impact of growth temperature and dislocation density*, Semicond. Sci. Technol. **32**, 075010 (2017).

[47] E. Feltin, J.-F. Carlin, J. Dorsaz, G. Christmann, R. Butté, M. Laügt, M. Ilegems, and N. Grandjean, *Crack-free highly reflective AlInN-AlGaN Bragg mirrors for UV applications*, Appl. Phys. Lett. **88**, 051108 (2006).

[48] W. Paszkowicz, R. Cerny, and S. Krukowski, *Rietveld refinement for indium nitride in the 105-295 K range,* Powder Diffr. **18**, 114 (2003).

[49] W. Paszkowicz, S. Podsiado, and R. Minikayev, *Rietveld-refinement study of aluminium and gallium nitrides,* J. Alloys Compounds **382**, 100 (2004).

[50] L. Pauling, *The nature of the chemical bond and the structure of molecules and crystals* (Cornell University Press, New York, 1960).

[51] C. Wood and D. Jena, *Polarization Effects in Semiconductors: From Ab Initio Theory to Device Applications* (Springer (New York), 2008).

[52] S. Nicolay, J.-F. Carlin, E. Feltin, R. Butté, M. Mosca, N. Grandjean, M. Ilegems, M. Tchernycheva, L. Nevou, and F. H. Julien, *Midinfrared intersubband absorption in lattice-matched AlInN/GaN multiple quantum wells*, Appl. Phys. Lett. **87**, 111106 (2005).

[53] L. Liu and J. Edgar, *Substrates for gallium nitride epitaxy*, Mat. Sci. Eng. R **37**, 61 (2002).

[54] F. Semond, Y. Cordier, N. Grandjean, F. Natali, B. Damilano, S. Vézian, and J. Massies, *Molecular Beam Epitaxy of Group-III Nitrides on Silicon Substrates: Growth, Properties and Device Applications*, Phys. Status Solidi A **188**, 501 (2001).

[55] N. Vico Triviño, R. Butté, J.-F. Carlin, and N. Grandjean, *Continuous Wave Blue Lasing in III-Nitride Nanobeam Cavity on Silicon*, Nano Lett. **15**, 1259 (2015).

[56] L. Zhang, W. Tan, S. Westwater, A. Pujol, A. Pinos, S. Mezouari, S. K, J. Whiteman, J. Shannon, and K. Stricklan, *High Brightness GaN-on-Si Based Blue LEDs Grown on 150 mm Si Substrates Using Thin Buffer Layer Technology*, J. Electron Devices Soc. **3**, 457 (2015).

[57] Sumitomo Electric, http://global-sei.com.

[58] E. Feltin, A. Castiglia, G. Cosendey, L. Sulmoni, J.-F. Carlin, N. Grandjean, M. Rossetti, J. Dorsaz, V. Laino, M. Duelk, and C. Velez, *Broadband blue superluminescent light-emitting diodes based on GaN*, Appl. Phys. Lett. **95**, 081107 (2009).

[59] J.-F. Carlin and M. Ilegems, *High-quality AlInN for high index contrast Bragg mirrors lattice matched to GaN*, Appl. Phys. Lett. **83**, 668 (2003).

[60] L. Zhou, D. J. Smith, M. R. McCartney, D. S. Katzer, and D. F. Storm, *Observation of vertical honeycomb structure in InAlN/GaN heterostructures due to lateral phase separation*, Appl. Phys. Lett. **90**, 081917 (2007).

[61] J. Mánuel, F. Morales, J. Lozano, D. González, R. García, T. Lim, L. Kirste, R. Aidam, and O. Ambacher, *Structural and compositional homogeneity of InAlN epitaxial layers nearly lattice-matched to GaN*, Acta Mater. **58**, 4120 (2010).

[62] M. H. Wong, F. Wu, C. A. Hurni, S. Choi, J. S. Speck, and U. K. Mishra, *Molecular beam epitaxy of InAlN lattice-matched to GaN with homogeneous composition using ammonia as nitrogen source*, Appl. Phys. Lett. **100**, 072107 (2012).

[63] N. A. K. Kaufmann, L. Lahourcade, B. Hourahine, D. Martin, and N. Grandjean, *Critical impact of Ehrlich-Schwöbel barrier on GaN surface morphology during homoepitaxial growth*, J. Cryst. Growth **433**, 36 (2016).

[64] T. C. Sadler, M. J. Kappers, and R. A. Oliver, *The impact of hydrogen on indium incorporation and surface accumulation in InAlN epitaxy*, J. Cryst. Growth **331**, 4 (2011).

[65] M. Gonschorek, Ph.D. thesis, EPFL, Thesis nr. 4586, Lausanne (2011).

[66] L. Lugani, Ph.D. thesis, EPFL, Thesis nr. 6628, Lausanne (2015).

[67] G. Liaugaudas, G. Jacopin, J.-F. Carlin, R. Butté, and N. Grandjean, *Optical properties of nearly lattice-matched GaN/(Al,In)N quantum wells*, J. Appl. Phys. **119**, 205708 (2016).

[68] J. Dorsaz, J.-F. Carlin, S. Gradecak, and M. Ilegems, *Progress in AlInN-GaN Bragg reflectors: Application to a microcavity light emitting diode*, J. Appl. Phys. **97**, 084505 (2005).

[69] R. Butté, G. Cosendey, L. Lugani, M. Glauser, A. Castiglia, G. Perillat-Merceroz, J.-F. Carlin, and N. Grandjean, *III-Nitride Semiconductors and their Modern Devices, edited by B. Gil* (Oxford University Press, Oxford, 2013), chap. Properties of InAlN layers nearly lattice-matched to GaN and their use for photonics and electronics.

[70] J. Kim, Z. Lochner, M.-H. Ji, S. Choi, H. J. Kim, J. S. Kim, R. D. Dupuis, A. M. Fischer, R. Juday, Y. Huang, T. Li, J. Y. Huang, F. A. Ponce, and J.-H. Ryou, *Origins of unintentional incorporation of gallium in InAlN layers during epitaxial growth, part II: Effects of underlying layers and growth chamber conditions*, J. Cryst. Growth **388**, 143 (2014).

[71] M. Gonschorek, J.-F. Carlin, E. Feltin, M. A. Py, N. Grandjean, V. Darakchieva, B. Monemar, M. Lorenz, and G. Ramm, *Two-dimensional electron gas density in* $Al_{1-x}In_xN$*/AlN/GaN heterostructures (0.03* $\leq x \leq$ *0.23)*, J. Appl. Phys. **103**, 093714 (2008).

[72] T. Matsuoka, *Calculation of unstable mixing region in wurtzite* $In_{1-x-y}Ga_xAl_yN$, Appl. Phys. Lett. **71**, 105 (1997).

[73] T. C. Sadler, M. J. Kappers, and R. A. Oliver, *The effect of temperature and ammonia flux on the surface morphology and composition of* $In_xAl_{1-x}N$ *epitaxial layers*, J. Cryst. Growth **311**, 3380 (2009).

[74] E. Feltin, D. Simeonov, J.-F. Carlin, R. Butté, and N. Grandjean, *Narrow UV emission from homogeneous GaN/AlGaN quantum wells*, Appl. Phys. Lett. **90**, 021905 (2007).

[75] E. Rosencher and B. Vinter, *Optoelectronics* (Cambridge University Press, Cambridge, 2002).

[76] P. Y. Yu and M. Cardona, *Fundamentals of Semiconductors: Physics and Material Properties, Fourth Edition* (Springer, Berlin, 2010).

[77] C. F. Klingshirn, *Semiconductor Optics, Fourth edition* (Springer, Berlin Heidelberg, 2012).

[78] I. Vurgaftman and J. R. Meyer, *Band parameters for nitrogen-containing semiconductors*, J. Appl. Phys. **94**, 3675 (2003).

[79] S. A. Kazazis, E. Papadomanolaki, M. Androulidaki, M. Kayambaki, and E. Iliopoulos, *Optical properties of InGaN thin films in the entire composition range*, J. Appl. Phys. **123**, 125101 (2018).

[80] Y. P. Varshni, *Temperature dependence of the energy gap in semiconductors*, Physica **34**, 149 (1967).

[81] L. Viña, S. Logothetidis, and M. Cardona, *Temperature dependence of the dielectric function of germanium*, Phys. Rev. B **30**, 1979 (1984).

[82] D. Brunner, H. Angerer, E. Bustarret, F. Freudenberg, R. Höpler, R. Dimitrov, O. Ambacher, and M. Stutzmann, *Optical constants of epitaxial AlGaN films and their temperature dependence*, J. Appl. Phys. **82**, 5090 (1997).

[83] B. Gil and O. Briot, *Internal structure and oscillator strengths of excitons in strained α-GaN*, Phys. Rev. B **55**, 2530 (1997).

[84] L. C. de Carvalho, A. Schleife, and F. Bechstedt, *Influence of exchange and correlation on structural and electronic properties of AlN, GaN, and InN polytypes*, Phys. Rev. B **84**, 195105 (2011).

[85] S. L. Chuang and C. S. Chang, *k.p method for strained wurtzite semiconductors*, Phys. Rev. B **54**, 2491 (1996).

[86] A. Shikanai, T. Azuhata, T. Sota, S. Chichibu, A. Kuramata, K. Horino, and S. Nakamura, *Biaxial strain dependence of exciton resonance energies in wurtzite GaN*, J. Appl. Phys. **81**, 417 (1997).

[87] G. H. Wannier, *The Structure of Electronic Excitation Levels in Insulating Crystals*, Phys. Rev. **52**, 191 (1937).

[88] J. Frenkel, *On the Transformation of Light into Heat in Solids. I*, Phys. Rev. **37**, 17 (1931).

[89] J. Frenkel, *On the Transformation of Light into Heat in Solids. II*, Phys. Rev. **37**, 1276 (1931).

[90] P. Rinke, M. Winkelnkemper, A. Qteish, D. Bimberg, J. Neugebauer, and M. Scheffler, *Consistent set of band parameters for the group-III nitrides AlN, GaN, and InN*, Phys. Rev. B **77**, 075202 (2008).

[91] K. Kornitzer, T. Ebner, K. Thonke, R. Sauer, C. Kirchner, V. Schwegler, M. Kamp, M. Leszczynski, I. Grzegory, and S. Porowski, *Photoluminescence and reflectance spectroscopy of excitonic transitions in high-quality homoepitaxial GaN films*, Phys. Rev. B **60**, 1471 (1999).

[92] G. Rossbach, M. Feneberg, M. Röppischer, C. Werner, N. Esser, C. Cobet, T. Meisch, K. Thonke, A. Dadgar, and J. Bläsing, *Influence of exciton-phonon coupling and strain on the anisotropic optical response of wurtzite AlN around the band edge*, Phys. Rev. B **83**, 195202 (2011).

[93] B. Gil, *Physics of Wurtzite Nitrides and Oxides* (Springer International, Cham, 2014).

[94] C. F. Klingshirn, J. Geurts, A. Hoffmann, B. K. Meyer, and A. Waag, *ZnO: From Fundamentals Towards Novel Applications* (Springer, Berlin Heidelberg, 2010).

[95] I. Vurgaftman, J. R. Meyer, and L. R. Ram-Mohan, *Band parameters for III-V compound semiconductors and their alloys*, J. Appl. Phys. **89**, 5815 (2001).

[96] J. J. Hopfield, *Theory of the Contribution of Excitons to the Complex Dielectric Constant of Crystals*, Phys. Rev. **112**, 1555 (1958).

[97] G. Rossbach, Ph.D. thesis, EPFL, Thesis nr. 6245 (2014).

[98] G. Martin, A. Botchkarev, A. Rockett, and H. Morkoç, *Valence-band discontinuities of wurtzite GaN, AlN, and InN heterojunctions measured by x-ray photoemission spectroscopy*, Appl. Phys. Lett. **68**, 2541 (1996).

[99] G. Bastard, *Wave mechanics applied to semiconductor heterostructures* (Les Éditions de Physique, Les Ulis, 1988).

[100] R. L. Greene, K. K. Bajaj, and D. E. Phelps, *Energy levels of Wannier excitons in GaAs-GaAlAs quantum-well structures*, Phys. Rev. B **29**, 1807 (1984).

[101] R. P. Leavitt and J. W. Little, *Simple method for calculating exciton binding energies in quantum-confined semiconductor structures*, Phys. Rev. B **42**, 11774 (1990).

[102] L. C. Andreani and A. Pasquarello, *Accurate theory of excitons in GaAs-GaAlAs quantum wells*, Phys. Rev. B **42**, 8928 (1990).

[103] G. Christmann, R. Butté, E. Feltin, A. Mouti, P. A. Stadelmann, A. Castiglia, J.-F. Carlin, and N. Grandjean, *Large vacuum Rabi splitting in a multiple quantum well GaN-based microcavity in the strong-coupling regime*, Phys. Rev. B **77**, 085310 (2008).

[104] N. Grandjean, B. Damilano, S. Dalmasso, M. Leroux, M. Laügt, and J. Massies, *Built-in electric-field effects in wurtzite AlGaN/GaN quantum wells*, J. Appl. Phys. **86**, 3714 (1999).

[105] F. Bernardini and V. Fiorentini, *Spontaneous versus Piezoelectric Polarization in III-V Nitrides: Conceptual Aspects and Practical Consequences*, Phys. Status Solidi B **216**, 391 (1999).

[106] N. Grandjean and R. Butté, *Polarization Effects in Semiconductors: From Ab Initio Theory to Device Applications, edited by C. Wood and D. Jena* (Springer, New York, 2008), chap. Effects of Polarization in Optoelectronic Quantum Structures.

[107] E. M. Purcell, *Spontaneous Emission Probabilities at Radio Frequencies*, Phys. Rev. **69**, 674 (1946).

[108] C. Weisbuch and B. Vinter, *Quantum Semiconductor Structures: Fundamentals and Applications* (Academic Press, inc., San Diego, 1991).

[109] G. C. Dente and M. L. Tilton, *Calculating radiative matrix elements for semiconductors*, J. Opt. Soc. Am. B **15**, 1737 (1998).

[110] M. Glauser, C. Mounir, G. Rossbach, E. Feltin, J.-F. Carlin, R. Butté, and N. Grandjean, *InGaN/GaN quantum wells for polariton laser diodes: Role of inhomogeneous broadening*, J. Appl. Phys. **115**, 233511 (2014).

[111] R. Houdré, R. P. Stanley, U. Oesterle, M. Ilegems, and C. Weisbuch, *Room temperature exciton-photon Rabi splitting in a semiconductor microcavity*, Le Journal de Physique IV **03**, 51 (1993).

[112] W. Liu, J.-F. Carlin, N. Grandjean, B. Deveaud, and G. Jacopin, *Exciton dynamics at a single dislocation in GaN probed by picosecond time-resolved cathodoluminescence*, Appl. Phys. Lett. **109**, 042101 (2016).

[113] S. Rudin and T. Reinecke, *Temperature-dependent exciton linewidths in semiconductor quantum wells*, Phys. Rev. B **41**, 3017 (1990).

[114] S. Rudin, T. Reinecke, and B. Segall, *Temperature-dependent exciton linewidths in semiconductors*, Phys. Rev. B **42**, 11218 (1990).

[115] T. Aschenbrenner, H. Dartsch, C. Kruse, M. Anastasescu, M. Stoica, M. Gartner, A. Pretorius, A. Rosenauer, T. Wagner, and D. Hommel, *Optical and structural characterization of AlInN layers for optoelectronic applications*, J. Appl. Phys. **108**, 063533 (2010).

[116] E. Sakalauskas, H. Behmenburg, C. Hums, P. Schley, G. Rossbach, C. Giesen, M. Heuken, H. Kalisch, R. H. Jansen, J. Bläsing, A. Dadgar, A. Krost, and R. Goldhahn, *Dielectric function and optical properties of Al-rich AlInN alloys pseudomorphically grown on GaN*, J. Phys. D: Appl. Phys. **43**, 365102 (2010).

[117] B. E. A. Saleh and M. C. Teich, *Fundamentals of Photonics, second edition* (Wiley, Hoboken, 2007).

[118] O. Ambacher, W. Rieger, P. Ansmann, H. Angerer, T. Moustakas, and M. Stutzmann, *Sub-bandgap absorption of gallium nitride determined by Photothermal Deflection Spectroscopy*, Solid State Commun. **97**, 365 (1996).

[119] J. Levrat, Ph.D. thesis, EPFL, Thesis nr. 5449 (2012).

[120] S. Schmitt-Rink, C. Ell, S. W. Koch, H. E. Schmidt, and H. Haug, *Subband-level renormalization and absorptive optical bistability in semiconductor multiple quantum well structures*, Solid State Commun. **52**, 123 (1984).

[121] E. Hanamura and H. Haug, *Condensation effects of excitons*, Phys. Rep. **33**, 209 (1977).

[122] M. Kira, F. Jahnke, S. W. Koch, J. D. Berger, D. V. Wick, T. R. Nelson, G. Khitrova, and H. M. Gibbs, *Quantum Theory of Nonlinear Semiconductor Microcavity Luminescence Explaining Boser Experiments*, Phys. Rev. Lett. **79**, 5170 (1997).

[123] N. F. Mott, *The transition to the metallic state*, Philos. Mag. **6**, 287 (1961).

[124] G. Rossbach, J. Levrat, G. Jacopin, M. Shahmohammadi, J.-F. Carlin, J.-D. Ganière, R. Butté, B. Deveaud, and N. Grandjean, *High-temperature Mott-transition in wide band-gap semiconductor quantum wells*, Phys. Rev. B **90**, 201308(R) (2014).

[125] M. G. A. Bernard and G. Duraffourg, *Laser Conditions in Semiconductors*, Phys. Status Solidi B **1**, 699 (1961).

[126] S. Schmitt-Rink, D. S. Chemla, and D. A. B. Miller, *Theory of transient excitonic optical nonlinearities in semiconductor quantum-well structures*, Phys. Rev. B **32**, 6601 (1985).

[127] R. Syms and J. Cozens, *Optical guided waves and devices* (McGraw-Hill, Berkshire, 1992).

[128] M. Fox, *Quantum Optics, An Introduction* (Oxford University Press, New York, 2006).

[129] V. Savona, L. C. Andreani, P. Schwendimann, and A. Quattropani, *Quantum well excitons in semiconductor microcavities: Unified treatment of weak and strong coupling regimes*, Solid State Commun. **93**, 733 (1995).

[130] J. Kasprzak, M. Richard, S. Kundermann, A. Baas, P. Jeambrun, J. M. J. Keeling, F. M. Marchetti, M. H. Szymańska, R. André, J. L. Staehli, V. Savona, P. B. Littlewood, B. Deveaud, and L. S. Dang, *Bose-Einstein condensation of exciton polaritons.*, Nature **443**, 409 (2006).

[131] Y. Zhu, D. J. Gauthier, S. E. Morin, Q. Wu, H. J. Carmichael, and T. W. Mossberg, *Vacuum Rabi splitting as a feature of linear-dispersion theory: Analysis and experimental observations*, Phys. Rev. Lett. **64**, 2499 (1990).

[132] J. S. C. Prentice, *Coherent, partially coherent and incoherent light absorption in thin-film multilayer structures*, J. Phys. D: Appl. Phys. **33**, 3139 (2000).

[133] M. Glauser, Ph.D. thesis, EPFL, Thesis nr. 6415, Lausanne (2014).

[134] R. Houdré, R. P. Stanley, and M. Ilegems, *Vacuum-field Rabi splitting in the presence of inhomogeneous broadening: Resolution of a homogeneous linewidth in an inhomogeneously broadened system*, Phys. Rev. A **53**, 2711 (1996).

[135] Y. Kaluzny, P. Goy, M. Gross, J. M. Raimond, and S. Haroche, *Observation of Self-Induced Rabi Oscillations in Two-Level Atoms Excited Inside a Resonant Cavity: The Ringing Regime of Superradiance*, Phys. Rev. Lett. **51**, 1175 (1983).

[136] C. Weisbuch, M. Nishioka, A. Ishikawa, and Y. Arakawa, *Observation of the coupled exciton-photon mode splitting in a semiconductor quantum microcavity*, Phys. Rev. Lett. **69**, 3314 (1992).

[137] M. H. Anderson, J. R. Ensher, M. R. Matthews, C. E. Wieman, and E. A. Cornell, *Observation of Bose-Einstein condensation in a dilute atomic vapor*, Science **269**, 198 (1995).

[138] A. Imamoglu, R. Ram, S. Pau, and Y. Yamamoto, *Nonequilibrium condensates and lasers without inversion: Exciton-polariton lasers*, Phys. Rev. A **53**, 4250 (1996).

[139] A. Amo, J. Lefrère, S. Pigeon, C. Adrados, C. Ciuti, I. Carusotto, R. Houdré, E. Giacobino, and A. Bramati, *Superfluidity of polaritons in semiconductor microcavities*, Nat. Phys. **5**, 805 (2009).

[140] K. G. Lagoudakis, M. Wouters, M. Richard, A. Baas, I. Carusotto, R. André, L. S. Dang, and B. Deveaud-Plédran, *Quantized vortices in an exciton-polariton condensate*, Nat. Phys. **4**, 706 (2008).

[141] M. Saba, C. Ciuti, J. Bloch, V. Thierry-Mieg, R. André, L. S. Dang, S. Kundermann, A. Mura, G. Bongiovanni, J. L. Staehli, and B. Deveaud, *High-temperature ultrafast polariton parametric amplification in semiconductor microcavities*, Nature **414**, 731 (2001).

[142] D. Ballarini, M. De Giorgi, E. Cancellieri, R. Houdré, E. Giacobino, R. Cingolani, A. Bramati, G. Gigli, and D. Sanvitto, *All-optical polariton transistor*, Nat. Commun. **4**, 1778 (2013).

[143] C. Sturm, D. Tanese, H. Nguyen, H. Flayac, E. Galopin, A. Lemaître, I. Sagnes, D. Solnyshkov, A. Amo, G. Malpuech, and J. Bloch, *All-optical phase modulation in a cavity-polariton Mach-Zehnder interferometer*, Nat. Commun. **5**, 3278 (2014).

[144] P. M. Walker, L. Tinkler, M. Durska, D. M. Whittaker, I. J. Luxmoore, B. Royall, D. N. Krizhanovskii, M. S. Skolnick, I. Farrer, and D. A. Ritchie, *Exciton polaritons in semiconductor waveguides*, Appl. Phys. Lett. **102**, 012109 (2013).

[145] I. Rosenberg, Y. Mazuz-Harpaz, R. Rapaport, K. West, and L. Pfeiffer, *Electrically controlled mutual interactions of flying waveguide dipolaritons*, Phys. Rev. B **93**, 195151 (2016).

[146] T. Ellenbogen and K. B. Crozier, *Exciton-polariton emission from organic semiconductor optical waveguides*, Phys. Rev. B **84**, 161304(R) (2011).

[147] H. Takeda and K. Sakoda, *Exciton-polariton mediated light propagation in anisotropic waveguides*, Phys. Rev. B **86**, 205319 (2012).

[148] S. Pirotta, M. Patrini, M. Liscidini, M. Galli, G. Dacarro, G. Canazza, G. Guizzetti, D. Comoretto, and D. Bajoni, *Strong coupling between excitons in organic semiconductors and Bloch surface waves*, Appl. Phys. Lett. **104**, 051111 (2014).

[149] D. D. Solnyshkov, H. Terças, and G. Malpuech, *Optical amplifier based on guided polaritons in GaN and ZnO*, Appl. Phys. Lett. **105**, 231102 (2014).

[150] J. Ciers, J. G. Roch, J.-F. Carlin, G. Jacopin, R. Butté, and N. Grandjean, *Propagating Polaritons in III-Nitride Slab Waveguides*, Phys. Rev. Applied **7**, 034019 (2017).

[151] J. Liu, *Photonic Devices* (Cambridge University Press, Cambridge, 2005).

[152] J. Ding, H. Jeon, T. Ishihara, M. Hagerott, A. V. Nurmikko, H. Luo, N. Samarth, and J. Furdyna, *Excitonic gain and laser emission in ZnSe-based quantum wells*, Phys. Rev. Lett. **69**, 1707 (1992).

[153] U. T. Schwarz, H. Braun, K. Kojima, M. Funato, Y. Kawakami, S. Nagahama, and T. Mukai, *Investigation and comparison of optical gain spectra of (Al,In)GaN laser diodes emitting in the 375 nm to 470 nm spectral range*, Proc. of SPIE **6485**, 648506 (2007).

[154] Lumerical Solutions, Inc., FDTD Solutions v. 8.11.422.

[155] S. Birner, T. Zibold, T. Andlauer, T. Kubis, M. Sabathil, A. Trellakis, and P. Vogl, *Nextnano: General Purpose 3-D Simulations*, IEEE Trans. Electron. Devices **54**, 2137 (2007).

[156] D. Segev and C. G. Van de Walle, *Origins of Fermi-level pinning on GaN and InN polar and nonpolar surfaces*, Europhys. Lett. **76**, 305 (2006).

[157] M. Malinverni, Ph.D. thesis, EPFL, Thesis nr. 6747, Lausanne (2015).

[158] D. E. Aspnes, *Third-derivative modulation spectroscopy with low-field electroreflectance*, Surf. Sci. **37**, 418 (1973).

[159] J. P. Estrera, W. M. Duncan, and R. Glosser, *Complex Airy analysis of photoreflectance spectra for III-V semiconductors*, Phys. Rev. B **49**, 7281 (1994).

[160] M. Leroux, B. Beaumont, N. Grandjean, P. Lorenzini, S. Haffouz, P. Vennéguès, J. Massies, and P. Gibart, *Luminescence and reflectivity studies of undoped, n- and p-doped GaN on (0001) sapphire*, Mater. Sci. Eng. B **50**, 97 (1997).

[161] G. Callsen, M. R. Wagner, T. Kure, J. S. Reparaz, M. Bügler, J. Brunnmeier, C. Nenstiel, A. Hoffmann, M. Hoffmann, J. Tweedie, Z. Bryan, S. Aygun, R. Kirste, R. Collazo, and Z. Sitar, *Optical signature of Mg-doped GaN: Transfer processes*, Phys. Rev. B **86**, 075207 (2012).

[162] G. Rossbach, J. Levrat, E. Feltin, J.-F. Carlin, R. Butté, and N. Grandjean, *Impact of saturation on the polariton renormalization in III-nitride based planar microcavities*, Phys. Rev. B **88**, 165312 (2013).

[163] M. Shahmohammadi, W. Liu, G. Rossbach, L. Lahourcade, A. Dussaigne, C. Bougerol, R. Butté, N. Grandjean, B. Deveaud, and G. Jacopin, *Enhancement of Auger recombination induced by carrier localization in InGaN/GaN quantum wells*, Phys. Rev. B **95**, 125314 (2017).

[164] J. R. Haynes, *Experimental Proof of the Existence of a New Electronic Complex in Silicon*, Phys. Rev. Lett. **4**, 361 (1960).

[165] D. A. Kleinman, *Binding energy of biexcitons and bound excitons in quantum wells*, Phys. Rev. B **28**, 871 (1983).

[166] J. C. Kim, D. R. Wake, and J. P. Wolfe, *Thermodynamics of biexcitons in a GaAs quantum well*, Phys. Rev. B **50**, 15099 (1994).

[167] D. Taillaert, F. Van Laere, M. Ayre, W. Bogaerts, D. Van Thourhout, P. Bienstman, and R. Baets, *Grating Couplers for Coupling between Optical Fibers and Nanophotonic Waveguides*, Jpn. J. Appl. Phys. **45**, 6071 (2006).

[168] M. Glauser, Master's thesis, EPFL (2010).

[169] D. M. Whittaker, P. Kinsler, T. A. Fisher, M. S. Skolnick, A. Armitage, A. M. Afshar, M. D. Sturge, and J. S. Roberts, *Motional Narrowing in Semiconductor Microcavities*, Phys. Rev. Lett. **77**, 4792 (1996).

[170] V. Y. Davydov, Y. E. Kitaev, I. N. Goncharuk, A. N. Smirnov, J. Graul, O. Semchinova, D. Uffmann, M. B. Smirnov, A. P. Mirgorodsky, and R. A. Evarestov, *Phonon dispersion and Raman scattering in hexagonal GaN and AlN*, Phys. Rev. B **58**, 12899 (1998).

[171] T. Guillet, M. Mexis, J. Levrat, G. Rossbach, C. Brimont, T. Bretagnon, B. Gil, R. Butté, N. Grandjean, and L. Orosz, *Polariton lasing in a hybrid bulk ZnO microcavity*, Appl. Phys. Lett. **99**, 161104 (2011).

[172] F. Tassone, C. Piermarocchi, V. Savona, A. Quattropani, and P. Schwendimann, *Bottleneck effects in the relaxation and photoluminescence of microcavity polaritons*, Phys. Rev. B **56**, 7554 (1997).

[173] L. Tinkler, Ph.D. thesis, University of Sheffield, Department of Physics and Astronomy (2015).

[174] M. Maragkou, A. J. D. Grundy, T. Ostatnicky, and P. G. Lagoudakis, *Longitudinal optical phonon assisted polariton laser*, Appl. Phys. Lett. **97**, 111110 (2010).

[175] P. Corfdir, J. Levrat, G. Rossbach, R. Butté, E. Feltin, J.-F. Carlin, G. Christmann, P. Lefebvre, J.-D. Ganière, N. Grandjean, and B. Deveaud-Plédran, *Impact of biexcitons on the relaxation mechanisms of polaritons in III-nitride based multiple quantum well microcavities*, Phys. Rev. B **85**, 245308 (2012).

[176] F. Li, L. Orosz, O. Kamoun, S. Bouchoule, C. Brimont, P. Disseix, T. Guillet, X. Lafosse, M. Leroux, J. Leymarie, M. Mexis, M. Mihailovic, G. Patriarche, F. Réveret, D. Solnyshkov, J. Zuniga-Perez, and G. Malpuech, *From Excitonic to Photonic Polariton Condensate in a ZnO-Based Microcavity*, Phys. Rev. Lett. **110**, 196406 (2013).

[177] G. Christmann, R. Butté, E. Feltin, J.-F. Carlin, and N. Grandjean, *Impact of inhomogeneous excitonic broadening on the strong exciton-photon coupling in quantum well nitride microcavities*, Phys. Rev. B **73**, 153305 (2006).

[178] J. Levrat, R. Butté, E. Feltin, J.-F. Carlin, N. Grandjean, D. Solnyshkov, and G. Malpuech, *Condensation phase diagram of cavity polaritons in GaN-based microcavities: Experiment and theory*, Phys. Rev. B **81**, 125305 (2010).

[179] R. Hahe, C. Brimont, P. Valvin, T. Guillet, F. Li, M. Leroux, J. Zuniga-Perez, X. Lafosse, G. Patriarche, and S. Bouchoule, *Interplay between tightly focused excitation and ballistic propagation of polariton condensates in a ZnO microcavity*, Phys. Rev. B **92**, 235308 (2015).

[180] D. A. B. Miller, D. S. Chemla, D. J. Eilenberger, P. W. Smith, A. C. Gossard, and W. T. Tsang, *Large room-temperature optical nonlinearity in GaAs/GaAlAs multiple quantum well structures*, Appl. Phys. Lett. **41**, 679 (1982).

[181] T. Lermer, A. Gomez-Iglesias, M. Sabathil, J. Müller, S. Lutgen, U. Strauss, B. Pasenow, J. Hader, J. V. Moloney, S. W. Koch, W. Scheibenzuber, and U. T. Schwarz, *Gain of blue and cyan InGaN laser diodes*, Appl. Phys. Lett. **98**, 021115 (2011).

[182] M. Martens, C. Kuhn, T. Simoneit, S. Hagedorn, A. Knauer, T. Wernicke, M. Weyers, and M. Kneissl, *The effects of magnesium doping on the modal loss in AlGaN-based deep UV lasers*, Appl. Phys. Lett. **110**, 081103 (2017).

[183] K. Kojima, U. T. Schwarz, M. Funato, Y. Kawakami, S. Nagahama, and T. Mukai, *Optical gain spectra for near UV to aquamarine (Al,In)GaN laser diodes*, Optics Express **15**, 7730 (2007).

[184] D. A. B. Miller, *Are optical transistors the logical next step?*, Nature Photon. **4**, 3 (2010).

[185] G. Schmidt, M. Müller, P. Veit, F. Bertram, J. Christen, M. Glauser, J.-F. Carlin, G. Cosendey, R. Butté, and N. Grandjean, *Nano-scale luminescence characterization of individual InGaN/GaN quantum wells stacked in a microcavity using scanning transmission electron microscope cathodoluminescence*, Appl. Phys. Lett. **105**, 032101 (2014).

[186] J. D. Jackson, *Classical Electrodynamics, third Edition.* (Wiley, New York, 1998).

[187] K. Yee, *Numerical solution of initial boundary value problems involving Maxwell's equations in isotropic media*, IEEE Trans. Antennas. Propag. **14**, 302 (1966).

[188] D. M. Sullivan, *Electromagnetic Simulation Using the FDTD Method, second edition* (Wiley, Hoboken, 2013).

[189] A. Taflove, A. Oskooi, and S. G. Johnson, *Advances in FDTD Computational Electrodynamics: Photonics and Nanotechnology* (Artech House, Norwood, 2013).

[190] Lumerical Knowledgebase, available at https://www.lumerical.com/support/knowledge_base/.

[191] Oxford Instruments, www.oxford-instruments.com/.

[192] S. Rizvi, *Handbook of Photomask Manufacturing Technology* (CRC Press, Boca Raton, 2005).

[193] M. Hatzakis, *Electron resists for microcircuit and mask production*, J. Electrochem. Soc. **116**, 1033 (1969).

[194] D. R. Herriott, R. Collier, D. Alles, and J. Stafford, *EBES: A practical electron lithographic system*, IEEE Trans. Electron Devices **22**, 385 (1975).

[195] C. Mounir, Master's thesis, EPFL (2012).

[196] K. L. Shaklee, R. E. Nahory, and R. F. Leheny, *Optical gain in semiconductors*, J. Lumin. **7**, 284 (1973).

Joachim Ciers

Curriculum Vitae

Address	Chemin Aimé Steinlen 10 1004 Lausanne, Switzerland
E-mail	joachim.ciers@epfl.ch
Phone	+41 78 802 07 25
Date of birth	24/12/1991
Nationality	Belgian

Work Experience

Research Assistant **École Polytechnique Fédérale de Lausanne**
Supervised by Prof. Nicolas Grandjean and Dr. Raphaël Butté 2014-present
Experimental research on light-matter interaction in semiconductor nanostructures
Supervision of master projects, teaching of general physics courses to bachelor students
Teaching award from the physics section (CHF 1000 cash prize)

Internship **Chemnitz University of Technology**
Supervised by Dr. Christian Müller Jul – Aug 2013
Development of carbon-nanotube-based strain sensors

Internship **University of Oslo**
Supervised by Prof. Morten Hjorth-Jensen Aug – Sep 2012
Numerical solution methods of the time-dependent Schrödinger equation

Education

Ph.D. in Physics **École Polytechnique Fédérale de Lausanne**
Focus on semiconductor physics, advanced optics, nanofabrication 2014-2018

Master of Science in Engineering Physics – Cum Laude **Ghent University**
including one Erasmus semester at the Universidad Complutense de Madrid 2012-2014
Focus on optics, semiconductor physics and devices, nanotechnology, plasma physics, numerical methods, particle physics, photovoltaics and sustainable energy, physical chemistry, heat transport
Master thesis: Subwavelength Nanopatch Cavities with Colloidal Nanocrystals
Supervised by Prof. Zeger Hens and Prof. Dries Van Thourhout

Bachelor of Science in Engineering Physics **Ghent University**
Focus on mathematics, physics, chemistry, programming, quantum mechanics, electronics, electromagnetism, solid-state physics, photonics 2009-2012

High School education – Cum Laude **Sint-Jozefscollege, Izegem (Belgium)**
Focus on sciences and mathematics – Award for extraordinary merit 2005-2009

Skills

Computer

- Scientific calculations, programming and data processing (Matlab, Python, C++, JAVA, optical simulations, Origin),
- LaTeX, Office
- Inkscape, Illustrator
- Linux

Scientific

- Strong background in science, engineering and technology
- Advanced competences in optics and semiconductor physics
- Optical spectroscopy techniques (various methods, optical setup design)
- Nanofabrication (e-beam lithography, etching, deposition, SEM, AFM)
- Laser installation and maintenance
- Vacuum and cryogenic techniques

Communication

- High-level scientific and educational communication, oral and written
- Presentation
- Supervision of master students
- Teaching to undergraduates

Languages

Dutch	native	**French**	full proficiency (C2)	**Spanish**	good (B2)
English	full proficiency (C2)	**German**	fluent (C1)		

Scientific Publications and Presentations

- **J. Ciers**, G. Jacopin, G. Callsen, C. Bougerol, J.-F. Carlin, R. Butté and N. Grandjean, *"Near-UV Narrow Bandwidth Optical Gain in Lattice-Matched III-Nitride Waveguides"*, Jpn. J. Appl. Phys **57**, 090305 (2018).
- **J. Ciers**, J. G. Roch, J.-F. Carlin, G. Jacopin, R. Butté, N. Grandjean, *"Propagating Polaritons in III-Nitride Slab Waveguides"*, Phys. Rev. Applied **7**, 034019 (2017)
- T. Braniste, **J. Ciers**, E. Monaico, D. Martin, J.-F. Carlin, V. V. Ursaki, V. V. Sergentu, I. M. Tiginyanu and N. Grandjean, *"Multilayer porous structures of HVPE and MOCVD grown GaN for photonic applications"*, Superlattices and Microstructures **102**, 221 (2017)
- **J. Ciers**, J. G. Roch, J.-F. Carlin, G. Jacopin, R. Butté, N. Grandjean, *"Propagating Polaritons in III-Nitride Slab Waveguides"*, contributed talk at OECS, Bath, UK (2017)
- G. Callsen, K. Shojiki, C. Haller, W. Liu, G. Jacopin, I. M. Rousseau, M. Castelli, S. P. T. Kaufmann, **J. Ciers**, P. Sohi, J.-F. Carlin, D. Martin, R. Butté, and N. Grandjean, *"Isoelectronic doping of GaN by indium: impurity band formation"*, contributed talk at ICNS 12, Strasbourg, France (2017)
- K. Shojiki, S. P. T. Kaufmann, J.-F. Carlin, G. Callsen, I. Rousseau, **J. Ciers**, G. Jacopin, R. Butté, and N. Grandjean, *"Position-controlled GaN nanostructures embedded in AlN film on Si substrate"*, poster presentation at ICNS 12, Strasbourg, France (2017)
- **J. Ciers**, J.-F. Carlin, R. Butté, N. Grandjean, *"Strong Light-Matter Coupling in planar III-N waveguides"*, poster presentation at Frontiers in Nanophotonics, Ascona, Switzerland (2015)

Extracurricular Activities and Interests

- Senior member of ShARE EPFL (global student think tank association) – Projects on energy storage for renewable intermittent electricity production, reduction of the CO_2 footprint of business air travel, and correlation between researchers' air travel CO_2 footprint and their academic excellence
- Board member at IAESTE (global association providing international internships for students) – Local Committee President Lausanne (2017) – Finance Coordinator Local Committee Lausanne (2015-2016) – Board Member Local Committee Ghent (2012-2014)
- Treasurer (2011-2014) and External Public Relations (2010-2011) in student association Apollo (Ghent)
- 6th position in the Flemish Chemistry Olympiad, finalist in the Flemish Biology Olympiad and Physics Olympiad in 2008-2009
- 13th position (on 33 participating teams) with the Flemish team at the European Union Science Olympiad in Nicosia, Cyprus in 2008 - Winner of the Flemish preselection for the European Union Science Olympiad in 2007-2008
- 10th position in the Flemish Physics Olympiad, finalist in the Flemish Chemistry Olympiad in 2007-2008
- Traveling, learning, educating, triathlon, duathlon, cycling, hiking, skiing